Study of Lambda quasi-free production in the 3H(e,e'K+)X reaction

Doctoral Thesis

Study of Lambda quasi-free production in the $^3\mathrm{H}(e, e'K^+)X$ reaction

$^3\mathrm{H}(e, e'K^+)X$ 反応における ラムダ粒子準自由生成の研究

Kosuke Itabashi

Department of Physics, Graduate School of Science
Tohoku University

2021 (令和 3 年)

Abstract

A nucleus is a system of baryons which are composed of three valence quarks, and bound by the strong interaction. We can understand the nuclear system and the origin of matter by studying the strong interaction between baryons. The nucleon-nucleon (NN) interaction has been studied with NN scattering data. However, the Λ-nucleon (ΛN) interaction has large uncertainty due to difficulties of ΛN scattering experiments. Therefore, the ΛN interaction has been mainly studied by spectroscopy of Λ hypernuclei. The recoil Λ which is produced in a nucleus is known to interact with a nucleon in the nucleus (FSI), and the ΛN interaction can be studied by treating it as the ΛN scattering problem. An $nn\Lambda$ is a neutral nucleus with a Λ, and the study of this structure provides the precious information of the Λn interaction. However, the existence of the $nn\Lambda$ is not established at all. In 2013, HypHI collaboration at GSI reported a possible bound state of the $nn\Lambda$ by measuring a final state of $\pi^- + t$. However, the peak significance of the invariant mass of $\pi^- + t$ was not enough to establish the bound state of $nn\Lambda$. Theoretical calculations that reproduce the Λ binding energies of light hypernuclei do not support the existence of the bound $nn\Lambda$ state. On the other hand, a resonance state of $nn\Lambda$ may exist if the Λn interaction is strengthened by about 5% which is not contradict the existing experimental data. Therefore, in order to search for the $nn\Lambda$ state, the experiment (E12-17-003) was performed in 2018 at JLab Hall A by using the $(e, e'K^+)$ reaction which enabled a high resolution spectroscopy of Λ hypernuclei.

In this experiment, a ^{3}H target with a thickness of 84.8 mg/cm^2 was irradiated with an electron beam at a beam current of 22.5 μA and with a beam energy of 4.3 GeV in order to measured the missing mass of $nn\Lambda$ in the $^3\mathrm{H}(e, e'K^+)X$ reaction. A K^+ with a central momentum of 1.8 GeV/c and a scattered electron with a central momentum of 2.2 GeV/c were measured by using two HRS spectrometers which were set at angles of $\theta_{eK} = 13.2^\circ$ and $\theta_{ee'} = 13.2^\circ$.

In the missing mass spectrum on the $^3\mathrm{H}(e, e'K^+)X$ reaction, any clear peak was not observed. However, there was on enhancement near the $nn\Lambda$ mass threshold ($-B_\Lambda \sim 0$ MeV), and the differential cross section of it was evaluated by using an assumed $nn\Lambda$ peak function with $(-B_\Lambda, \Gamma) = (0.55, 4.7)$ MeV. It was obtained as $21.7 \pm 6.7(\mathrm{stat.}) \pm 5.2(\mathrm{syst.})$ nb/sr by fitting the experimental data with this function, and the upper limit of the $nn\Lambda$ (CL90%) was estimated as 36.5 nb/sr.

Since the differential cross section of the Λ-QF distribution observed in this experiment in-

cluded the enhancement due to the Λn FSI, it was necessary to take the Λn FSI into account in the analysis. The differential cross section including FSI can be obtained as the product of the differential cross section without FSI and the influence factor ($I(k_{\rm rel})$) which depends on Λn relative momentum ($k_{\rm rel}$). With the effective range approximation, the influence factor can be written by using two Λn potential parameters, scattering length (a) and effective range (r). The JLab standard simulation code, SIMC with the influence factor, calculated the distribution of the differential cross section including the Λn FSI effect. As a result of fitting, the experimental data with the SIMC spectrum including the $nn\Lambda$ peak and the Λn FSI effect, the reduce chi-square in the range of $0 \leq -B_\Lambda \leq 60$ MeV took the minimum value of 0.98 when the scattering length (a) and the effective range (r) were at $(a, r) = (-2.6, 5.0)$ fm. The effective range at given a scattering length was constrained with this analysis. Assuming the scattering length is -2.6 fm, the effective range was obtained as $5.0^{+1.3}_{-1.2}$ fm.

Contents

List of Figures

List of Tables

Chapter 1 Introduction

"What is the fundamental principle to describe in the world ?" This is the ultimate question for many scientists. Today, the standard model, which is established from quantum chromodynamics (QCD) and electroweak theory, is most widely supported as a first principle theory. The standard model predicts elementary particles, six quarks, six leptons, gauge bosons and higgs boson, all of which are observed. A hadron which is a multi quark system is classified into a baryon composed of three quarks (qqq) and a meson composed of a quark and an anti quark ($q\bar{q}$). Each of quark in the hadron was bound by a strong interaction. The strong interaction between quarks and gluons is an effect by the medium of gluon with color charge and is described by the established QCD theory. In a high energy region ($Q \gg \Lambda_{QCD}$), in which a perturbation approach calculation can be used, strong interactions among quarks can be calculated by QCD with asymptotic freedom. However, the baryon-baryon (BB) interaction in the low energy region cannot be described by the perturbation calculation of QCD because of a large coupling constant. Therefore, the phenomenological approach is necessary to understand BB interaction. The scattering experiment is a major experimental method to derive BB interactions from, and succeeded in deriving well nucleon-nucleon (NN) interaction.

On the other hand, a hyperon including an s-quark decays with a short lifetime ($\tau \sim 10^{-10}$ sec), so the hyperon nucleon (YN) scattering data is limited, and especially there is no scattering data of Λn. A hypernucleus which is a bound hyperon in a nucleus was used to deduce the YN interaction. A $nn\Lambda$, a neutral system with a Λ, is a good tool to deduce the Λn interaction on which no scattering data exist. This article studied the Λn interaction with $^3\mathrm{H}(\mathrm{e},\mathrm{e}'\mathrm{K}^+)\mathrm{X}$ data measured at JLab. This section introduces the experimental method and the history for studying YN interactions, and the purpose of this study.

1.1 Hyperon

A baryon with an s quark with strangeness ($S = -1$) is classified as a hyperon. Since the bare masses of u, d and s quarks are less than energy scale $\Lambda_{\mathrm{QCD}} \sim 250$ MeV, these quarks are approximately treated in the flavor SU(3) symmetry frame ($SU(3)_{\mathrm{f}}$). The irreducible representation of baryons in $SU(3)_{\mathrm{f}}$ is decomposed as :

$$\mathbf{3} \otimes \mathbf{3} \otimes \mathbf{3} = \mathbf{10}_S \oplus \mathbf{8}_M \oplus \mathbf{8}_M \oplus \mathbf{1}_A, \tag{1.1}$$

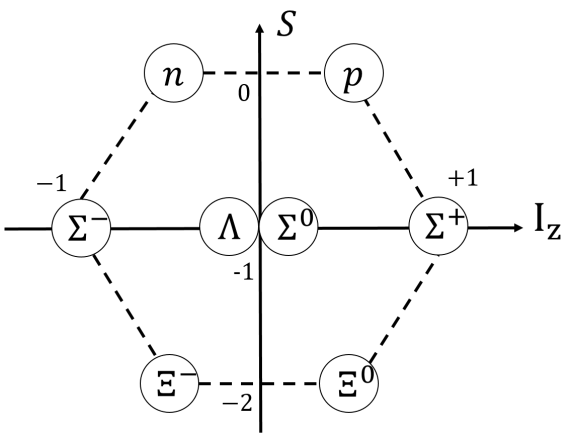

Figure 1.1: Baryon octet is group of baryons consisting of combinations of three u,d or s quarks with a half of spin and a positive parity. Iz and S are shows component of isospin and strangeness, respectively.

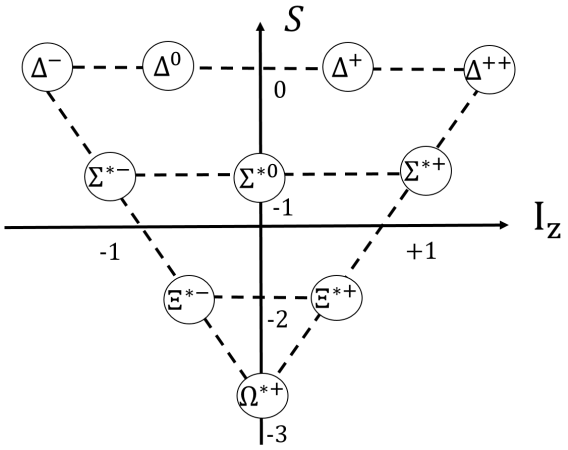

Figure 1.2: Baryon decuplet is group of barons combination consisting of combinations of three u, d or s quarks with one and a half of spins and a positive parity. I_z and S are shows component of isospin and strangeness, respectively.

where subscripts of S, A and M show parts of symmetry, asymmetry and mixed, respectively. A baryon requires asymmetry in a wave function by Pauli exclusion principle. Therefore, in the $\mathrm{SU(3)_f}$, the octet and decuplet terms in Eq. 1.1 satisfy the principle. Figure 1.1 and 1.2 show the baryon group classified as octet (spin parity, $J^P = 1/2^+$) and decuplet ($J^P = 3/2^+$) in $SU(3)_f$ frame. Both of Λ and Σ^0 in Fig. 1.1 are $S = -1$, $I_z = 0$, but they have different isospins, singlet $I = 0$ and triplet $I = 1$, respectively. The hyperons have heavier masses ($m > 1.1156$ GeV/c^2) than the nucleon mass (~ 0.94 GeV/c^2) and decay into a nucleon in a short lifetime ($\tau \sim 10^{-10}$ sec).

1.2 Historical study of YN interaction

The irreducible representation of octets baryon-baryon (BB) interaction ($\mathbf{8} \otimes \mathbf{8}$) is decomposed as follows,

$$\mathbf{8} \otimes \mathbf{8} = \mathbf{1} \oplus \mathbf{8}_S \oplus \mathbf{27} \oplus \mathbf{8}_A \oplus \mathbf{10} \oplus \mathbf{10}^*. \tag{1.2}$$

The first three terms in Eq. 1.2 are symmetric and the others are anti-symmetric under a flavor exchange of two baryons. Combinations of NN, ΛN, ΣN systems in the isospin basis are summarized in Table 1.1. The NN interactions belong to the ($\mathbf{10}*$) and ($\mathbf{27}$) multiplets. On the other hand, ΛN interactions are written in terms of ($\mathbf{10}*$), ($\mathbf{27}$), $\mathbf{8_s}$ and $\mathbf{8_a}$ multiplets. The $\mathbf{8_s}, \mathbf{8_a}$ terms are not included in NN interactions, so information of ΛN interaction gives us more expanded understanding the strong interaction.

Table 1.1: The irreducible representation of the baryon-baryon potentials in the $(\mathbf{8} \otimes \mathbf{8})$ basis for NN, ΛN and ΣN interactions

B-B	Isospin (I)	flavor symmetric	flavor anti-symmetric
NN	I = 0	-	$(\mathbf{10}^*)$
NN	I = 1	$(\mathbf{27})$	-
ΛN	I = 1/2	$\frac{1}{\sqrt{10}}((\mathbf{8}_s) + 3(\mathbf{27}))$	$\frac{1}{\sqrt{2}}(-(\mathbf{8}_a) + (\mathbf{10}^*))$
ΣN	I =1/2	$\frac{1}{\sqrt{10}}(3(\mathbf{8}_s) - (\mathbf{27}))$	$\frac{1}{\sqrt{2}}((\mathbf{8}_a) + (\mathbf{10}^*))$
ΣN	I =3/2	$(\mathbf{27})$	$(\mathbf{10})$

Table 1.2: The summary of existing data for $\Lambda p \to \Lambda p$ scattering.

Reference	Λ beam production	p_Λ [GeV/c]	$N_{\Lambda p \to \Lambda p}$ [Counts]
Crawford *et al.*, [1]	$\pi^0 p \to \Lambda K^0$	0.5 - 1.0	4
Alexander*et al.*, (1961) [2]	$\pi^0 p \to \Lambda K^0$	0.4 - 1.0	14
Groves [3]	$K^- N \to \Lambda \pi$	0.3 - 1.5	26
Beilliére *et al.*, [4]	$K^- N \to \Lambda \pi$	0.3 - 1.5	86
Piekenbrock *et al.*, [5]	$K^- A \to \Lambda X$	0.15 - 0.4	11
Sechi-Zorn *et al.*, [6]	$K^- p \to \Lambda X$	0.12 - 0.4	75
Vishnevksiĭ *et al.*, [7]	$nA \to \Lambda X$	0.9 - 4.7	12
Bassano *et al.*, [8]	$K^- p \to \Lambda X$	1.0 - 5.0	68
Alexander *et al.*, (1968) [9]	$K^- p \to \Lambda X$	0.1 - 0.3	378
Sechi-Zorn *et al.*, (1968) [10]	$K^- p \to \Lambda X$	0.1 - 0.3	224
Kadyk *et al.*, [11]	K^-Pt $\to \Lambda X$	0.3 - 1.5	175
Anderson *et al.*, [12]	pPt $\to \Lambda X$	1.0 - 17.0	109
Mount *et al.*, [13]	pCu $\to \Lambda X$	0.5 - 24.0	71

1.2.1 Elastic scattering

An elastic scattering reaction conserves the kinetic energy of particles in the center of mass frame, and these experiments were performed to derive the strength of NN interactions from a scattering cross section.

The mass of Λ, which is the lightest in hyperons, is easy to be produced. Thus, many Λp scattering experiments were performed in the world as a first step to deduce the YN interaction. Fig. 1.3 shows the scattering cross section distribution depending on indicating center of energy ($\sqrt{s}$). Blue points in Fig. 1.3 shows Λp elastic data which were summarized in Tab. 1.2. The scattering data about the Λp is limited (about 1300 counts) because the Λ decays to a nucleon in a short lifetime ($\tau_\Lambda \sim 260$ ps). Therefore, the Λp interaction has a huge uncertainty comparing with the NN interaction.

1.2.2 ΛN interaction in Λ hypernuclei

The two-body scattering experiment is a major method to derive the BB interactions, but the ΛN scattering data is limited. Hence, an attempt was made to derive the ΛN interactions from a investigation of the Λ hypernuclei, in which a Λ is bound in a nuclear system. On the

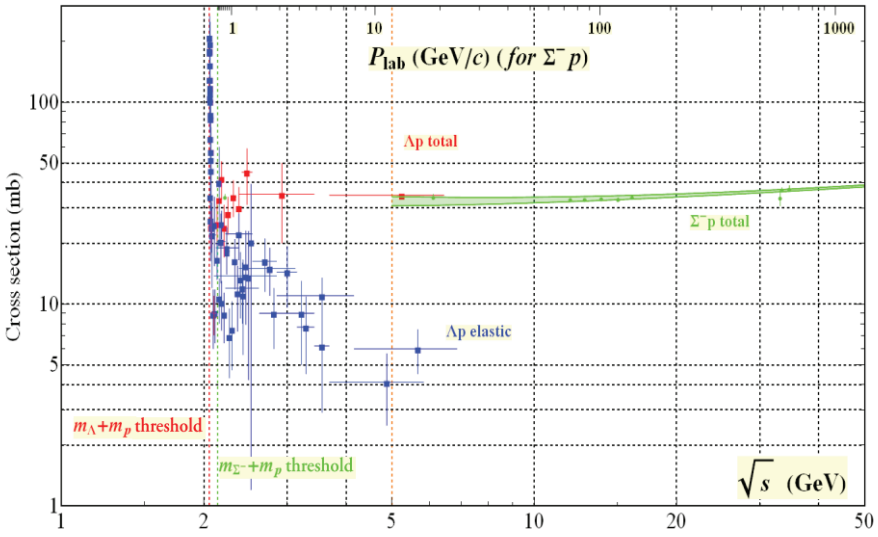

Figure 1.3: Cross sections of elastic scattering [14]. The horizontal and vertical axes indicate center of energy($\sqrt{s}$) and cross section (mb), respectively. The blue and red dot points shows Λp elastic data and total data which are including elastic and inelastic for $\Lambda p \to \Lambda p$. Each of points of elastic data for $\Lambda p \to \Lambda p$ has huge error because of limited data ($\sim$ 2000 events).

assumption that the wave function of the Λ and that of the core nucleus in Λ hypernuclei can be treated independent by the Hamiltonian of the Λ hypernuclus is described as

$$\mathbf{H}_{\mathrm{Hyp}} = \mathbf{H}_{\mathrm{core}} + t_{\mathrm{HYP}} + \sum v^{\mathrm{eff}}_{\Lambda N} \tag{1.3}$$

where $\mathbf{H}_{\mathrm{core}}$, t_{HYP} and $\sum v^{\mathrm{eff}}_{\Lambda N}$ are a Hamiltonian of the core nucleus, the kinematic energy of the hypernuclus and the effective ΛN potential, respectively. The effective ΛN potential takes account of an effect of the interaction between the core nucleus and the Λ, and can be deduced via the G-matrix method from ΛN interaction in the free space [15].

Table 1.3 shows results of the G-matrix calculations with each ΛN potential model in environment of nuclear density. The ΛN interaction in the environment of free space is given by one-boson exchange models such as Nijmen potential, extend soft core potential (ESC04 -08), soft core potential (NSC97 e and f) models. By comparing experimental data with a cross section or binding energy of Λ hypernuclei deduced from Eq. 1.3, the ΛN effective potential can be tested.

1.2.3 Λp final state interaction

A YN final state interaction (YN FSI) represents the interaction that occurs during YN scattering after the hyperon production. Especially, Λp FSI was derived from a Λp inelastic scattering or Λ quasi free spectrum about ${}^{3}_{\Lambda}\mathrm{H}$.

Table 1.3: Partial wave contributions to $U_\Lambda(\rho_0)$

model	$^1S_0$	$^3S_1$	$^1P_1$	$^3P_0$	$^3P_1$	$^3P_2$	D	sum
ESC08a	-12.7	-22.2	3.0	0.1	1.4	-3.6	-1.6	-35.6
ESC08b	-12.3	-19.7	2.7	-0.2	1.5	-4.2	-1.7	-34.0
ESC04a	-13.7	-20.5	0.6	0.2	0.5	-4.5	-1.0	-38.5
ESC04d	-13.6	-26.6	3.2	-0.2	0.9	-6.4	-1.4	-44.1
ESC06d	-13.3	-30.7	3.5	-0.2	1.7	-4.3	-1.2	-44.5
ESC06d*	-11.8	-26.9	3.8	0.0	2.1	-3.4	-1.1	-37.2
NSC97e	-12.7	-25.5	2.1	0.5	3.2	-1.2	-1.1	-34.7
NSC97f	-14.3	-22.4	2.4	0.5	4.0	-0.7	-1.2	-31.7

■ **Λp final state interaction with inelastic scattering**

Experiments for deducing the Λp final state interaction were performed with reactions of $K^- + d \rightarrow \pi^- + (\Lambda p)$ [16–18], $\pi^+ d \rightarrow K^+ + (\Lambda p)$ and $p + p \rightarrow K^+ + (\Lambda p)$ [19–27]. An inelastic scattering reaction dose not conserve the kinematic energy of the incident particle. The lost energy is converted into excitation energy of the target or used for pair production of $s\bar{s}$ quarks in a nucleon.

In the case of inelastic scattering by ($p_b + p_{tar} \rightarrow K^+ + \Lambda + p$) reaction, the Λp FSI can be derived from a (Λp) missing mass spectrum which is obtained with momenta of the K^+ and the injected beam. Especially, the effect of the Λp FSI expects to produce an enhance structure around the Λp mass threshold because this mass region corresponds to the small relative momentum region in the center of mass frame in Λp (Fig. 1.4). This structure can be treated as the two-body scattering problem.

By treating this enhance structure as a two-body scattering problem, it can be calculated as the scattering differential cross section. The double differential cross section can be deduced from the scattering amplitude and enhancement factor(I) as,

$$\frac{d^2\sigma}{d\Omega_K dM_{\Lambda p}} = \frac{\Phi_3}{4}\left(\mathrm{I_s}|M_s|^2 + 3\mathrm{I_t}|M_t|^2\right), \tag{1.4}$$

where Φ_3, $|M_s|$ and $|M_t|$ are phase space, and transition matrix elements in spin singlet and triplet. On the effective range approximation, the enhancement factor was written by Jost function with a scattering length (a) and effective range (r) parameters in a Λp potential. These parameters can be determined by fitting experimental data (Fig. 1.4) with Eq. 1.4.

■ **FSI study with Λ quasi free production**

A nucleon in a nucleus has a momentum. In the Fermi gas model, the Fermi momentum (k_F) in the nucleus is calculated as $k_F = (3\pi^2\rho_N)^{1/3}$ with the nuclear density (ρ_N) which is obtained by a quasi-elastic scattering experiment. The Λ particles produced in the reaction with

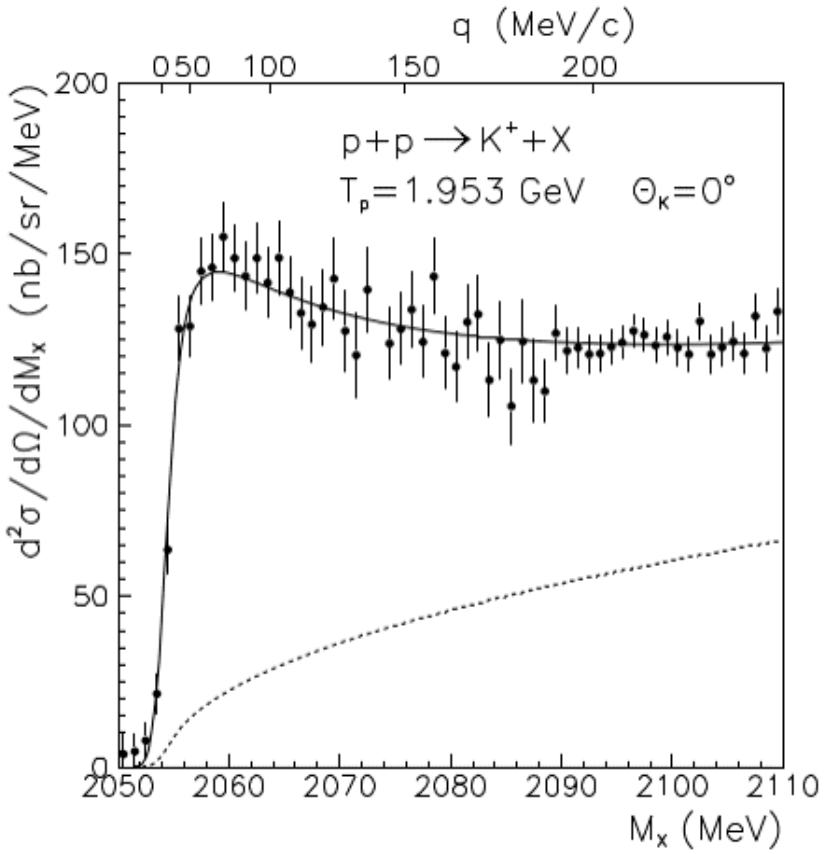

Figure 1.4: Double differential cross section of missing mass with the $p + p \rightarrow K^+(\Lambda p)$ reaction at $T_p = 1.953$ GeV and $\Theta_K = 0°$ [28]. The bottom and top horizontal axes show missing mass from $p + p \rightarrow K^+(\Lambda p)$ and the c.m. momentum q of the Λp system. Solid lines shows fitting result with six-parameters (Eq. 1.4). Dashed line is $p + p \rightarrow K^+(\Lambda p)$ phase space distribution.

nucleons having a momentum distribution are observed as a continuous energy states (Quasi-free (QF) distribution). Fig. 1.5 shows the missing mass distribution in the $^3\mathrm{He}(e, e'K^+)X$ reaction. The peak around 2.99 GeV is a bound state of $^3_\Lambda\mathrm{H}$, and the other events represent Λ-QF production [29]. The black dot points shows the missing mass spectrum of the $^3\mathrm{He}(e, e'K^+)X$ reaction. The hatched magenta area shows the missing mass spectrum obtained by Monte Carlo simulation (SIMC) which is JLab standard simulation code, and the hatched blue area shows the missing mass spectrum including the FSI effects. The FSI effect was introduced in MC simulation by solving two-body scattering problem (discussed in Sec. 1.2.3). The scattering amplitude of FSI was obtained by fitting the missing mass spectrum obtained from MC simulation including FSI.

1.3 Λ production reactions

Λ hypernuclei were produced from the reactions such as (K^-, π^-), (π^+, K^+) and $(e, e'K^+)$. The schematic drawing of these reactions are shown in Fig. 1.6. In the (K^-, π^-) reaction process,

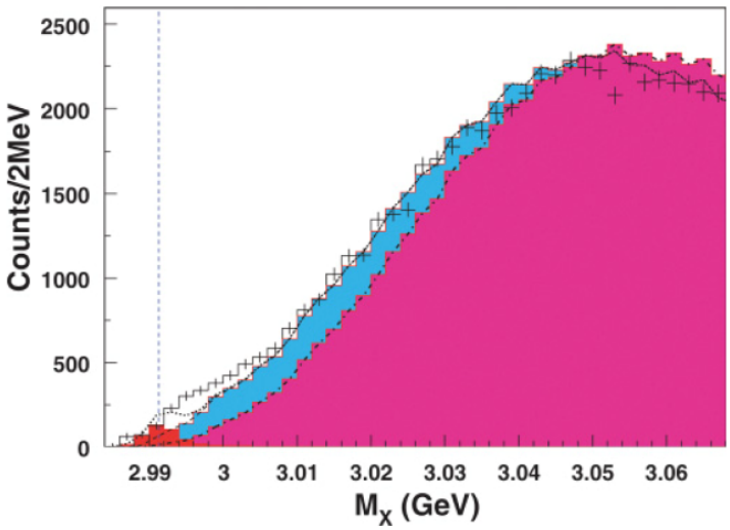

Figure 1.5: A ^{3}He(e, e′K^{+})$^{3}_{\Lambda}$H missing mass spectrum [29]. The horizontal axis is missing mass and the vertical axis. The black dot point shows missing mass spectra of ^{3}He$(e, e'K^{+})X$ reaction. The red hatched area shows $^{3}_{\Lambda}$H events.The blue and magenta hatched areas indicated calculation of Λ QF with FSI and without FSI, respectively. Including FSI distribution success to reproduce enhancement in a range between 2.99 and 3.03 GeV/c^2.

$\Lambda(uds)$ is produced by exchanging an s-quark in $K^{-}(s\bar{u})$ with a u-quark in a neutron in the target $(K^{-}(s\bar{u})+n(udd) \rightarrow \pi^{-}(d\bar{u})+\Lambda(uds))$. Hence, the cross section of Λ hypernuclei is mb/sr order which is larger than the other reactions, because the strange exchange reaction such as the (K^{-}, π^{-}) reaction can easily produced a Λ than $s\bar{s}$ pair production process. Additionally, the (K^{-}, π^{-}) reaction has characteristic of a low momentum transfer. In the case of K^{-} beam momentum at 500 MeV/c (Magic momentum), the reaction gives no momentum transfer. The reactions of (π^{+}, K^{+}) and $(e, e'K^{+})$ produce a Λ with the $s\bar{s}$ pair production process. They are endothermic reaction so beam energies need to be higher than an energy the threshold of Λ production (900 MeV/c). These reactions give high momentum transfer to Λ ($\sim$ 400 MeV/c) so these reactions is suitable for the study of the excited state of heavy Λ hypernuclei or deep bound states. The cross section for hypernuclear production by the (π^{+}, K^{+}) and $(e, e'K^{+})$ reactions are of the order of 10 μb/sr and 100 nb/sr, respectively.

1.3.1 Histrical background

In 1960's, light Λ hypernuclei ($A \leq 16$) were observed by using (K^{-}, π^{-}) reaction and emulsion stack in CERN[*1] and BNL[*2]. Λ hypernuclei in ground state were produced from ^{A}Z$(K^{-}, \pi^{-})^{A}_{\Lambda}$(Z − 1) reaction process, and were identified by measured vertex from the tracking of week decayed particles in emulsion stack. The tracking was appeared by an energy deposit of a charged particle in emulsion so the momentum of decayed particles were precisely deduced

[*1] European organization for Nuclear Research
[*2] Brookhaven National Laboratory

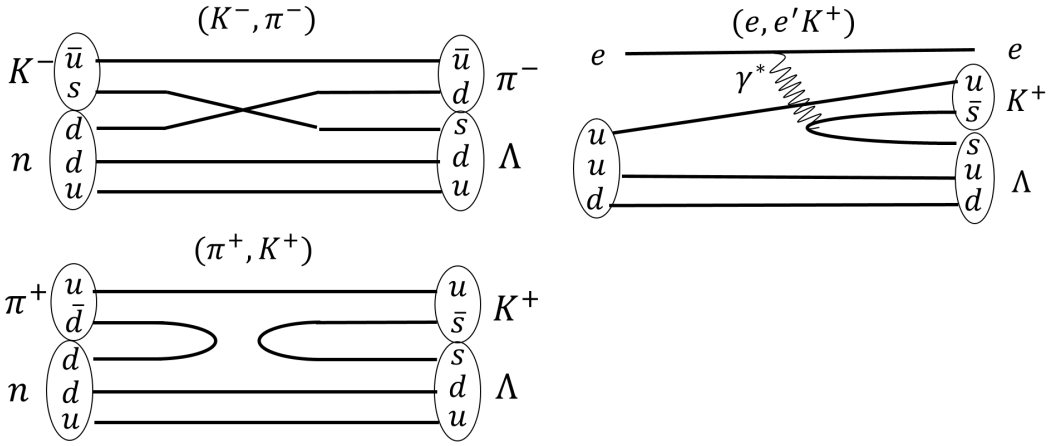

Figure 1.6: The schematic figures of basic elementary reactions for Λ production.

from tracking lengths. Owing to emulsion experiment, the strength of ΛN potential is known as two third of NN potential. However, emulsion experiment cannot study of excited state of Λ hypernuclei. In 1970s, the experiments using counter with (K^-, π^-) reaction were established at CERN or BNL, and this experimental method enabled to measure an excited state of Λ hypernuclei. The p-shell state of Λ hypernuclei were able to be observed by counter experiments, the Λ spin orbit splittings were known to be small comparing with nucleus [30]. The (K^-, π^-) experiment brought about many achievements to hypernuclear physics, but the intensity and quality of K^- beam are low so the yield of Λ hypernuclei is small. Thereafter, KEK established γ-ray spectroscopy method, and transition energies from excited state were able to be measured with high resolution at a few MeV in FWHM [31].

In 1980s, the (π^+, K^+) reaction experiment was developed at BNL [32]. Additionally, High energy accelerator research organization (KEK) were successful in a high resolution spectroscopy owing to Superconducting Kaon Spectrometer(SKS) [33, 34].

1.3.2 Λ hypernuclear experiment with the $(e, e'K^+)$ reaction

The $(e, e'K^+)$ reaction was thought was not suitable for Λ hypernuclei measurement because the cross section about the $(e, e'K^+)$ reaction is 10^{-3} times smaller than other reactions and much background derived from bremsstrahlung was expected to contaminate at forward angle between incoming and scattered electrons ($\theta_{ee'} \sim 0°$). However, in 2000, the first Λ hypernuclei experiment with $(e, e'K^+)$ reaction was performed at JLab Hall C, and succeeded in achieved sub MeV (FWHM) resolution (Fig. 1.8) because electron beam using the reaction can be accelerated directory and controlled with small energy spread ($\Delta E/E \sim 10^{-4}$) and beam size ($\sigma \sim 0.1$ mm). Moreover, high current electron beam (85 μA) compensates for low cross section so thinner target ~ 0.1 g/cm^2 comparing with other experiment (g/cm^2) can be used. Hence, the systematical

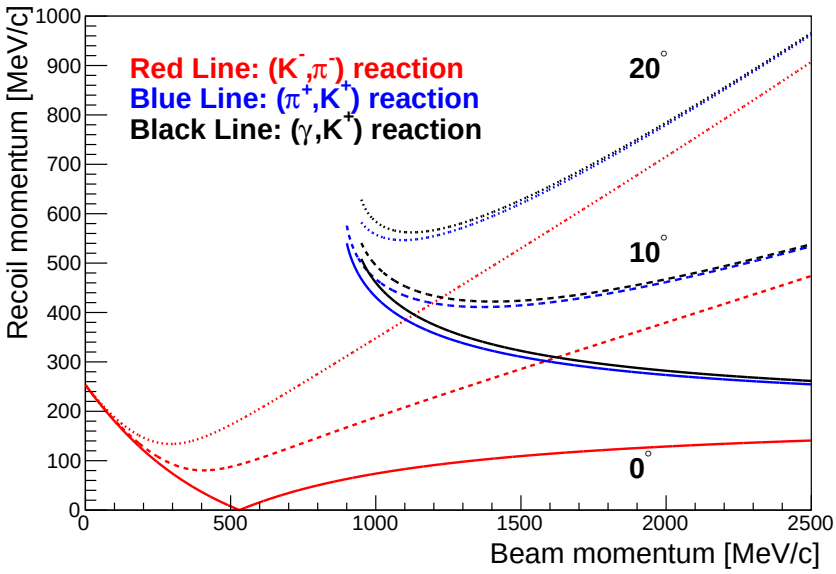

Figure 1.7: The Momentum transfer to Λ depending on beam momenta. There show nine lines combinations of three reactions (red :(K^-, π^-), blue:(π^+, K^+) and black:$(e, e'K^+)$) and three differential opening angles(θ) between beam and recoil Λ(0°:solid line, 10°:dashed line and 20°: dotted line). (π^+, K^+) and $(e, e'K^+)$ reaction have Λ production threshold because of endothermic reactions. In the (K^-, π^-) reaction, there are local minimum value. Especially, at the forward angle (0°) between beam and Λ in (K^-, π^-) reaction, the magic momentum which is beam momentum where the recoil Λ momentum is zero, is exist ($\sim 500\mathrm{MeV}/c$).

error coming from energy loss and straggling effects can be reduced.

1.4 $nn\Lambda$ state problem

The Λp interaction was determined from the Λp (elastic and inelastic) scattering data and binding energies of Λ hypernuclei. On the other hand, the Λn interaction was evaluated with Λp scattering data on the assumption of charge symmetries because there is no Λn scattering data. Additionally, it is difficult to be derived from the effective Λn interaction obtained from spectroscopy of a Λ hypernuclei which are complex systems with protons. The $nn\Lambda$ system is no charged and simple system so it is ideal to study the Λn interaction. However, $nn\Lambda$ was believed not to be bound and no one observed it before the publication about the $nn\Lambda$ by the HypHI collaboration at GSI. In the A=3 Λ hypernuclear system, only ${}^{3}_{\Lambda}\mathrm{H}$ ($I = 0$) was observed and the binding energy of $-B_\Lambda = 0.13 \pm 0.05$ MeV was measured by emulsion experiment [36] (see Fig. 1.9). Considering that a Λ of ${}^{3}_{\Lambda}\mathrm{H}$ is bound shallowing, the isospin triplet ($I = 1$) in the A=3 hypernuclear system (${}^{3}_{\Lambda}\mathrm{H}$, ${}^{3}_{\Lambda}\mathrm{He}$, ${}^{3}_{\Lambda}\mathrm{n}$) are thought not to be bound.

In 1959, R.H. Dalitz calculated three-body Λ hypernuclei with the variational method [37]. The wave function in this model was described with a trial function with six free parameters. As a result of calculation, this theoretical model suggested that the existence of bound states

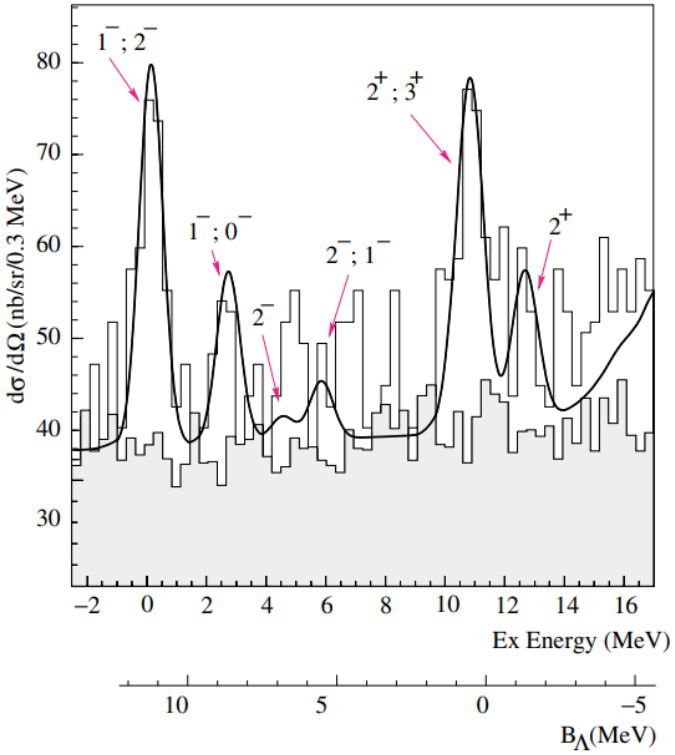

Figure 1.8: A $^{1}2\mathrm{C}(e,e'K^{+})^{12}_{\Lambda}\mathrm{B}$ missing mass spectrum with energy resolution of 0.9 MeV (FWHM) [35].

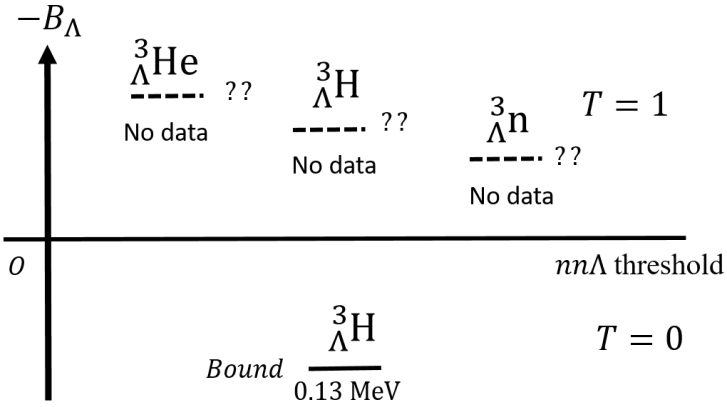

Figure 1.9: A level scheme of hypernuclear system in A=3

for $T = 1$ systems of the ΛNN is unrealistic. Afterwards, K. Miyagawa calculated the ΛNN system with Faddeev equations [38]. This theoretical calculation used Nijmegen potential for the ΛN interaction and the realistic NN interactions including the $\Lambda\Sigma$ conversion effect which is attractive force. This theoretical model with parameters, which were adjusted to reproduce the Λ binding energy of $^{3}_{\Lambda}\mathrm{H}$ in the $T = 0$ system, suggests that $T = 1$ systems of ΛNN are unbound. Based on such a historical background, the $nn\Lambda$ system was thought not to be bound.

In 2013, HypHI collaboration at GSI published the paper that they measured $t + \pi^{-}$ from $nn\Lambda \rightarrow t + \pi^{-}$ channels [39]. However, theoretical calculations cannot reproduce the bound

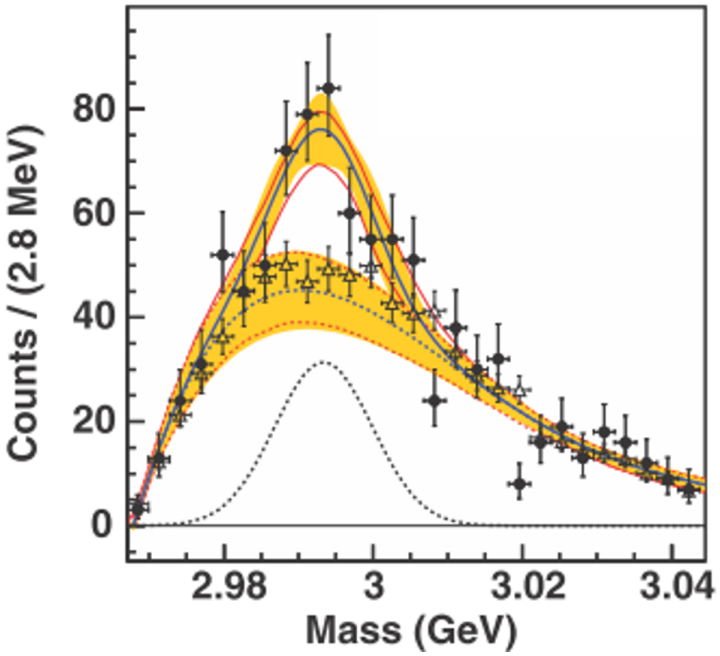

Figure 1.10: Invariant mass distribution of $t + \pi^-$. The horizontal axis shows invariant mass of $t + \pi^-$ observed by the HypHI collaboration at GSI [39]. The black filled circles shows the experimental data. There is structure around $nn\Lambda$ threshold (2.99 GeV) on background (open triangle), which was obtained by the mixed events analysis. The hatched orange region represents one standard deviation of the fitted model centered at the solid blue line of the total best fit.

state of $nn\Lambda$, and the result of the GSI experiment does not have enough peak significance to establish the bound state of $nn\Lambda$. In this section, more detail of the experimental result at GSI (Sec. 1.4.1) and theoretical discussion on $nn\Lambda$ (Sec. 1.4.2) will be explained.

1.4.1 Search for evidence of $nn\Lambda$ at GSI

GSI Helmholtzzentrum für Schwerionenforschung GmbH (GSI) is a heavy ion accelerator facility in Germany. The HypHI collaboration performed HypHI Phase0 experiment, which measured final state of $\pi^- + t$ and $\pi^- + d$ from ^{6}Li beam on the ^{1}2C target.

In 2013, they reported that candidate of the $nn\Lambda$ bound state was measured by lifetime and invariant mass of a final state of the $\pi^- + t$. Figure 1.10 shows that a $t + \pi^-$ invariant mass spectrum measured at GSI. There are some events on the $nn\Lambda$ mass threshold ($m_{2n+\Lambda} = 2.9948$ GeV/c^2) whose mean value was obtained by fitting at ($m = 2994.3 \pm 1.1 \pm 2.2$) MeV/$c^2$. Additionally, as the result of flight length measurement of the nucleus before $t + \pi^-$ decay, these lifetime was obtained as $\tau = 190^{+47}_{-35} \pm 36$ which is comparable with a typical lifetime of Λ hypernucleus ($\tau \sim 200$ ps). Hence, the result suggests that $t + \pi^-$ events were originating from the weak decay of the bound state of $nn\Lambda$.

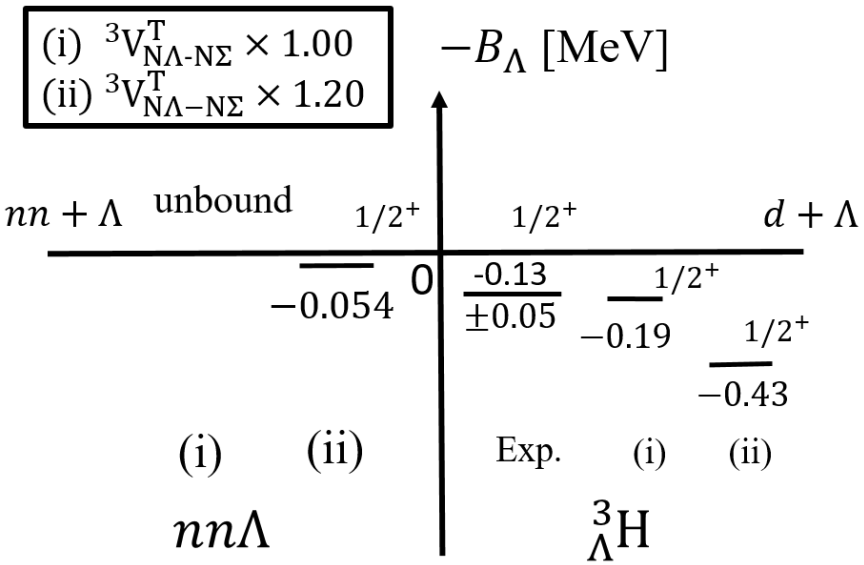

Figure 1.11: The binding energy calculation with Gaussian expansion method for ${}^{3}_{\Lambda}$H and $nn\Lambda$ with (i) ${}^{3}V^{T}_{N\Lambda-N\Sigma} \times 1.0$ and (ii) ${}^{3}V^{T}_{N\Lambda-N\Sigma} \times 1.2$ [40]. The ${}^{3}V^{T}_{N\Lambda-N\Sigma}$ is tensor term of the YN interaction which is used for scattering phase shifts given by NSC97f with $N\Lambda - \Sigma N$ coupling effect. In the case of (i) ${}^{3}V^{T}_{N\Lambda-N\Sigma} \times 1.0$, calculation of Λ binding energy in the ${}^{3}_{\Lambda}$H system is comparable with experimental result within experimental error. However, the $nn\Lambda$ indicates unbound state. In the case of (i) ${}^{3}V^{T}_{N\Lambda-N\Sigma} \times 1.2$, $nn\Lambda$ is bound narrowly, but calculation of Λ binding energy in the ${}^{3}_{\Lambda}$H system indicates over bound ($-B_\Lambda = -0.43$ MeV) comparing with experimental results. This result implied bound state of $nn\Lambda$ is unrealistic.

1.4.2 Theoretical discussion

The HypHi collaboration observed a possible bound state of $nn\Lambda$. On the other hand, theoretical calculations cannot reproduce the bound state of $nn\Lambda$.

■ **Hiyama** *et al.,* **(2014) [40]**

The binding energy of three and four body hypernuclei, ${}^{3,4}_{\Lambda}$H and ${}^{4}_{\Lambda}$He, were reproduced by theoretical calculation with the Gaussian expansion method [40]. The theoretical model used the NSC97f potential including the $\Lambda N - \Sigma N$ effects and the AV8 potential for the ΛN and NN interactions, respectively. Fig.1.11 shows results of Gaussian expansion calculation for binding energies of ${}^{3}_{\Lambda}$H and $nn\Lambda$. The (${}^{3}V^{T}_{N\Lambda-N\Sigma}$) is tensor term for the ΛN interaction. Figure 1.11 (i), which is optimized for binding energies of ${}^{3,4}_{\Lambda}$H and ${}^{4}_{\Lambda}$He, reproduces the energy of the $1/2^+$ state of ${}^{3}_{\Lambda}$H. On the other hand, $nn\Lambda$ was suggested to be unbound state. When the term of (${}^{3}V^{T}_{N\Lambda-N\Sigma}$) increases 20% (Fig. 1.11 (ii)), the $nn\Lambda$ is bound shallowly, but $1/2^+$ state of ${}^{3}_{\Lambda}$H is bound too deeply. Therefore, the theoretical calculation suggests that the bound state of $nn\Lambda$ system is hardly understood.

■ **I.R. Afnan** *et al.,* **(2015) [41]**

On the one hand, Faddeev calculation with the separable potential suggests that $nn\Lambda$ could be resonance state when a potential of Λn is 5% deeper than that of Λp [41]. Fig. 1.12 shows the resonance pole trajectories on second Riemann sheets with four different Λn potentials, Nijimeden model D (Mod D), Chiral ($\Lambda = 600$) (Chiral), Nijmegen NSC97f (NSC97f) and Jülich one bosson exchange potential (Jülich04). The horizontal and vertical axes are real and imaginary parts of binding energy for $nn\Lambda$, and the resonance poles are plotted with increasing every 2.5% ($\Delta s = 0.025$) of strength for the Λn potential from the Λp potential ($s = 1$). In case of increasing Λn interaction more than 5 % every potential models, resonance poles locate in $\Re(E) > 0$ which indicates that $nn\Lambda$ is resonance state. Moreover, when the Λn interaction is increased more than 25%, the $nn\Lambda$ is expected to be bound state for all potential models. Considering no Λn scattering data exists, the 5 % difference ($\Delta s \sim 5\%$) of the Λn potential from strength of Λp potential is within the systematical error so this theoretical calculation suggests that there is some possibility of the $nn\Lambda$ resonance state.

■ **V.B. Belyaev** *et al.,* **(2008) [43]**

Belyaev searched for a resonance state of $nn\Lambda$ by calculating the zeros of a three-body Jost function. As the NN potential, the Minnesota potential model was used, which accurately

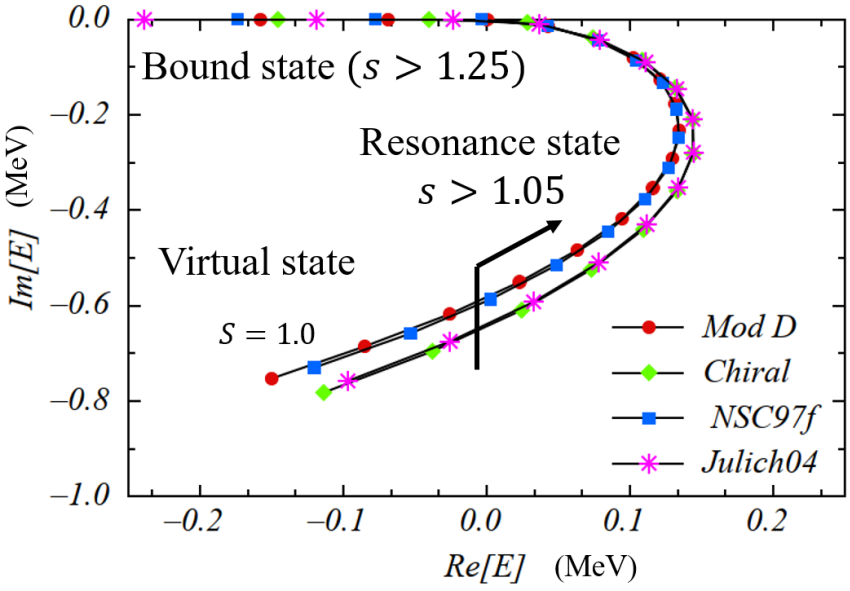

Figure 1.12: Trajectory of the resonance poles in the $nn\Lambda$ system as one varies the strength of the Λn interaction [41]. There are four curves with different Λn potentials correspond to Yamaguchi fits: Mod D for Nijmegen model D, Chiral for chiral ($\Lambda = 600$), NSC97f for Nijmegen NSC97f and Jülich04 for Jülich one boson exchange potential. These models were used the same nn potential [42].

reproduces the radii and binding energies of few-nucleon systems such as ^{2}H, ^{3}H, ^{3}He and ^{4}He. The ΛN interaction was constructed produced by using the NN potential model (Minnesota model), since the ΛN potential is considered to be similar to the NN potential due to the $\mathrm{SU_f}(3)$ symmetry. Nemura proposed three different Λn potentials (Set A, B and C) [44], and the S-wave Λn potentials of these models were shown in Fig. 1.13. There potential parameters were obtained by fitting the binding energies of 3,4-body Λ hypernuclei ($^{3,4}_{\Lambda}$H, $^{4}_{\Lambda}$He) and of excited state of 4-body Λ hypernuclei ($J^{+} = 1^{+}$) such as $^{4}_{\Lambda}$H*, $^{4}_{\Lambda}$He*. It has been experimentally suggested that a charge symmetry of the ΛN interaction is broken (CSB) in the 4-body Λ hypernuclei [45], and set A is the model that takes into account the CSB effect. The complex energies ($E = E_r - (i/2)\Gamma$) of $nn\Lambda$, which were calculated from the three different Λn potential models, were summarized in Tab. 1.4. In the cases of set A and B, there were resonance states of a wide range width of ~ 5 MeV, but in set C, there was not resonance state.

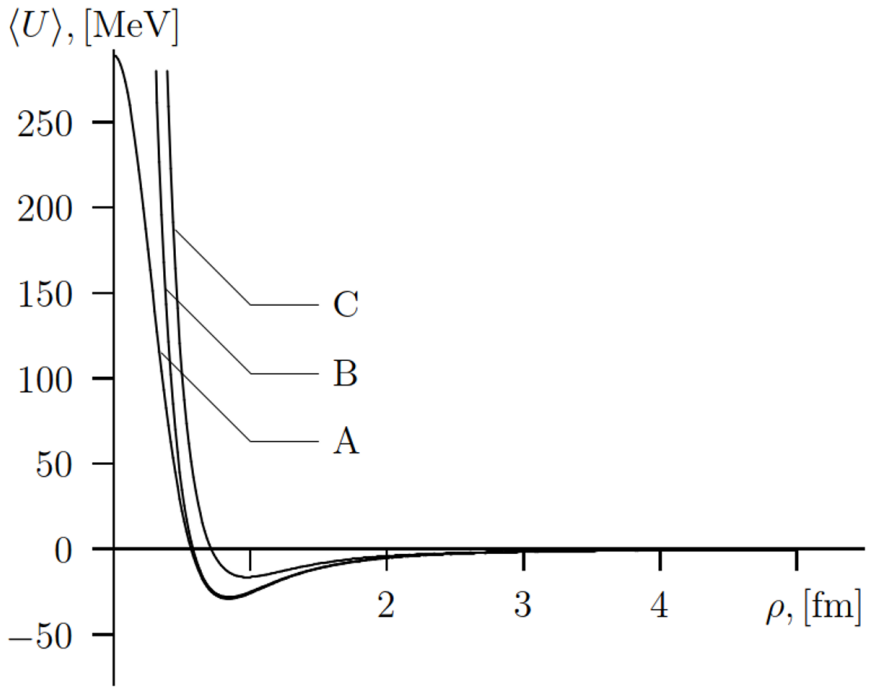

Figure 1.13: The three different Λn potentials, A, B and C are shown [44].

Table 1.4: Complex resonance energies ($E_0 = E_r + (i/2)\Gamma$ MeV) for $nn\Lambda$ system with three different potentials, A, B, and C [43]

Λn potential	E_r (MeV)	Γ (MeV)
A	0.551	4.698
B	0.456	4.885
C	-0.149	5.783

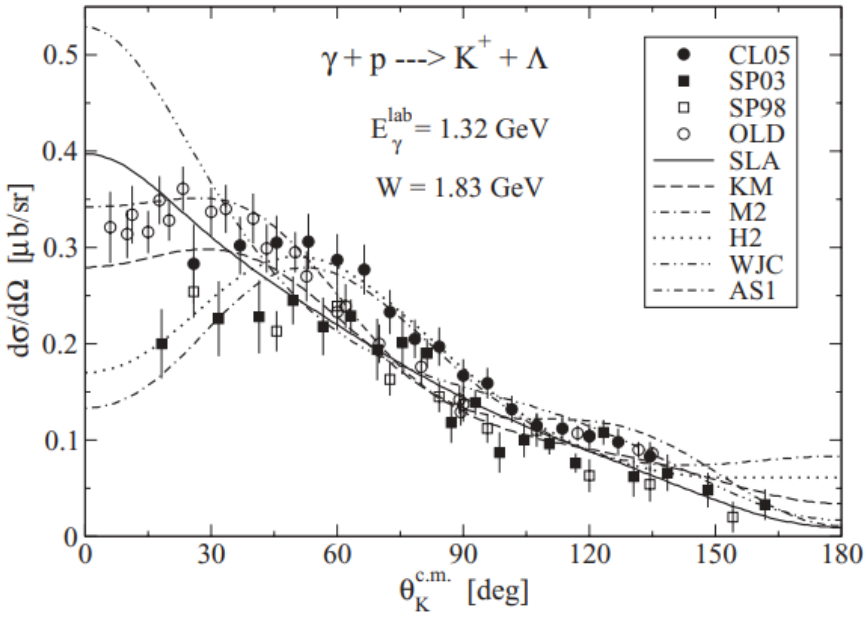

Figure 1.14: The differential cross section depending on K^+ opening angle in the center of mass frame for data of CLAS [46], SAPHIR [47] and an older one [48, 49] and theoretical calculations [50].

1.5 Purpose of the present research

1.5.1 Elementary productions of $p(e, e'K^+)\Lambda/\Sigma^0$

Λ and Σ^0 productions from a hydrogen target were used for energy calibration. This is a merit of the $(e, e'K^+)$ reaction and it enables us to achieve high resolution. Moreover, E12-17-003 experiment measured Λ and Σ^0 cross sections at forward angles ($\theta_{\gamma K} \sim 8°$) between a K^+ and virtual photon where there are only (Fig. 1.14) and sensitive to theoretical models. In the case of forward angles ($\theta_{\gamma K} \sim 8°$), the virtual photons can be approximately treated as real photons. Therefore, the measured the cross sections of Λ and Σ^0 at forward angles by this experiment can constrains theoretical models.

1.5.2 $^3\mathrm{H}(e, e'K^+)nn\Lambda$

■ **$nn\Lambda$ peak study**

HypHI Collaboration at GSI observed events which indicates a bound state of $nn\Lambda$, but there is not enough peak significance. The theoretical calculation with Faddev equation (see 1.4.2) suggests that there is possibility to be resonance state of $nn\Lambda$ within the systematical error. If the $nn\Lambda$ is bound or resonance state, a peak of $nn\Lambda$ can be observed. By using high resolution spectroscopy with a sensitivity to a bound and resonance states in the $(e, e'K^+)$ reaction, we performed the experiment (E12-17-003) at JLab in order to search for a $nn\Lambda$ peak. If the $nn\Lambda$

peak is observed in the missing mass spectrum, the state of $nn\Lambda$ can be identified by the sign of the binding energy, ($0 < -B_\Lambda$: resonance state, $-B_\Lambda < 0$: bound state). Additionally, the mean and width of the $nn\Lambda$ peak are corresponding to ($\Re[E]$) and ($\Im[E]$) parts of the binding energy on the second Riemann sheet (Fig. 1.12). Hence, the resonance state is observed the expected energy accuracy of $\sigma_{nn\Lambda} \sim 100$ keV and total error of energy resolution $\Delta\mu_{nn\Lambda} \sim 100$ keV of this experiment determine the Λn interaction with an accuracy of 5% by comparing with the theoretical predictions in the second Riemann sheet (Fig. 1.12).

■ **Λn final state interaction study from Λ quasi free production**

In this experiment, the Λ quasi free (Λ-QF) production events in $^3\mathrm{H}(e, e'K^+)X$ reaction can be obtained. The final state interaction effect in three body Λ hypernuleus ($^3_\Lambda\mathrm{H}$) was confirmed to be appeared in mass threshold of Λ hypernucleus. The Λn FSI effect is expected to be appeared to the Λ-QF spectrum in the $^3\mathrm{H}(e, e'K^+)X$ reaction, too. In this thesis (Sec. 5), the Λn FSI will be studied from the cross section spectrum about Λ-QF production in the $^3\mathrm{H}(e, e'K^+)X$ reaction.

Chapter 2 Experimental principle

The present experiment (JLab E12-17-003) was performed from October to November in 2018 at Jefferson Lab (JLab) Hall A. The experiment aims to an observation of a state of $nn\Lambda$ with the $(e, e'K^+)$ reaction. Momenta of kaons (K^+) and scattered electrons (e') were measured with two High Resolution Spectrometers (HRSs) in the experiment which are permanently installed at Hall A.

2.1 Principle and design

2.1.1 Kinematics of the $(e, e'K^+)$ reaction

The $(e, e'K^+)$ reaction, which produces a Λ hyperon from a proton by a virtual photon, is one of the Λ hypernuclear production methods. By comparison with the other mesonic reactions:(K^-, π^-) and (π^+, K^+), the $(e, e'K^+)$ reaction enables us to perform high resolution and high accuracy spectroscopy (sub MeV), because it is possible to use high quality and high intensity beam and to calibrate the spectrometer optimization with elementally reaction $\mathrm{H}(e, e'K^+)\Lambda/\Sigma^0$. The kinematics of the $(e, e'K^+)$ reaction is shown in Fig.2.1. There are two reaction planes: the scattering plane and reaction plane. In the scattering plane, four momentum of the virtual photon $q = (\omega, \vec{q})$ is described with four-momenta of a beam electron $p_e = (E_e, \vec{p_e})$ and scattered electron $p_{e'} = (E_{e'}, \vec{p_{e'}})$:

$$\omega = E_e - E_{e'} \ , \tag{2.1}$$

$$\vec{q} = \vec{p_e} - \vec{p_{e'}} \ . \tag{2.2}$$

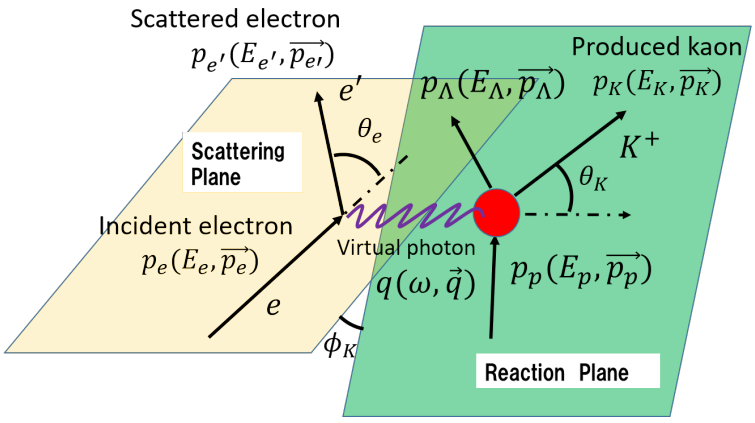

Figure 2.1: The elementary reaction $p(e, e'K^+)\Lambda$

Kinematics of a K^+ and Λ are calculated in the reaction plane as follow :

$$\omega + E_p = E_K + E_\Lambda \ , \tag{2.3}$$
$$\vec{q} + \vec{p_p} = \vec{p_K} + \vec{p_\Lambda} \ . \tag{2.4}$$

In the case of hypernuclear spectroscopy by an electron beam with GeV scale, the momentum of a proton by a molecular motion of hydrogen can be ignored ($\vec{p_p} \ll \vec{q}$) in Eq. 2.4. The four momentum transfer ($Q = \sqrt{-q^\mu q_\mu}$) can be described as follows:

$$Q^2 = 2(E_e E_{e'} - m_e^2 - |\vec{p_e}||\vec{p_{e'}}|\cos\theta_{ee'}) \tag{2.5}$$

where $\theta_{ee'}$ is the angle between electron beam and scattered electron. The differential cross section in elementally reaction $(p(e, e'K^+)\Lambda)$ is defined as [51]:

$$\frac{d^3\sigma}{dE_{e'}d\Omega_{e'}d\Omega_K} = \Gamma(\frac{\sigma_T}{d\Omega_K} + \epsilon_L\frac{d\sigma_L}{d\Omega_K} + \epsilon\frac{d\sigma_{LT}}{d\Omega_K}\cos 2\phi_K + \sqrt{2\epsilon_L(1+\epsilon)}\frac{d\sigma_{TT}}{d\Omega_K}\cos\phi_K), \tag{2.6}$$

where the terms of $\sigma_T,\ \sigma_L,\ \sigma_{LT}$, and σ_{TT} are the transverse, longitudinal and interference cross sections. The virtual photon flux (Γ) is described as :

$$\Gamma = \frac{\alpha}{2\pi^2 Q^2}\frac{E_\gamma}{1-\epsilon}\frac{E_{e'}}{E_e} \ , \tag{2.7}$$

where the fine structure constant ($\alpha \simeq 1/137$) and $Q^2 = -q^2 > 0$.

The virtual photon transverse polarization (ϵ), longitudinal polarization (ϵ_L) and E_γ are represented by:

$$\epsilon = \left(1 + \frac{2|\vec{q}|^2}{Q^2}\tan\theta_{ee'}/2\right)^{-1} \ , \tag{2.8}$$
$$\epsilon_L = \frac{Q^2}{\omega^2}\epsilon \ , \tag{2.9}$$
$$E_\gamma = \omega + \frac{q^2}{2m_p} \ . \tag{2.10}$$

In the case of real photon, the polarized transverse terms (ϵ, ϵ_L) is zero since $Q^2 \to 0$.

2.2 Experimental design

In the $(e, e'K^+)$ reaction, Λ hypernuclei are produced by one virtual photon exchange model. When optimizing an efficient experimental setup, spectrometers were set to measure the maximize yield of Λ hypernuclei, especially $K^+\Lambda$ and $K^+\Sigma^0$ photo-productions. Fig.2.2 and 2.3 show cross sections of $K^+\Lambda$ and $K^+\Sigma^0$ photo-production by experimental result by CLAS [52]. The experiment was designed to measure K^+ and e' with central momenta $p_K = 1.823$ GeV/c and $p_{e'} = 2.218$ GeV/c, and measure K^+ at forward angles in center of mass coordinate ($\theta_K^{\mathrm{C.M.}} \sim 8°$). Furthermore, the electron beam was used at 4.318 GeV corresponding to the energy of virtual photon $W = E_e - E_{e'}$ of 2.14 GeV, which gave maximum cross section in $K^+\Lambda$ and $K^+\Sigma^0$ ($d\sigma^\Lambda/dcos(\theta_K^{\mathrm{C.M.}}) \sim 2\ \mu$b and $d\sigma^\Sigma/dcos(\theta_K^{\mathrm{C.M.}}) \sim 1.5\ \mu$b, respectively).

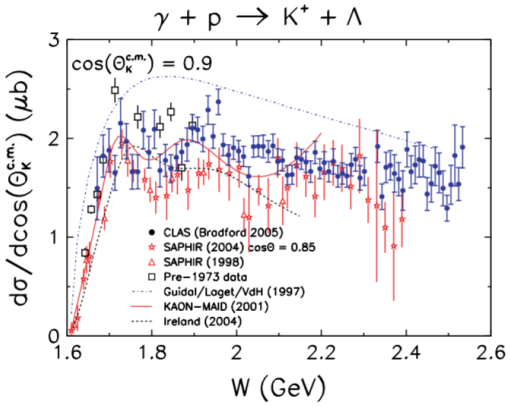

Figure 2.2: Experimental results and theoretical calculation of the cross section of $K^+\Lambda$ photo production at $\cos\theta_K^{C.M.} = 0.9$ [52]

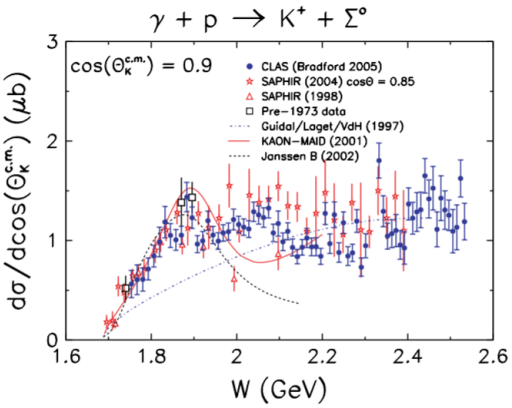

Figure 2.3: Experimental results and theoretical calculation of the cross section of $K^+\Sigma^0$ photo production at $\cos\theta_K^{C.M.} = 0.9$ [52].

2.2.1 Momentum matching in HRS-HRS

The experiment was designed to measure $nn\Lambda$ in HRS acceptance range. Fig. 2.4 shows momentum correlations between scattered electrons (e') and K^+s. In the experimental setup for $nn\Lambda$ with central momentum of scattered electrons at 2.213 GeV/c, Λ and Σ^0 were not observed simultaneously because Σ^0 missing mass was edge of HRS acceptance region which is insensitive. Therefore, when energy calibration data with hydrogen was performed, the central momentum of scattered electron was shift to 2.100 GeV/c for covering Λ and Σ^0 missing mass region within the sensitive region in HRSs.

2.3 Data taking

This experiment was performed from October 30th to November 25th, 2018. The quantity of electronic charge of the irradiated beam was measured by the beam current monitor (BCM), and the total charges irradiated to targets were summarized in Tab. 2.1. The error of the beam charge in Tab 2.1 was evaluated based on the accuracy of the BCM (see Sec. 3.2.3). The experiment used electron beam at 22.5 μA during experimental period (27 days). Since the total charge of electrons measured by the BCM was 23.4 C, the efficiency of data acquisition was about 45%. The ^{3}H target was used for $nn\Lambda$ productions by the $^3\mathrm{H}(e, e'K^+)X$ reaction, and was irradiated with the electron beams of 16.8$\pm$0.2 C. The ^{1}H target was used to measure the hyperons such as Λ and Σ^0 for the momentum calibration (see Sec. 4.2.7). In this experiment, the ^{1}H data were taken in the two kinematics, $(p_{e'}, p_K) = (2.100, 1.823)$ GeV/c and $(p_{e'}, p_K) = (2.213, 1.823)$ GeV/c. The total charges of electron beams at each momentum set were 4.75 $\pm$ 0.05 and

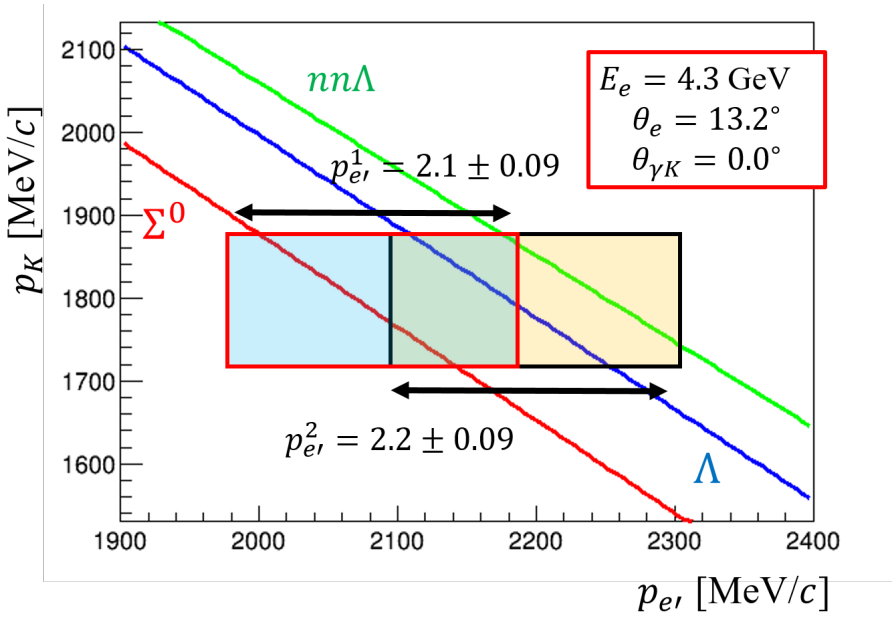

Figure 2.4: The momentum correlations between scattered electrons(e') and K^+s. Three lines shows the correlations for binding energies about Λ, Σ^0 and $nn\Lambda$. The $nn\Lambda$ data was taken with the central momentum of scattered electron at 2.218 GeV/c. However, in Λ and Σ^0 data, the central momentum of scattered electrons were changed to 2.100 GeV/c since Λ and Σ^0 need to be measured simultaneously for the energy scale calibration.

Table 2.1: Summary of the data taking

Target	production	$(p_{e'}, p_K)$ (GeV/c)	Beam charge (C)
^{3}H	$nn\Lambda$	$(2.2, 1.8)$	16.8 ± 0.2
^{1}H	Λ/Σ^0	$(2.1, 1.8)$	4.75 ± 0.05
^{1}H	Λ	$(2.2, 1.8)$	1.31 ± 0.01
^{3}H	Λ-QF	$(2.2, 1.8)$	0.558 ± 0.006
Optics		$(2.2, 1.8)$	0.531 ± 0.005
Total			23.4 ± 0.4

1.31 ± 0.01 C, respectively. The ^{3}He was contaminated in the ^{3}H target due to β decay of ^{3}H ($^3\mathrm{H} \rightarrow {}^3\mathrm{He} + e^- + \bar{\nu}_e$), and reacted with the electron beam to produce Λ-QF productions as a background (see Sec. 4.6.3). Therefore, 0.558 ± 0.006 C of electron beams was irradiated to ^{3}He target in order to estimate the Λ-QF distribution of the $^3\mathrm{He}(e, e'K^+)X$ reaction. Additionally, the experiment obtained optics data with solids targets (see. Sec. 4.2.4,4.2.5) with a total charge of electron beams at 0.531 ± 0.005 C.

Chapter 3 Experimental Apparatus

3.1 Continuous Electron Beam Accelerator Facility in JLab

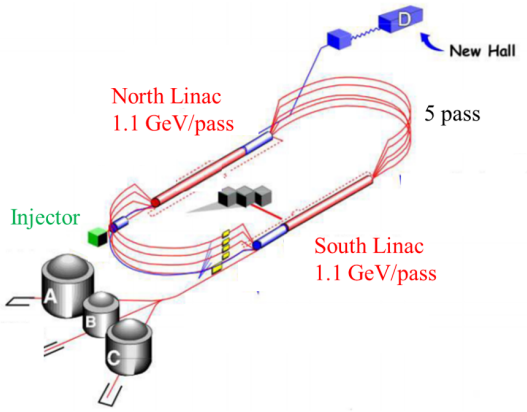

Figure 3.1: A schematic drawing of CEBAF [53]. The CEBAF injector is designed to create and accelerate electrons up to 123 MeV. The accelerated electrons by the injector are transported to the main rings. They are further accelerated by the north and south linacs which give electrons energy of 1.1 GeV for each pass. The CEBAF with five cycles to pass into north and south linacs can provide us electrons energy up to 12 GeV.

Continuous Electron Beam Accelerator Facility (CEBAF) in JLab provides us an electron beam with a high quality and intensity. Fig. 3.1 shows a schematics drawing of CEBAF in JLab. Electrons are generated in the injector, and transported to a main ring with energies of 123 MeV. The transported electrons are accelerated by the south and north linacs with each pass providing energy of 1.1 GeV, and they are transported to each experimental hole, Hall A, B, C and D. The main specifications of CEBAF are summarized in Tab. 3.1. These unique specifications about the electron beam at CEBAF satisfy the following experimental requirements:

Table 3.1: The main beam parameter of the CEBAF [53]

Maximum beam energy(Hall A, B, C)	11 GeV
Maximum beam energy(Hall D)	12 GeV
Maximum beam intensity(Hall A,C/B)	85 μA/5 μA
Beam emittance at max energy H/V	10/2 nm·rad
Energy spread at max energy (Hall A,B,C/D)	2.0 $\times 10^{-4}$
Polarization	80%

Table 3.2: Hall A beam parameters [54]

Parameter	Method		Accuracy	Comments
Energy	Arc	Absolute	2.0×10^{-4}	Invasive
			5.0×10^{-4}	Non-invasive
		Relative	1.0×10^{-4}	Non-invasive
	eP	Absolute	2.0×10^{-4}	Invasive
Energy width	OTR		$\Delta E/E \sim 1.0 \times 10^{-5}$ (σ)	Non-invasive
Current (≥ 1 μA)	2 RF Cavities	Absolute	$\leq 5 \times 10^{-3}$	Non-invasive
Position (at target)	2 BPM/Harp	Absolute	140μm	x,y on line
Direction (at target)	2 BPM/Harp	Absolute	30 μrad	θ, ϕ on line
Stability (at target)	Fast Feedback		$\leq$ 720 Hz motion	
	Position		≤ 20 $\mu m(\sigma)$	
	Energy		$\leq 1 \times 10^{-5}$ (σ)	

■ **High quality** ($\Delta E/E \sim 2.0 \times 10^{-4}$)

The electrons accelerated by CEBAF are characterized by a small energy dispersion of $\Delta E/E \sim 2 \times 10^{-4}$. The beam energy is measured in the Machine Control Center (MCC) (see Sec. 3.2.2) with an accuracy of 10^{-4} (Tab. 3.2). The dispersion of electron beam is comparable level with momentum resolution of spectrometers, and it helps to measure Λ hypernuclei with resolution of $\sim$ MeV (FWHM).

■ **Small beam size** ($\sigma \sim 100$ μm)

The momenta of e' and K^+ at vertex point are reconstructed from the positions and angles at reference plane of spectrometers using an inverse transport matrix. When the beam spot size is large, the accuracy of the reconstructed angle by the inverse transport matrix deteriorates.

Hoever, the size of the electron beam produced by CEBAF at $\sim$100 μm is small enough that it dose not affect the momentum resolution.

■ **High intensity (≤ 85 μA)**

The cross section of the $(e, e'K^+)$ reaction is two to four orders of magnitude smaller the than (π^+, K^+) and (K^-, π^-) reactions [55]. This disadvantage can be covered by using the high intensity beam of CEBAF. Moreover, the high intensity beam makes it possible to use a thin target ($<$ 0.1g/cm) with enough yield of Λ hypernuclei, which is thinner than used targets by other mesonic beam experiments (a few g/cm^2). The thinner target helps to be better momentum resolution since the effect on an energy loss and straggling in the target can be reduced. It is possible to measure Λ hypernuclei with a high resolution and accuracy.

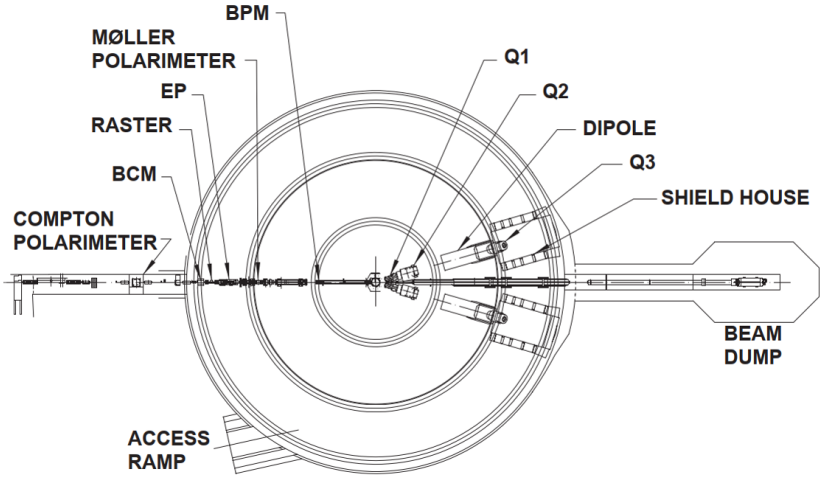

Figure 3.2: A schematics drawing of the Hall A beamline [56]. On the Hall A beamline, the Compton and Møller polarimeters, the raster, the EP energy measurement system, the beam current monitors (BCM) and beam position monitors (BPM) upstream of target. In the end of beamline, beam dump and truck access ramp located.

3.2 Hall A beamline

The accelerated electron beam at CEBAF is transported to Hall A beamline. Upstream of the target, a Compton and a Møller polarimeters, and an EP energy measurement system, beam current monitors (BCM) and beam position monitors (BPM) are installed in Hall A (See Fig. 3.2). In addition, a beam dump and a truck access ramp are installed at the end of the beamline.

3.2.1 Beam position and direction

The raster which is used not to heat up a cryogenic gas target, is controlled in a range of several mm in both x and y directions at the target by a fast raster system (17-24 kHz) located 23 m upstream of the target. A position shift by a raster enables to be calibrated with two Beam Position Monitors (BPMs). BPMs consist of four antennas which are attached to feedthroughs on the pipe wall at the right angle and located 7.524 m and 1.286 m upstream of the target. These four antenas are marked as u_+, u_- and v_+, v_-, respectively whose signals are used to determined u and v positions at target. When an electron beam passed through the BPMs, each antenna detects an induced signal, and sends the signal to the Hall A DAQ system.

The absolute beam positions at target can be determined from BPMs with two super harps which located 7.353 and 1.122 m upstream of the target, respectively. They consist of three wires with a thickness of 50 μm which are arranged a fork frame, and can be moved by a step motor. When the harp fork was moved into beamline, each wire received a signal, and this signal

was recorded to the DAQ. By analyzing recorded signals, an accuracy of the beam position can be achieved 140 μm.

3.2.2 Absolute energy measurements

The Machine Control Center (MCC) monitors the beam energy in the accelerator. In the Arc method, the beam energy is controlled in the the arc section of the beamline by measurement of a bend angle before providing for Hall A beamline. Fig. 3.3 shows arc section. The normal bend angle in the arc section is 34.3°. The beam momentum is depending on the bend angle θ and field integral of the eight dipoles $\int \vec{B} \cdot \vec{dl}/\theta$ Tm which is always monitoring with field measuring device located 9th dipole (see Fig. 3.3). Hence, by the measurement of the actual bend angle of the arc with two super harps, the beam energy can be determined.

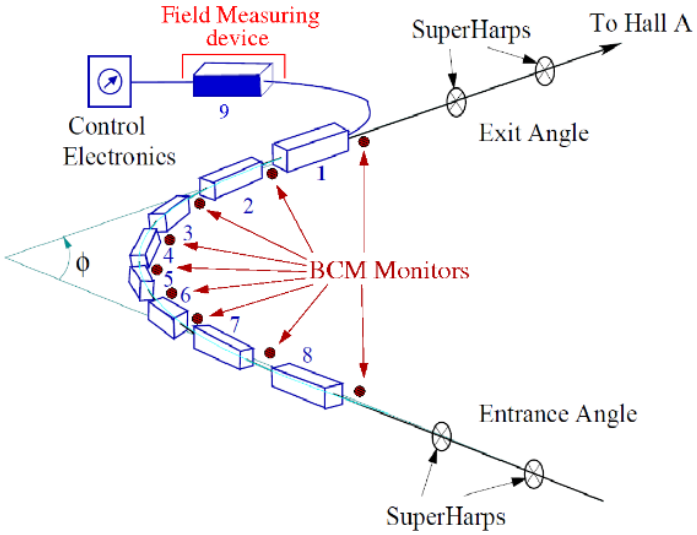

Figure 3.3: A schematics drawing of the arc section [57].

3.2.3 Current and charge calibrations

Beam current is determined by using the Beam Current Monitor (BCM) of Hall A which consists of an Unser monitor, two RF cavities, electronics and data acquisition system. Fig. 3.4 shows beam current instruments. The two RF cavities and Unser located 25 m upstream of the target are sealed by a thermal isolation box for shielding magnetic field. These monitors translate passed charge to frequency of the beam thus they are required of temperature stabilization to reduce noise. In the case of the Unser which is self-calibrated, it cannot be used to continuous monitor of beam current because it is not stable on time scale of several minute. On the other hand, the RF cavity monitors are stable with in $\pm 0.5\%$ during a several months. By using two

types of BCM, the charge in physics run can be determined with an accuracy of $\leq 0.5\%$.

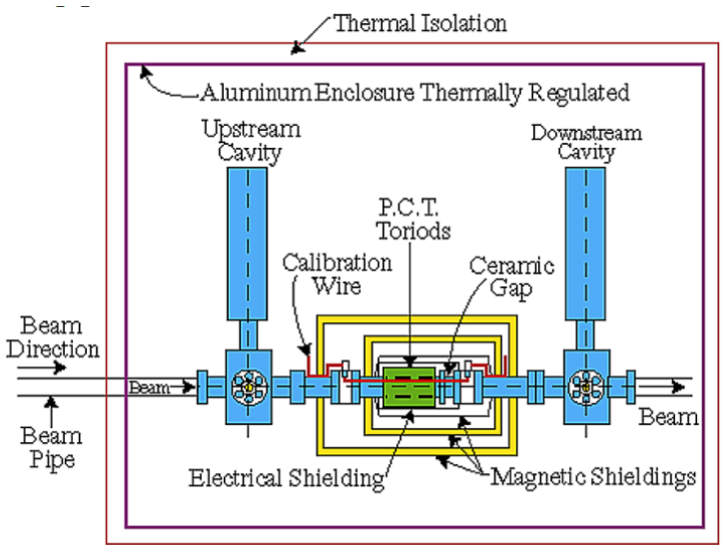

Figure 3.4: A schematics drawing of the beam current instruments from [58].

3.3 E12-17-003 experiment setup

3.3.1 Overview

Fig. 3.5 show E12-17-003 experimental setup with two high resolution spectrometers (HRSs). Angles between beam direction and each of HRS are flexible to change from 12.5 to 130 degree in hadron arm and 12.5 to 165 degree in electron arm, respectively. The main specification of experimental setup is summarized in Table 3.3.

Table 3.3: The experimental condition

Beam (e)	
Energy	4.5 GeV
Energy spread	1.0×10^{-4}
Beam current	25 μA
HRS-HRS	
Configuration	QQDQ
Central momentum ($p_K/p_{e'}$)	1.8 / 2.2 [GeV/c]
Momentum acceptance($\Delta p/p$)	$\pm4.5\%$
Momentum resolution	2.0×10^{-4} (FWHM)
Flight path length	27.3 m
HRS acceptance	$\sim$ 5 msr
HRS setting angle	13.2° / 13.2°

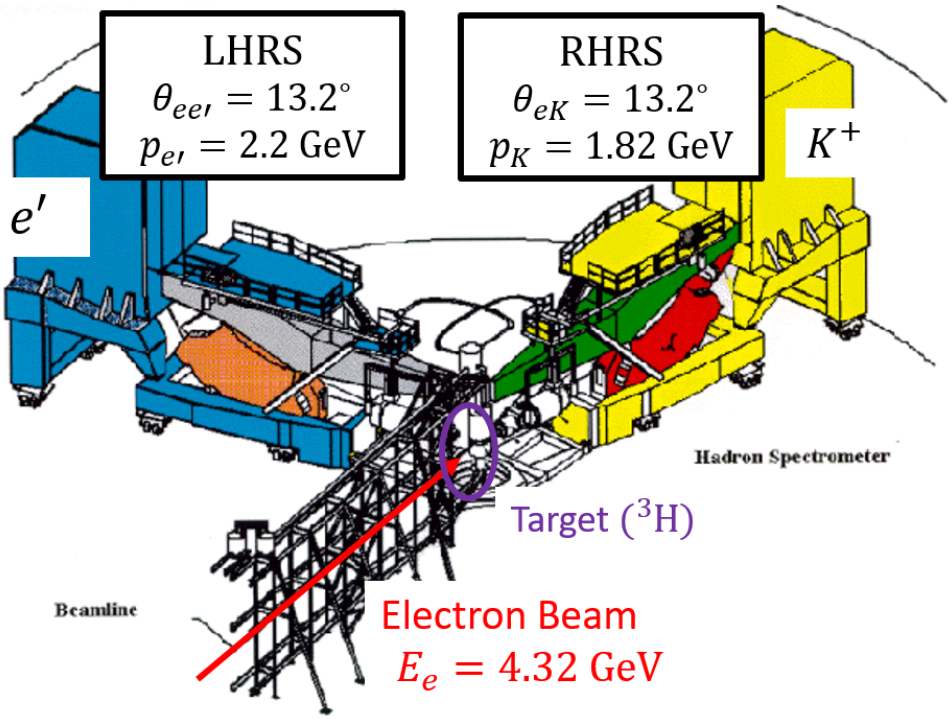

Figure 3.5: A schematics drawing of the standard Hall A setup. E12-17-003 experiment was used an electron beam at 4.3 GeV, and used two HRSs for measurement of K^+ and e' with central momenta $p_K = 1.8$ GeV/c and $p_{e'} = 2.2$ GeV/c, respectively.

3.3.2 High Resolution Spectrometer(HRS)

This experiment was performed by using two high resolution spectrometers (HRSs) for measurement momenta of e' and K^+. The HRS which consists of a detector package, superconducting quadrupole magnets, Q1, Q2 and Q3, and one superconducting dipole magnet (D), is designed to achieve high momentum resolution ($\Delta p/p < 2.0 \times 10^{-4}$) (FWHM). Main HRS specifications are listed in Table 3.3.

■ Superconducting Dipole Magnet (D)

The superconducting dipole magnet (D) is used for momentum dispersion and focusing. The main specification of dipole magnet is summarized in Table 3.4. The maximum current for operating dipole magnet is 2000 A. However, left and right HRSs should not be operated at a current above 1800 A and 1200 A corresponding 4.4 GeV/c and 3.2 GeV/c respectively, due to complications caused by an internal short. The dipole magnet is configured to achieve a 45° bending angle for 4 GeV/c momentum particles when the setting of dipole magnetic field is 1.6 T corresponding to 1500 A of an operating current.

Table 3.4: The specification of HRS dipole magnet

specification	value
Maximum current	2000 A (10 V)
Maximum magnet field	2 T
Effective length	6.6 m
Bend radius	8.4 m
Dending angle	45°

■ **Quadrupole Magnets (Q1, Q2, Q3)**

The HRS consist of three quadrupole magnets (Q1, Q2 and Q3). The Q1 and Q2 locate before the dipole magnet, and provide some of the focusing properties of the spectrometer and to a large extent its acceptance. The front quadrupole, Q1, is convergent in the vertical plane and, the Q2 and Q3 are used for transverse focusing. The main specification of three quadrupole magnets is summarized in Table 3.5.

Table 3.5: The specification of HRS quadrupole magnet [56]

	Q1	Q2/Q3
Clear bore	300 mm	600 mm
Magnetic length	948 mm	1800 mm
Field gradient	8.31 T/m	3.5 T/m
Gradient uniformity (integral)	10^-3	10^-3
Maximum current	3250 A	1850 A

3.3.3 Target system

The experiment used the cryogenic gas targets which were loaded with the gas species: ^{3}H, ^{3}He, ^{2}H, ^{1}H and empty (see Fig. 3.6), and solid targets on bottom for calibration targets.

■ **Cryogenic gas target**

The cryogenic gas targets were cooled down by helium supply at 15 K and a controlled heater. The coolant flows through the pipe attached on the target ladder which is the heat sink made of copper, and enables to keep target at 40 K.

Each gas target has 25-cm length, and sealed by aluminum frames which are especially designed for safely handing with gaseous tritium in a range of beam current 0 to 22.5 μA. During beam time, density of gas varies uniquely because heat energy from beam energy loss is expected to make flow in the target. The effect is known depending on beam current and will be explained in Sec. 4.5.1. The cell thickness were measured for each cell at eight locations, and summarized in Table 3.7. The tritium gas was filled with 10 atmospheres and completely sealed at Safety

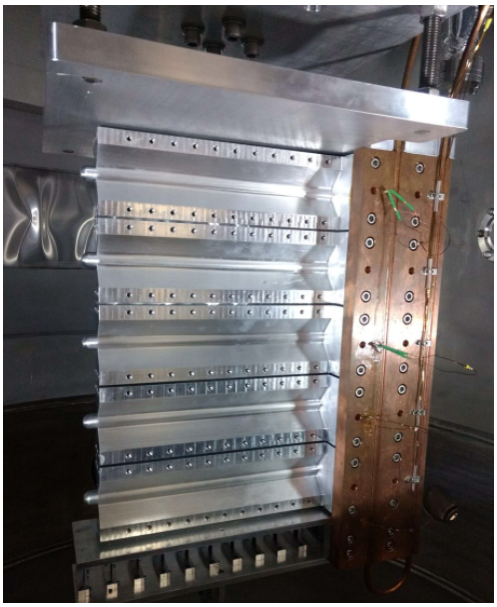

Figure 3.6: A photo of the target system into the vacuum chamber

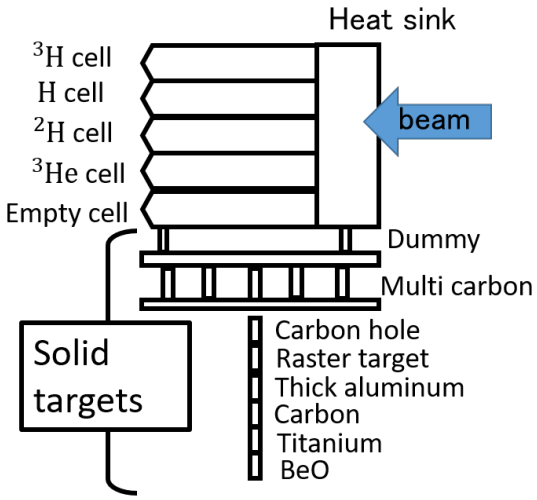

Figure 3.7: A schematics drawing of the target system.

Table 3.6: The main target specifications in this experiment [59]

State of target	Target	thickness [mg/cm^2]
Gas	^{3}H	84.8
	^{2}H	142.2
	^{1}H	70.8
	^{3}He	53.4
Solid	Multi carbon foils	883

and Tritium Applications Research Facility (STAR) at Idaho National Lab (INL) in order to ensure safety tritium operation.

■ **Solid targets**

Solid targets were located on the bottom of the gas target for taking calibration data (see Fig. 3.7). Dummy cell and multi carbon foils were mounted under the gas cells. The other solid targets were mounted on the target ladder. Fig. 3.8 shows multi carbon foils located under the gas target cells. 10 carbon foils with 2-mm length were mounted with spacing of 25 mm for z-vertex calibration. It is enough space among foils (25 mm) comparing with the typical z-vertex resolution ($\sigma \sim$ 4mm) to be separated from each of peak. Therefore, by comparing the reconstruct z-vertex distribution with reference z-vertex points, the reconstruct z-vertex was optimized by tuning the spectrometer parameters.

Table 3.7: Summary of the thickness of gas target cell.

Location	Empty cell thickness	^{3}H cell thickness	^{1}H cell thickness	^{2}H cell thickness	^{3}H cell thickness
Entrance (mm)	0.254± 0.005	0.253±0.004	0.311±0.001	0.215±0.004	0.203±0.007
Exit (mm)	0.279±0.005	0.343±0.047	0.330±0.063	0.294±0.056	0.328±0.041
Exit left (mm)	0.406±0.005	0.379±0.007	0.240±0.019	0.422±0.003	0.438±0.001
Exit right (mm)	0.421±0.005	0.406±0.004	0.519±0.009	0.361±0.013	0.385±0.016
Mid left (mm)	0.457±0.005	0.435±0.001	0.374±0.004	0.447±0.009	0.487±0.006
Mid right (mm)	0.432±0.005	0.447±0.004	0.503±0.005	0.471±0.012	0.478±0.007
Entrance left (mm)	0.508±0.005	0.473±0.003	0.456±0.010	0.442±0.005	0.504±0.011
Entrance right (mm)	0.424±0.005	0.425±0.003	0.457±0.006	0.332±0.011	0.477±0.011

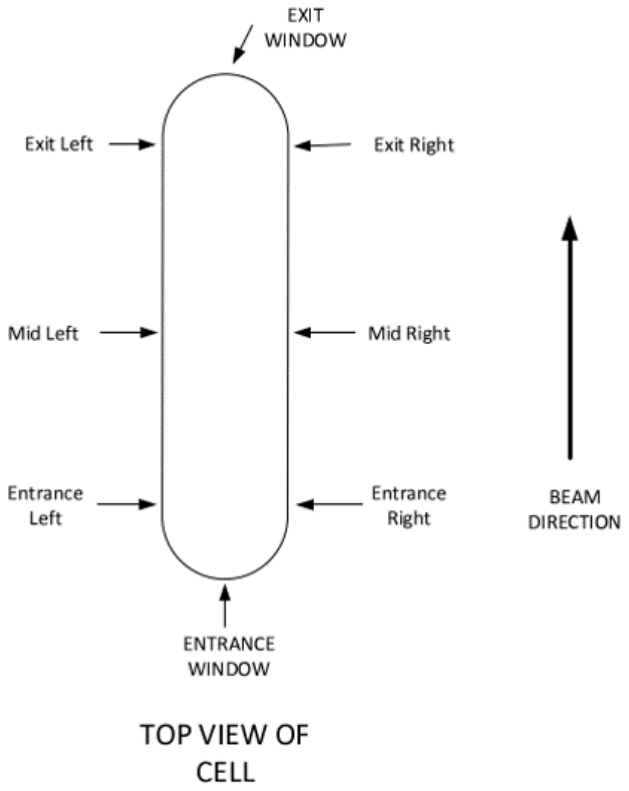

Table 3.8: A measurement points of the cells represented schematically

3.3.4 Sieve slit

Fig. 3.9 shows a design of sieve slit plate. It was made of tungsten with 2.54 cm thickness, and attached to an entrance of Q1 magnet. There are 154 holes with 4 mm diameters and 2 holes of 6 mm diameters. This plate has enough length to stop particles, so the only particles though holes enable to detect. This pate is used for optics calibration of HRS in off-line analysis (see Sec. 4.2.5).

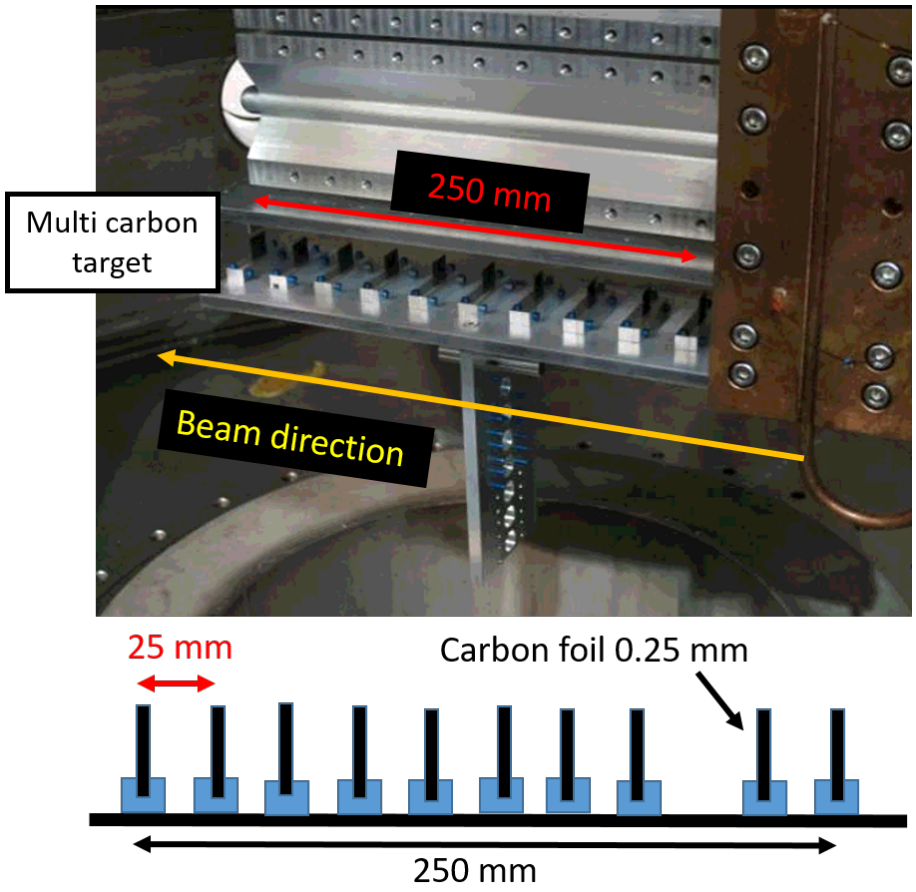

Figure 3.8: A picture of multi carbon foils

3.4 HRS detector package

The HRS detector package contains a Cherenkov detectors, two drift chambers (VDC1 and VDC2) and two types of trigger counters (S0 and S2), and it was used for the particle identification and measurement of particle path lengths. Figure 3.10 and 3.11 show detector packages in LHRS and RHRS, respectively. The momentum of the charged particle is reconstructed by an inverse transport matrix using information of positions and angles in the focal plane (see Sec. 4.2.2). Hence, two drift chambers (VDC1 and VDC2) installed in each HRS were used to measure the trajectory of charged particles and their positions in the focal plane. Two types of scintillation trigger counters (S0 and S2) installed at each HRS were used for an off-line analysis and a time-of-flight (TOF) measurement. In addition, two aerogel Cherenkov detectors (AC1 and AC2) were used to identify K^+ from the background such as p and π^+ detected in the RHRS. On the other hand, a gas Cherenkov detector (GC) was installed at LHRS to remove the π^- background. The main specification of each detector will be explained bellow.

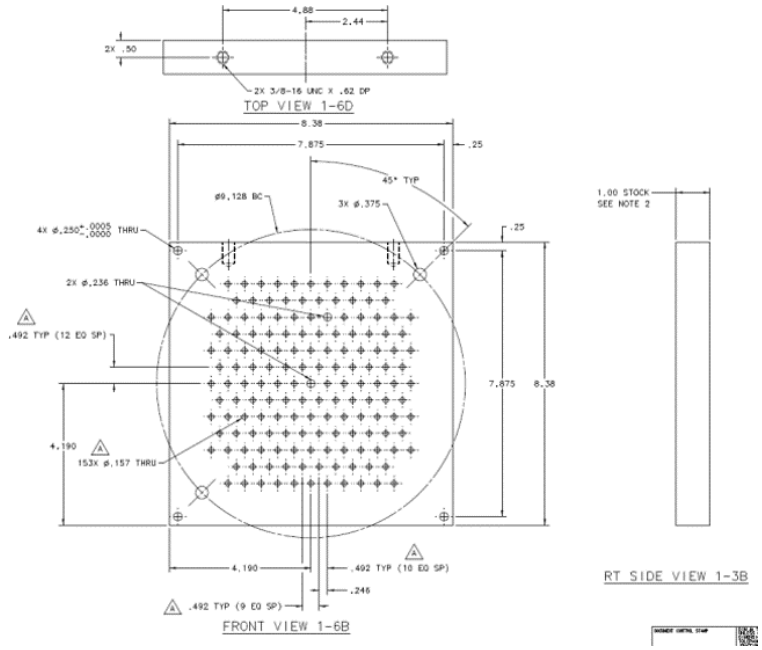

Figure 3.9: A schematic drawing of the HRS sieve slit plate with inch units. It was made of tungsten with 2.54 cm thickness, and attached on a front of Q1 magnet.

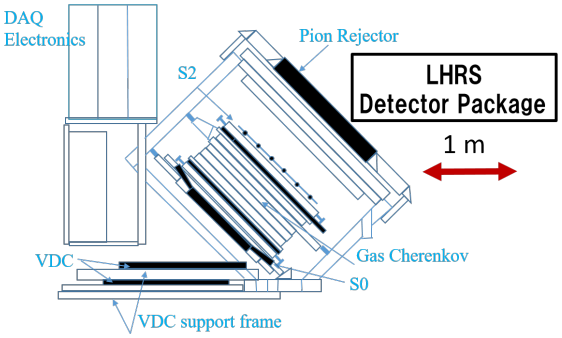

Figure 3.10: A schematic drawing of LHRS detector package. LHRS has two scintillation counters (S0, S2), two drift chambers (VDC1,2), gas Cherenkov detector and π^- rejector.

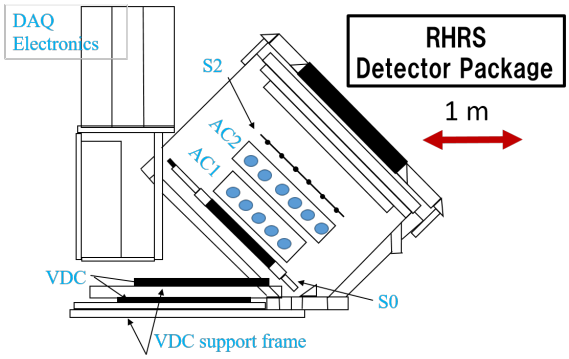

Figure 3.11: A schematic drawing of RHRS detector package. RHRS has two scintillation counters (S0, S2), two drift chambers (VDC1,2), and two aeroel Cherenkov detector (AC1, AC2).

3.4.1 Vertical drift chamber (VDC1,2)

Positions and incident angles of charged particles at focal plane were measured by using two drift chambers (VDC1 and VDC2). The VDCs, which are covered by aluminum frames, consist of two wire planes (U, V) with 368 sense wires on each plane. An active size of the VDC is 2188 mm × 288 mm, and the vertical distance between VDCs is 335 mm. Basically, a drift chamber use guide wires to make the electric field in the drift region more uniform. However, the VDC installed in HRS is not used these wires. The VDC are designed with a sensitive wires sandwiched between single-sided HV planes perpendicular to the direction of particle motion in

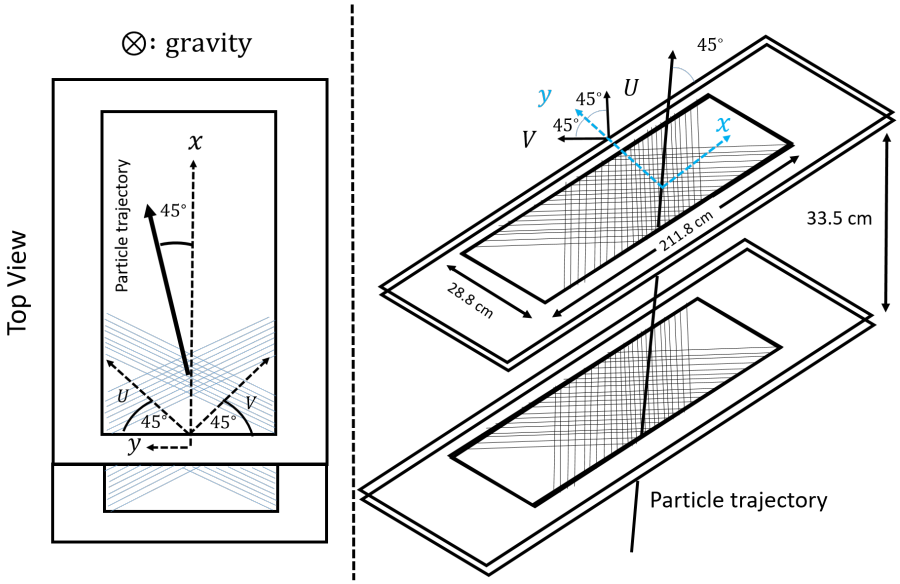

Figure 3.12: VDC layout

order to generate a uniform electric field in the drift region. Figure 3.13 shows a cross point of wire plane in the sense region. The VDC was designed to hit three cells when the particles passed wire plane at 45° of trajectory angle. Therefore, the pre-track efficiency of VDCs are close to 100% (Sec. 4.5.4).

■ **Time resolution of VDCs**

The VDCs is designed to hit multi wires per one track (see Fig. 3.13). In case of 5-wires hits, a relative time of the VDC per plane is obtained with the combination of drift times for each wire as follows:

$$\Delta T = |(t_1 - t_2) - (t_5 - t_4)|. \tag{3.1}$$

The required ΔT resolution was 20 ns (FWHM), and time resolution of per plane (Δt) is given by

$$\Delta t = \frac{1}{\sqrt{5}} \left(\frac{20 \text{ ns}}{\sqrt{4}} \right) = 4.5 \text{ ns}. \tag{3.2}$$

This value is corresponding with the position resolution of 225 μm (FWHM) per plane. For $E_{beam} = 0.845$ GeV and $\theta_{e'} = 16°$, the out-of-pane angle θ and in-plane angle ϕ at the target, are 6 mrad and 2.3 mrad, respectively [60]. By using these VDCs, it is possible to measure momentum with a resolution of ($\Delta p/p \sim 2.5 \times 10^{-4}$).

3.4.2 Scintillation trigger counter (STC)

There were two types of scintillation trigger planes (S0 and S2) in each HRS, which were used for timing measurement of charged particles and off-line trigger counters. S0 and S2 are arranged

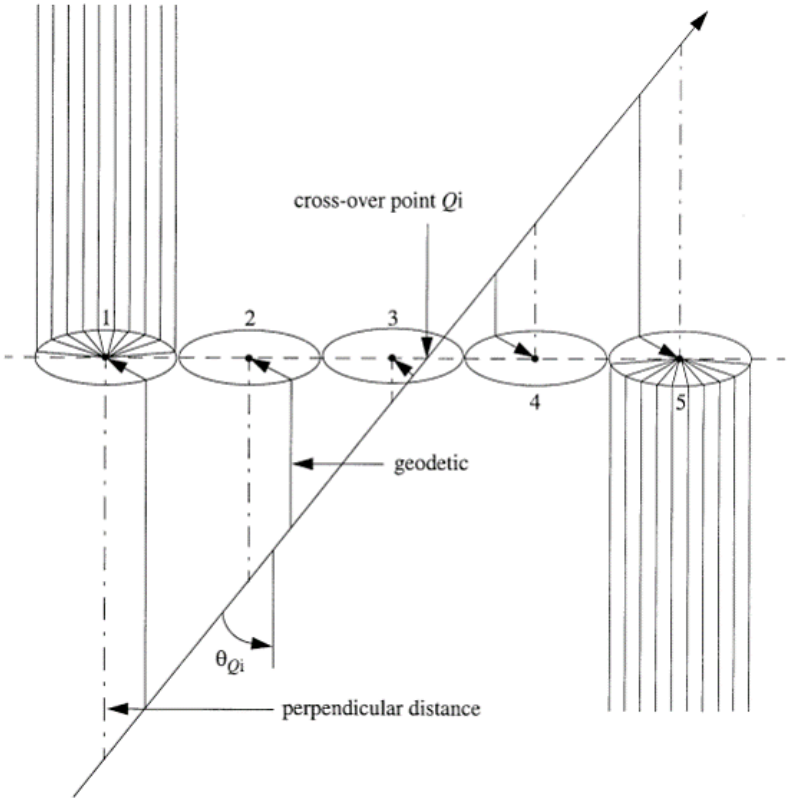

Figure 3.13: A track resulting in a 5-cell hits. The arrowed lines show paths of least time for ionization electrons to travel. The dot-dashed lines mean projection distances. The ellipse area near the wires shows electronic filed lines.

along the momentum dispersion (detector-x) direction.

■ **S0 trigger counter**

The 10 mm thick S0 counter, which is made of BICRON 408 plastic scintillator with an active area of 1700 mm × 250 mm, is attached to two 3" PMTs (XP2312). The timing resolution was $\sigma_t \sim 0.2$ ns.

■ **S2 trigger counter**

The S2 detector, located behind S0, was used for a timing counter and an off-line trigger counter. It composes of 16 segments of S2 trigger counters mounted on a steel frame (Fig. 3.14). Each scintillation bar is made of plastic scintillator (EJ-230), which has an active area of 432 mm × 140 mm and 50 mm thick. Time resolution (σ_T) in the S2 plane is about 0.3 ns, and the time resolution of TOF from target to S2 plane is 0.5 ns (σ).

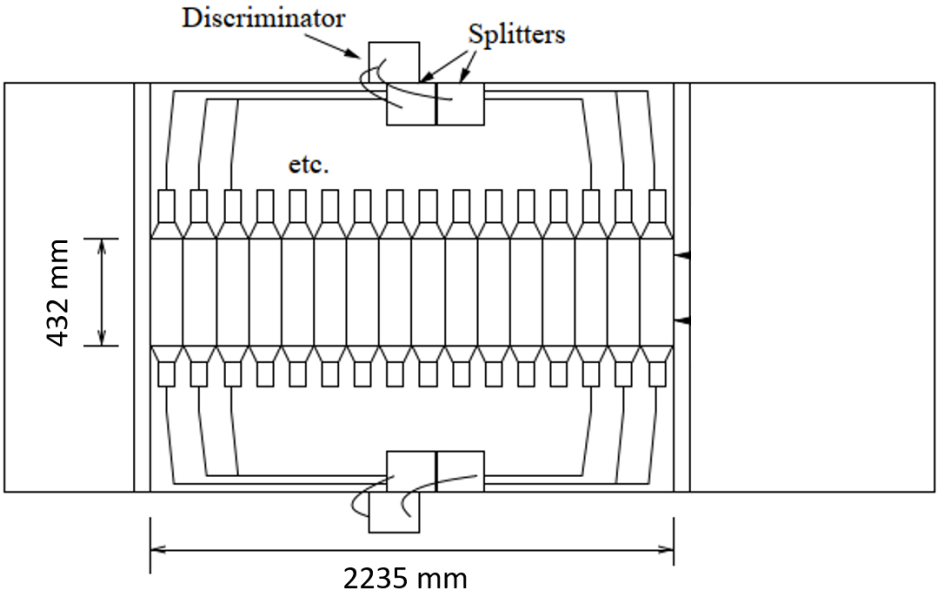

Figure 3.14: The layout on frame with S2 paddles [54]. There are sixteen S2 paddles on the frame. The size of one S2 scintillation trigger counter is 432 mm × 140 mm in active area and 50 mm in thickness, and total effective are of the S2 detector is 2235 mm × 432 mm.

3.4.3 Cherenkov detecoters

The experiment was detected K^+ at RHRS and e' at LHRS for identification of Λ productions. However, much background were detected in each HRS. Basically, the charged particle is identified using Cherenkov detectors. When the charged particle passes through a material with a refractive index of n with higher than the speed of light in a material ($\beta > 1/n$), it emits Cherenkov light. Cherenkov photon yield in material with a refractive index of n is written as followings:

$$\frac{d^2N}{dxd\lambda} = \frac{2\pi\alpha z^2}{\lambda^2}\left(1 - \frac{1}{\beta^2 n^2(\lambda)}\right), \tag{3.3}$$

α : Fine structure constant,
N : Number of photons,
x : Path length [m],
λ : Wavelength of the Cherenkov light [m],
z : Charge of the particle,
β : Velocity factor of the particle,
$n(\lambda)$: Refraction index of the medium.

In order to identify the charged particle such as e' and K^+, this experiment used two aerogel Cherenkov detectors (AC1 and AC2) in RHRS, and a gas Cherekov detector in LHRS. The performance of these Cherenkov detectors will be discussed in detail below.

Table 3.9: Main characteristics of Cherenkov detectors

Arm	Detector	material type	Refractive index	Tile size (cm^3)	Radiator Size (cm^3)	Number of PMTs	PMT Model
RHRS	AC1	Aerogel (SP15)	1.015	$10 \times 10 \times 1$	$170 \times 32 \times 9$	24	RCA 8854
	AC2	Aerogel (SP50)	1.055	$10 \times 10 \times 1$	$192 \times 30 \times 5$	26	XP 4572B
LHRS	GC	CO_2	1.00041	-	$250 \times 80 \times 150$	10	BURLE 8854

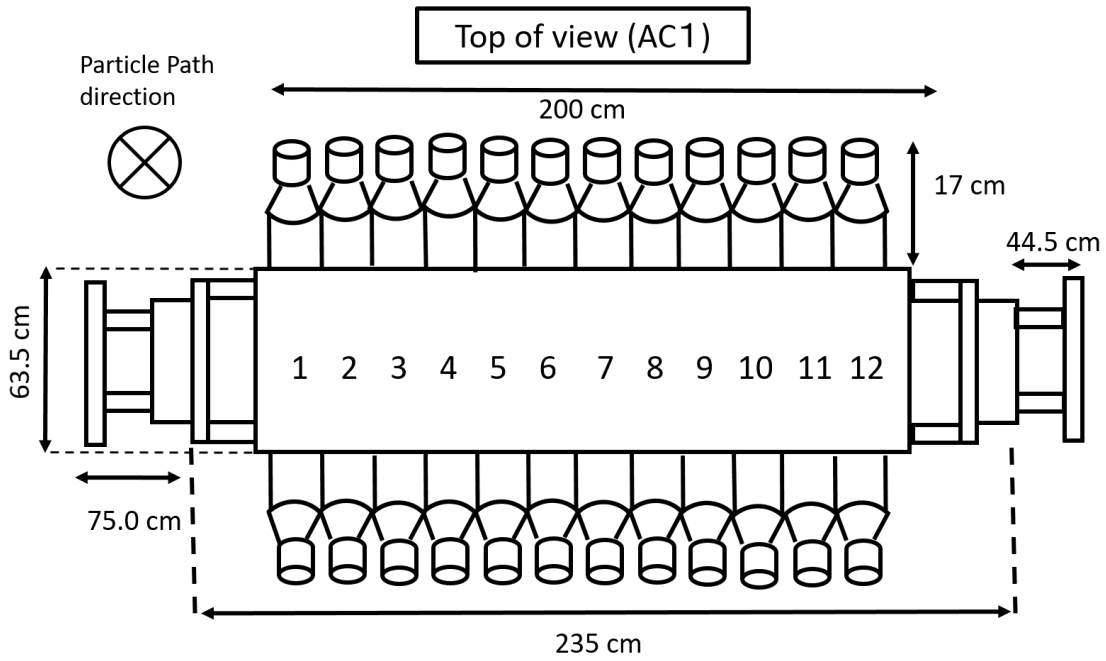

Figure 3.15: A schematics drawing of aerogel Cherenkov detector (AC1). There are 12 segments and 24 PMTs.

■ **Aerogel Cherenkov detector : AC1**

The main specifications of used Cherenkov detectors are summarized in Tab. 3.9.

The AC1 detector was used for distinguished π^+ from K^+ and p in off-line analysis. Figure 3.15 shows a schematics drawing of the AC1. The AC1 contains aerogel tiles with refractive indices at 1.015 (SP15) and a thickness of 9 cm, and there are 24 segments with PMTs (RCA 8854). In addition, the millipore and the ESR seats were attached to the inside of the AC light box as reflections.

■ **Aerogel Cherenkov detector : AC2**

The AC2 was used for K^+ separation from π^+ background. Figure 3.16 shows a schematics drawing of the AC2. The AC2 has an aerogel with refractive index of 1.055 and 5 cm thickness. There are 26 segments with PMTs (XP 4572B).

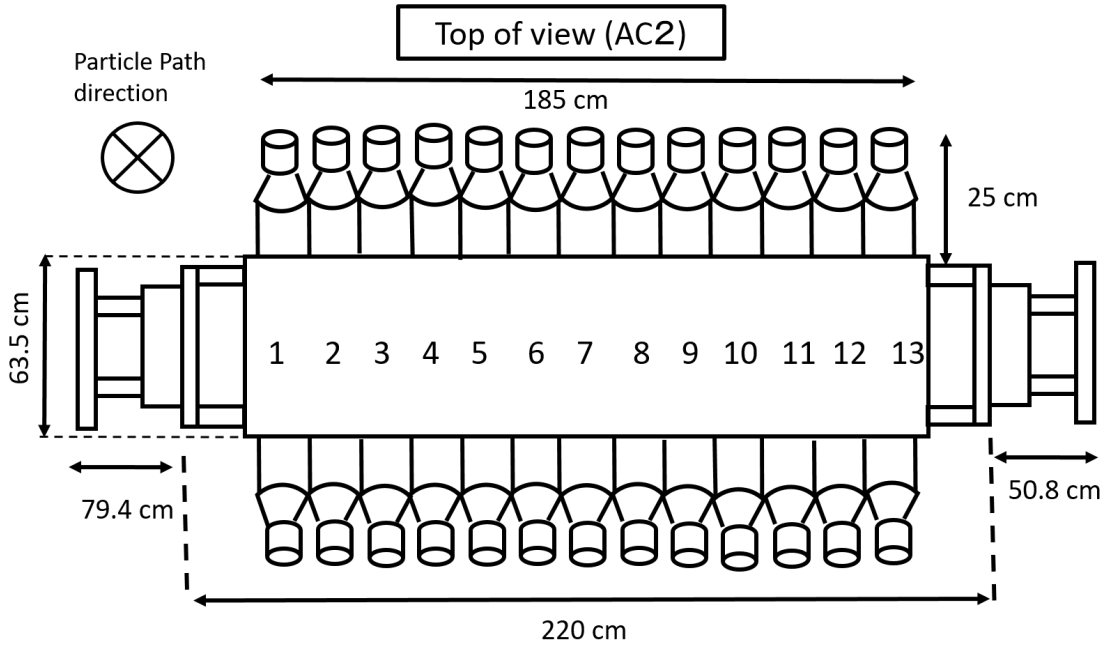

Figure 3.16: A schematics drawing of aerogel Cherenkov detector (AC2) front view of AC2. There are 13 segments and 26 PMTs.

■ **Gas Cherenkov detector (GC)**

The gas Cherenkov (GC) detector is filled with CO_2 gas with reflective index of 1.00041, at 1 atmosphere. It was used for electron identification, and mounted between S0 and S2. The momentum thresholds for an electron and a π in the GC are 0.017 and 4.8 GeV/c, respectively. Therefore, when charged particles below 4.8 GeV/c pass through the GC, the GC detects only Cherenkov light of emitting by electrons. The geometrical layout of the GC is shown in Fig. 3.17. The emitting Cherenkov light was reflected on 10 concave mirrors in the bottom of chamber, and it guided by ten spherical mirrors to PMTs with 11-cm diameters (BURLE 8854).

■ **Particle identification**

The two aerogel Cherenkov detectors, the refractive indexes of which are 1.015 and 1.055, were used to identify K^+ in off-line analysis in RHRS. The Fig. 3.18 and 3.19 show the result of the number of photon electron with Eq. 3.3. The wavelength was integrated between 300 to 650 nm which is typical sensitive range of wavelength of the PMT, and reflective index ($n(\lambda)$) was fixed at 1.015 and 1.055 for two aerogel (AC1, AC2), respectively. In this experiment, the acceptance range of K^+ momentum was from 1.72 to 1.88 GeV/c. The AC1 separates π^+ from p and K^+, and AC2 distinguishes K^+ from p in the acceptance range. K^+ events can be distinguished with

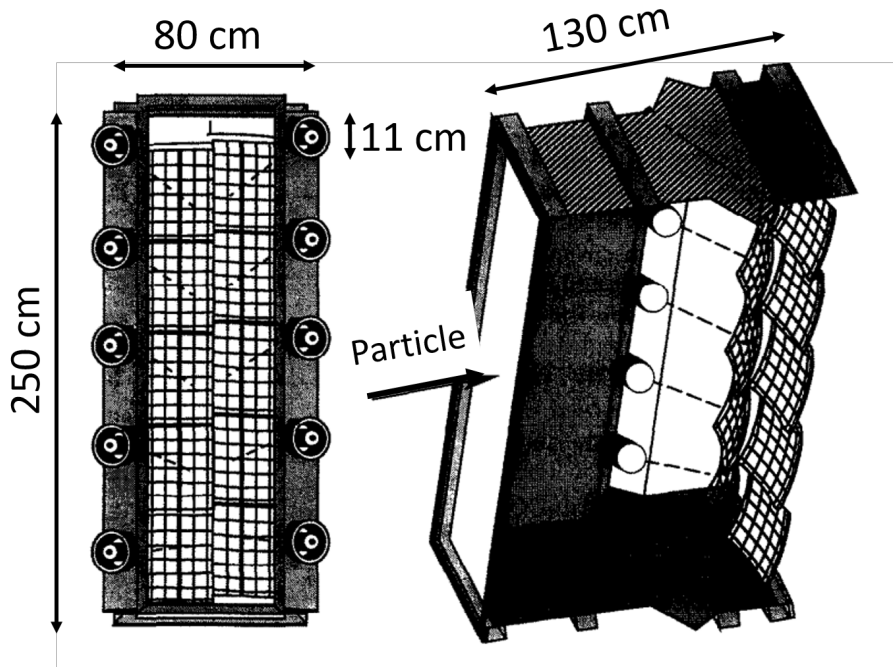

Figure 3.17: A schematics of gas Cherenkov detector [61].

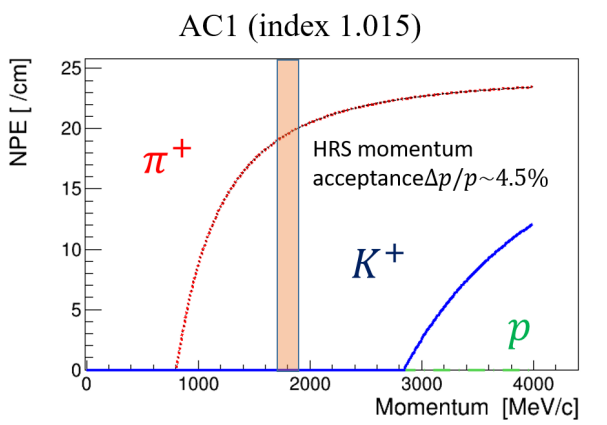

Figure 3.18: This shows the π^+, K^+ and p momenta dependence of Cherenkov photon yields with aerogel of $n = 1.015$ per 1 cm thickness. The π^+ can be distinguished from p and K^+ within a range of RHRS acceptance in the off-line analysis.

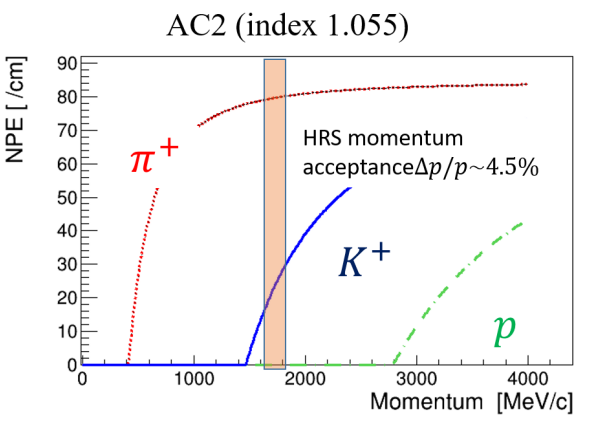

Figure 3.19: This shows the π^+, K^+ and p momenta dependence of Cherenkov photon yields with aerogel of $n = 1.055$ per 1 cm thickness. The p can be distinguished from π^+ and K^+ within a range of RHRS acceptance in off-line analysis. Applying an appropriate ADC threshold cut, the K^+ particles can be separated from π^+.

the combination of AC1 and AC2, as follows :

$$\overline{AC1} \otimes AC2. \tag{3.4}$$

In the case of LHRS, the gas Cherekov detector with the refractive indexes of 1.00041 was used for π^- rejection. Fig.3.20 shows the result of the number of photon electron with Eq. 3.3. The wavelength was integrated between 300 to 650 nm which is typical sensitive range of wavelength

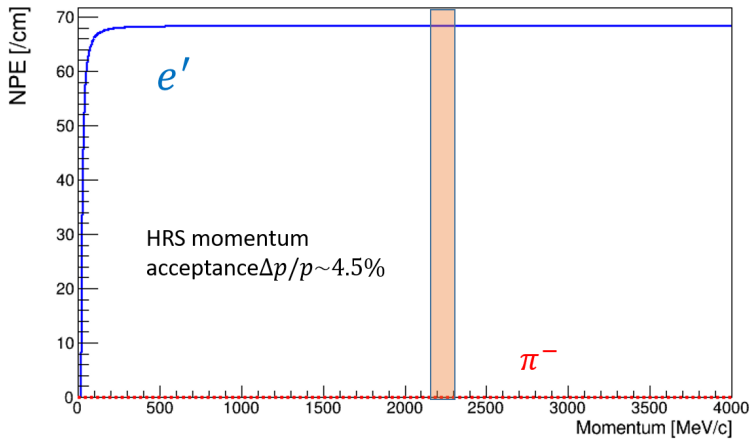

Figure 3.20: Number of photo-electrons (NPEs) with Gas Cherenkov as a function of momenta of e' and π^-.

of the PMT, and reflective index ($n(\lambda)$) was fixed at 1.0041. Within a range of LHRS acceptance, π^- are not detected by GC. Hence, e' events can be distinguished by selecting fired events in GC.

3.5 Trigger systems

In the experiment, there are five trigger modes, T_{L1}, T_{L2}, T_{L3}, T_R and T_{coin}. T_{L1}, T_{L2} and T_{L3} are LHRS single triggers which consist of S0, S2 and gas Cherenkov triggers in LHRS. The LHRS triggers will be also explained in Sec. 3.5.1. The RHRS trigger (T_R) consists of coincidence of S0 and S2 triggers. These four triggers, which were generated to analyzed the single arm data, were used for taking calibration data. In the $(e, e'K^+)$ experiment, the coincidence trigger (T_{coin}), which consists of coincidence of T_{L1} and T_R triggers, is mainly used for $e'K^+$ coincidence data analysis, and described logical condition as the follow:

$$T_{coin} = T_R \otimes T_{L1}. \tag{3.5}$$

These multi trigger signals (Fig. 3.21) were controlled with Trigger Supervisor(TS), which is the designed at CEBAF [62]. Taking data by these triggers were pre-scaled by TS, and was controlled to keep high efficiency of data acquisition (DAQ).

3.5.1 LHRS trigger system

As a LHRS single trigger, the experiment was used three triggers (T_{L1}, T_{L2}, T_{L3}). These trigger's logical condition are shown in Fig. 3.22 and described as:

$$T_{L1} = (LS0 \otimes LS2), \tag{3.6}$$
$$T_{L2} = (LS0 \otimes LS2) \otimes GC, \tag{3.7}$$
$$T_{L3} = (LS0 \oplus LS2) \otimes GC. \tag{3.8}$$

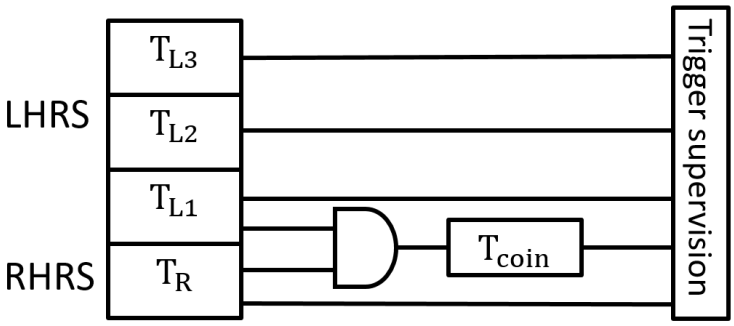

Figure 3.21: Main triggers of E12-17-003 experiment. The single triggers (T_{L1}, T_{L2}, T_{L3}, T_R) and coincidence trigger (T_{coin}) signals were controlled by the trigger supervisor.

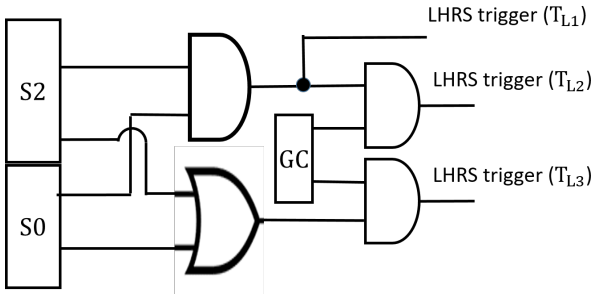

Figure 3.22: LHRS trigger conditions

Data with T_{L1} trigger was took when S0 and S2 were fired simultaneously. The other LHRS triggers (T_{L2} and T_{L3}) were generated with the combination of S0, S2 and gas Cherenkov detector triggers. The rate of main LHRS single trigger (T_{L1}) was $\sim$ 11.5 kHz (pre-scaled 1/200 in TS) with beam current 25 μA with tritium target (thickness is 84.8 g/cm^2).

3.5.2 RHRS trigger system

RHRS trigger was made by the following logical condition:

$$T_R = (RS0 \otimes RS2). \tag{3.9}$$

The RHRS trigger (T_R) was also generated with the combination of S0 and S2 in RHRS. RHRS trigger rate was 20 kHz (pre-scaled 1/200 in TS) with beam current 25 μA with tritium target (thickness is 84.8 g/cm^2).

3.5.3 Data acquisition

In the experiment, data were taken by the CEBAF On-line Data Acquisition (CODA) system [63]. The CODA data acquisition system was developed for rapid construction of DAQ systems, and consists of three components which are the readout controller (ROC), the event builder (EB) and the event recorder (ER). Additionally, TS and the event transfer (ET) system, which

Table 3.10: Data summary of the E12-17-003 experiment.

Target	Kinematics	Thickness [mg/cm^2]	Beam current [μA]	Total charge [C]
H	H kine	70.8	22.5	4.7
H	T kine	70.8	22.5	1.3
^{3}H	T kine	84.8	22.5	14

is used instead of data distribution system (DD), were implemented.

Chapter 4 Analysis

4.1 Particle identification

In the $(e, e'K^+)$ reaction experiment, e' and K^+ were observed to identify the Λ productions. However, much background such as π^-, π^+ and p, contaminated in the spectrometers (HRSs). These backgrounds were identified by an off-line analysis using the Cherenkov detectors (AC1, AC2) and the time of flight (TOF) information from the target to the trigger scintillation counter (S2).

4.1.1 Coincidence time

The accidental electrons (e') in the LHRS cannot be removed by any Cherenkov detectors. Therefore, the coincidence time analysis was used to remove the accidental electrons.

The coincidence time ($T_{\rm coin}$) was defined as a reaction time difference between the K^+ and scattered electrons,

$$T_{\rm coin} = T_{\rm L} - T_{\rm R}. \tag{4.1}$$

Reaction times at the target ($T_{\rm L},\ T_{\rm R}$) were determined by subtracting the TOF from detection time at the S2 counters ($T_{\rm S2}$) as following,

$$T_{\rm R} = T_{\rm RS2} - \frac{l_{\rm path}}{c\beta_{\rm R}}, \tag{4.2}$$

where $\beta_{\rm R}$ and $l_{\rm path}$ were the velocity of particles and the path lengths from the vertex point to the S2 trigger position in RHRS. The $T_{\rm L}$ was also written in Eq. 4.2 with variables of $\beta_{\rm L}$ and $l_{\rm path}$. Reaction times of K^+ and e' at target should be same so e' is separable from accidental electrons by selecting $T_{coin} \sim 0$ which means simultaneous production of e' and K^+. Additionally, π^+ and p background events were also identified with coincidence time analysis. The velocity (β) was calculated with momentum (p) which was reconstruct by backward matrices (Sec. 4.2.2). Therefore, Eq. 4.2 was described with momentum and particle mass (m) as:

$$T_{R,L} = T_{RS2,LS2} - \frac{l_{path}}{c}\frac{p}{\sqrt{p^2+m^2}}. \tag{4.3}$$

Since coincidence time was depending on particle masses, the $e'\pi^+$ and $e'p$ coincidence times were 3 and 7 ns difference from $e'K^+$ coincidence time (see Table 4.1). Fig. 4.1 shows the coincidence time distribution. The events around $T_{coin} \sim 0$ ns corresponding to $e'K^+$ events,

Table 4.1: Time of flight for each particle

Particles	β at 1.8 GeV/c	flight time (l_{path} = 27.3 m)
K^+	0.964	94.4 ns
π^+	0.997	91.2 ns
p	0.887	102.6 ns

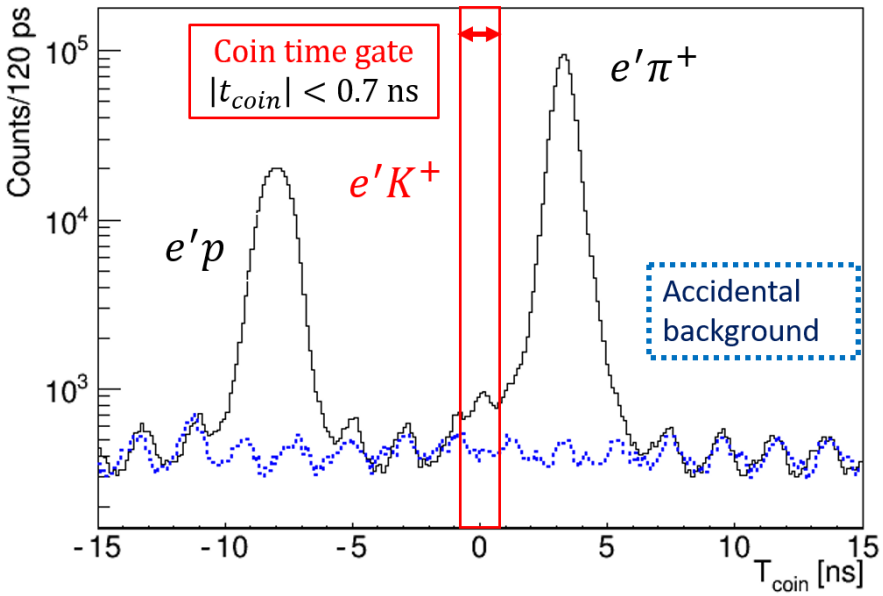

Figure 4.1: [
Coincidence time distribution without any Cherenkov cut.]Coincidence time distribution without any Cherenkov cut. The K^+ events existed at $T_{\rm coin} = 0$ ns. In this analysis, $-0.7 \leq T_{\rm coin} \leq 0.7$ ns region was used for K^+ events selection.

and main two peaks around -8.0 ns and 3.5 ns were $e'p$ and $e'\pi^+$ coincidence events, respectively. The 2-ns bunch structures originated from RCS (499 MHz). The number of $e'K^+$ coincidence events was obtained by subtracting the accidental background distribution which was estimated from selecting side bunches of coincidence time ($|T_{\rm coin}| > 20$ ns). Coincidence events in a range of $|T_{coin}| < 0.7$ region were selected as a $e'K^+$ coincidence events.

4.1.2 Electron identification

Negative charged particles such as π^- and accidental electrons contaminated in the LHRS. The gas Cherenkov detector (GC), which was filled with CO_2 gas with refractive index of 1.00041, was used for a selection of scattered electrons in the off-line analysis. Figure 4.2 shows ADC distribution of the GC. The one of the peak at 500 ch was one photon electron and pedestal events were removed with ADC cut. off-line cut of GC was applied to

$$\mathrm{ADC_{GC}} \geq 1800 \text{ ch} \tag{4.4}$$

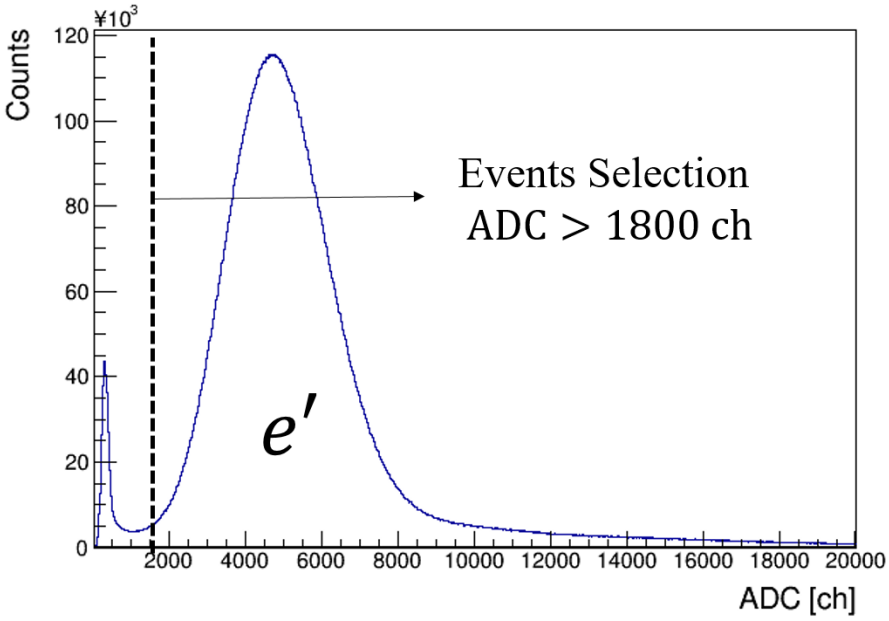

Figure 4.2: Gas Cherenkov cut condition

4.1.3 K^+ identification

Off-line K^+ identification (KID) is necessary to remove a large background from mainly π^+ and p particles. For the K^+ identification, two aerogel Cherenkov detectors (AC1, AC2) were installed in the RHRS detector package. Figure 4.3 and 4.4 show the detected number of photo-electrons of AC1 and AC2 depending on coincidence time. For the K^+ identification, the cut conditions of AC1 and AC2 were determined as follows:

$$\text{AC1} \leq 3.0 \text{ [NPE]} , \tag{4.5}$$

$$1.0 \text{ [NPE]} \leq \text{AC2} \leq 23.0 \text{ [NPE]} . \tag{4.6}$$

4.2 Optics calibration

4.2.1 Missing mass

In the $(e, e'K^+)$ reaction, the missing mass of the Λ hypernucei was calculated from :

$$M_{HYP} = \left[(E_e + M_{tar} - E_K - E_{e'})^2 - (\vec{p}_e - \vec{p}_K - \vec{p}_{e'})^2\right]^{1/2} , \tag{4.7}$$

$$= \left[(\cdots)^2 + p_e^2 + p_{e'}^2 + p_K^2 - 2p_e p_{e'}\cos\theta_{ee'} - 2p_e p_K \cos\theta_{eK} + 2p_{e'} p_K \cos\theta_{e'K}\right] , \tag{4.8}$$

where E_e and $\vec{p}_e$ are beam energy and momentum, and M_{tar} is target mass. The $\theta_{ee'}$, θ_{eK} and $\theta_{ee'}$ are particle angels at target. The beam momentum vector were precisely controlled in CEBAF (see Table 3.1), and beam energy E_e was calculated from an equation of $E_e = \sqrt{M_e^2 + |\vec{p}_{e'}|^2}$. Therefore, the missing mass can be deduced from the information of momentum vectors about

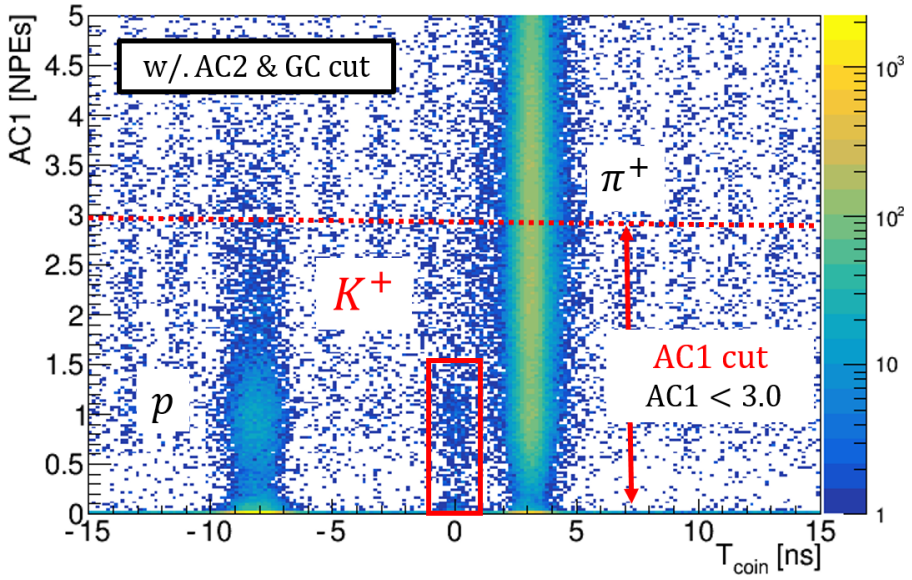

Figure 4.3: Correlation between coincidence time and AC1 NPEs. The Chereknov cut of GC (Eq. 4.4) and AC2 (Eq. 4.6) were used.

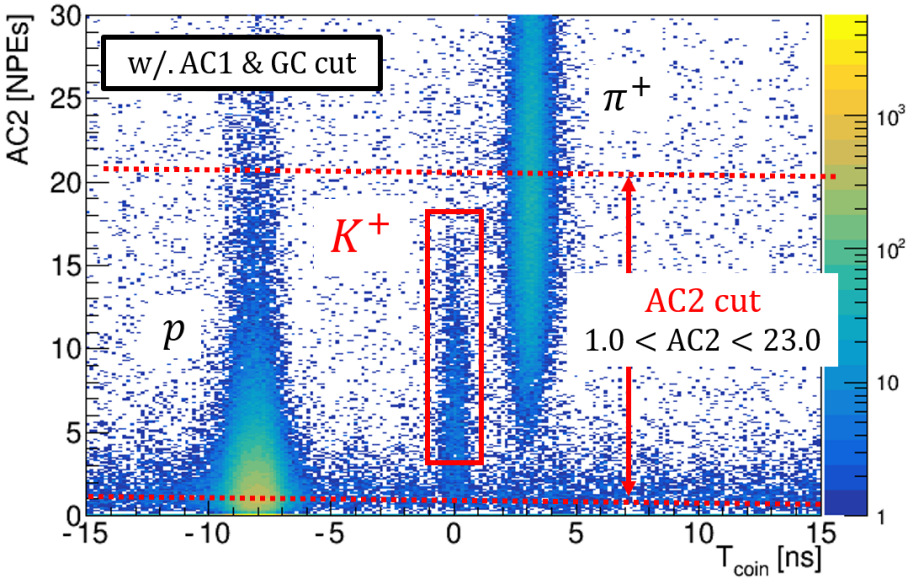

Figure 4.4: Correlation between coincidence time and AC2 NPEs. The Chereknov cut of GC (Eq. 4.4) and AC1 (Eq. 4.5) were used.

K^+ and scattered electron at target. The angles and momentum at target were obtained by using the backward transfer matrix from focal plane (x_{FP}, y_{FP}, x'_{FP}, y'_{FP}). Therefore, the optimization of backward transfer matrix improved the missing mass resolution.

4.2.2 Backward matrix

The reference plane (subscript RP) events at target (subscript tar) is transferred to with a 1st order matrix (M_0), is described as:

$$\begin{pmatrix} x_{RP} \\ x'_{RP} \\ y_{RP} \\ y'_{RP} \\ p \end{pmatrix} = M_0 \begin{pmatrix} x_{\rm tar} \\ x'_{\rm tar} \\ y_{\rm tar} \\ y'_{\rm tar} \\ p \end{pmatrix} \tag{4.9}$$

where $x,\ y,\ x'(\equiv p_x/p_z),\ y'(\equiv p_y/p_z)$ and p are positions (x, y), angles (x', y') and momentum (p) of particles. Experimentally, the particles were detected at the reference plane, so the target plane information is estimated with an inverse transfer matrix (M_0^{-1}) by :

$$\begin{pmatrix} x_{\rm tar} \\ x'_{\rm tar} \\ y_{\rm tar} \\ y'_{\rm tar} \\ p \end{pmatrix} = M_0^{-1} \begin{pmatrix} x_{RP} \\ x'_{RP} \\ y_{RP} \\ y'_{RP} \\ p \end{pmatrix} . \tag{4.10}$$

This is a ideal case. In reality, the magnetic field of HRS cannot be reproduced by first order matrix. Therefore, the inverse matrix needs high order terms as:

$$\begin{pmatrix} x_{\rm tar} \\ x'_{\rm tar} \\ y_{\rm tar} \\ y'_{\rm tar} \\ p \end{pmatrix} = M \begin{pmatrix} x_{RP} \\ x'_{RP} \\ y_{RP} \\ y'_{RP} \\ x^2_{RP} \\ z_{\rm tar} \\ x_{\rm RP}x'_{\rm RP} \\ \vdots \end{pmatrix} \tag{4.11}$$

$$z_{\rm tar} = M_Z \begin{pmatrix} x_{RP} \\ x'_{RP} \\ y_{RP} \\ y'_{RP} \\ x^2_{\rm RP} \\ x_{RP}x'_{RP} \\ \vdots \end{pmatrix} \tag{4.12}$$

where $z_{\rm tar}$ is z-vertex (a beam direction) which can be written with Eq. 4.12. There is no momentum term (p) in the Eq. 4.11. Experimentally, the momentum cannot be measured directly at the reference plane, so the momentum parameter at target was written with parameters of the reference plane. The variable of angles $(x'_{\rm tar}, y'_{\rm tar})$, momentum (p) and z-vertex $(z_{\rm tar})$ were written as follows:

$$z_{\rm tar} = \sum_{i+j+k+l\le n} C_z(i,j,k,l)(x_{RP})^i(x'_{RP})^j(y_{RP})^k(y'_{RP})^l, \tag{4.13}$$

$$x'_{\rm tar} = \sum_{i+j+k+l+m\le n} C_{x'}(i,j,k,l,m)(x_{RP})^i(x'_{RP})^j(y_{RP})^k(y'_{RP})^l(z_{\rm tar})^m\ , \tag{4.14}$$

$$y'_{\rm tar} = \sum_{i+j+k+l+m\le n} C_{y'}(i,j,k,l,m)(x_{RP})^i(x'_{RP})^j(y_{RP})^k(y'_{RP})^l(z_{\rm tar})^m\ , \tag{4.15}$$

$$p = \sum_{i+j+k+l+m\le n} C_p(i,j,k,l,m)(x_{RP})^i(x'_{RP})^j(y_{RP})^k(y'_{RP})^l(z_{\rm tar})^m\ , \tag{4.16}$$

Table 4.2: Number of parameters required each matrix order

order (n)	1	2	3	4	5	6
${x'}_T$, ${y'}_T$	6	21	56	126	252	462
z_T	5	15	35	70	126	210

where $C_{x',y',z}(i,j,k,l,m)$ were components of M in Eq. 4.11 and 4.12. The numbers of parameters written in Eq. 4.13, 4.14, 4.15 and 4.16 are summarized in Tab. 4.2. Each co-efficient variable of $C_{z,x',y',p}$ in ${x'}_{\rm tar}$, ${y'}_{\rm tar}$, $z_{\rm tar}$ and p was optimized by a minimization of chi square with each calibration data.

4.2.3 Raster correction

The beam raster with 1.8×2.9 mm^2 was used for the cryogenic to reduce an energy loss density. In the Hall A, x and y coordinate were defined as a gravity and vertical directions, respectively. Figure 4.5 shows the geometrical correlation between the raster position y and reconstruct z-vertex.

When the Λ was produced at (y,z)=$(\Delta y, z_{\rm Hit})$, reconstructed z-vertex point ($z_{\rm Rec}$) was given at the intersection point of particle tracking and x-axis. Therefore, the reconstructed z-vertex point has offset derived from raster y ($\Delta z_{\rm ras} = z_{Hit} - z_{\rm Rec}$). This offset was geometrically calculated as :

$$z_{ras} = \frac{y_{ras}}{\tan(\theta_{\rm HRS} + y'_{tar})}, \tag{4.17}$$

where $\theta_{\rm HRS}$ and y'_{tar} are HRS located at an angle of 13.2° and angle from the central axis of the HRS. Figure 4.6 shows the distributions of z-vertex, the reconstructed z-vertex (blue line) and corrected z-vertex (red line). Comparing these distributions with the reference positions of multi-carbon foils (dot line in Fig. 4.6), the the z-distribution after the raster correction was better agreement with the reference positions than before the correction.

4.2.4 z-vertex correction

While the past Λ hypernuclear experiments used thin targets of $\leq$ 1 mm, the experiment used gas long (25 cm) gas targets. An energy resolution was worse for long targets because the generation positions were dispersed. Therefore, in this experiment, the multi-foil target was used to correct for the target thickness. Figure 4.7 shows the target thickness (z-vertex) distribution when the multi-carbon foils target was used. The co-efficient variable of C_z in Eq. 4.13 was optimized with a chi square minimization by comparing with known positions of multi-carbon

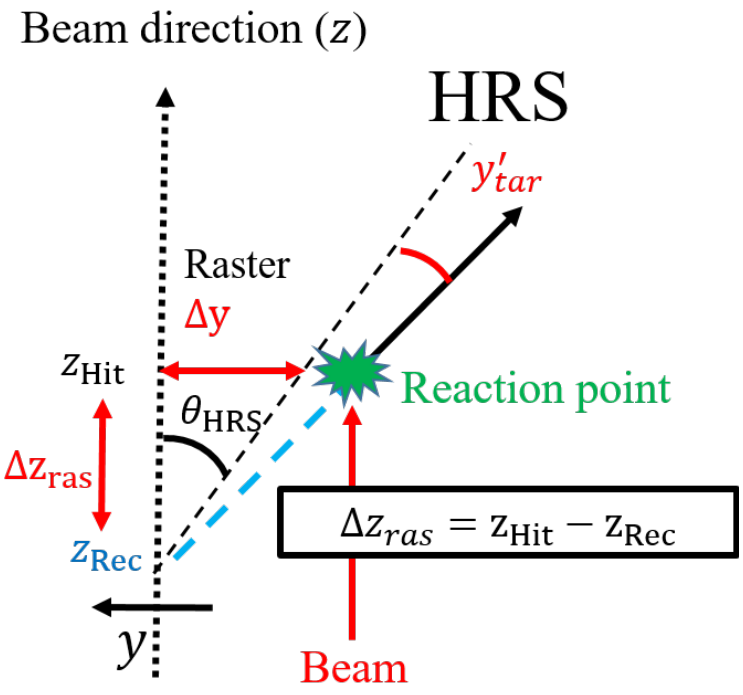

Figure 4.5: A schematics drawing of raster correction

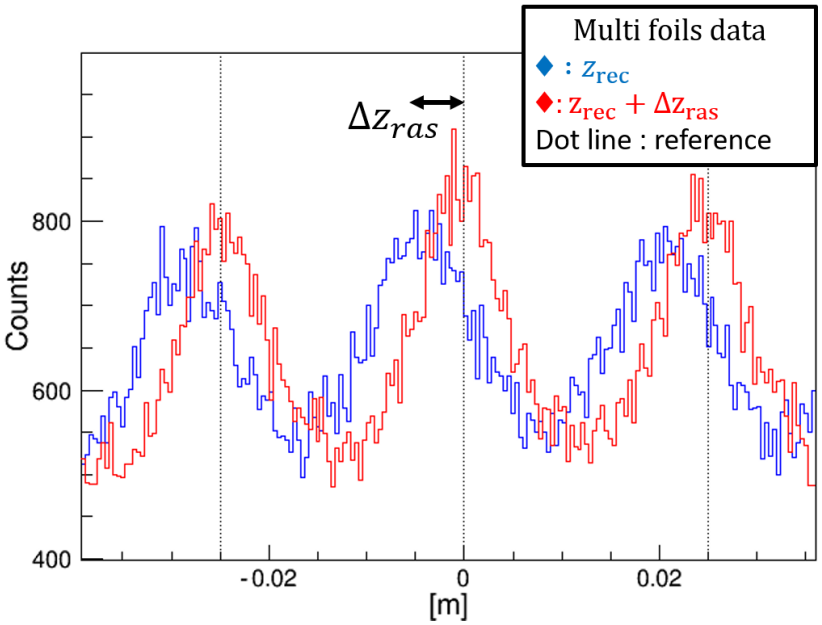

Figure 4.6: z-vertex distributions without (blue line) and with raster calibration (red line)

foils. The chi square (χ^2_z) in each carbon foil was defined as :

$$\chi^2_{z_j} = \sum_{i=0}^{N} \frac{(z_j^{\mathrm{ref}} - z_i)^2}{\sigma^2_{z_j}} \tag{4.18}$$

where j is label of carbon foils ($j \leq 10$). The N_j was the number of events when selecting within 2.5 cm from the reference position (z^{ref}) of each carbon foil. The total chi-square of z-vertex

(χ^2_z) was represented by adding each chi-square ($\chi^2_{z_j}$) in Eq. 4.18 as :

$$\chi^2_z = \sum_{j=0}^{10} \chi^2_{z_j}. \tag{4.19}$$

Figure 4.7 and 4.8 are shown result of z-vertex calibration. The blue dashed and red lines show reconstructed the z-vertex in LHRS before and after the z correction. The black dashed lines show the positions of multi-foil target. The resolutions of foils which were gotten by fitting with Gaussian functions, are shown Fig. 4.8. The resolutions of all carbon foils in both HRS arm are given by fitting with Gaussian functions, and better resolution than NIM value ($\sigma_z < 7.8$ mm).

4.2.5 Angle calibration

The angles (x'_{tar}, y'_{tar}) at vertex were represented with the backward matrix with Eq. 4.14 and 4.15. The parameters of angles ($x'_{tar},\ y'_{tar}$) are optimized with sieve slit data. Sieve slit plate, which has 2.54-cm length with 153 holes of 4 mm diameters and 2 holes of 6 mm diameters, was attached to entrance of Q1 magnet in HRS. Therefore, the charged particles, which only passed through sieve slit holes, can be observed (Fig. 4.9).

The angles (X', Y') at vertex point enabled to be determined with sieve slit positions ($x_{SS},\ y_{SS}$) by :

$$y_{SS} = \frac{l'_0 Y'}{\cos(\theta_{\rm HRS} - \theta'_{\rm HRS} \mp \tan(Y'))} \quad \text{(LHRS, RHRS)}, \tag{4.20}$$

$$\theta'_{\rm HRS} = \tan^{-1}\left(\frac{l_0 \sin\theta_{\rm HRS}}{l_0 \cos\theta_{\rm HRS} - z}\right), \tag{4.21}$$

$$x_{SS} = X'\sqrt{(2y^2_{SS} l'^2_0 |\sin(\theta_{\rm HRS} - \theta'_{\rm HRS})|}, \tag{4.22}$$

where $\theta_{\rm HRS} = 13.2^\circ$ is spectrometer angle, and parameters of (l_0 and l'_0) are lengths from central position at sieve slit to vertex points ($z = 0, z$). The schematic explainable of parameters in Eq. 4.20 was given as Fig. 4.10.

The matrix elements of angles ($C_{x'(y')}$) were optimized by chi-square minimization. For events around a hole with a sieve slit, the chi-square of each hole ($\chi_{ss_{j,k}}$) when the carbon foil labeled k was selected, was written as follows:

$$\chi^2_{{\rm ss}_{j,k}} = \sum_{i=0}^{N} \frac{({\rm ss}^{\rm ref}_j - {\rm ss}_i)^2}{\sigma^2_j} \tag{4.23}$$

where ${\rm ss}^{\rm ref}_j$ is the central position about each sieve slit hole, j and k are labels of a sieve slit hole and a multi-carbon foil. The total chi-square of sieve slits ($\chi^2_{\rm ss}$) was written with the chi-square of each hole ($\chi^2_{{\rm ss}_{j,k}}$) as

$$\chi^2_{\rm ss} = \sum_{k=0}^{10} \sum_{j=0}^{N_{\rm hole}} \chi^2_{{\rm ss}_{j,k}} \tag{4.24}$$

After the minimization of chi-square with Eq. 4.24, the sieve slit holes can be seen clearly.

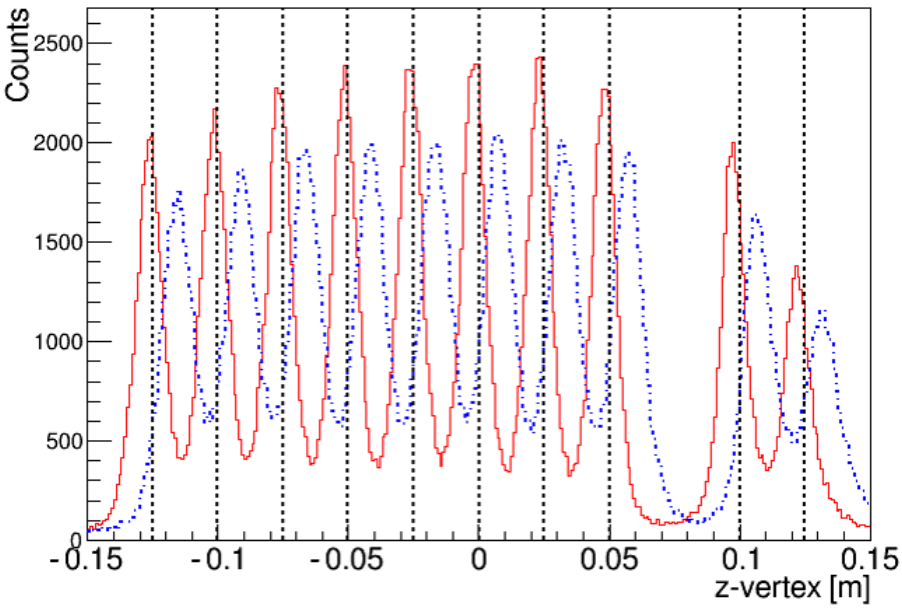

Figure 4.7: z-distribution with (red line) and without (blue dot line) z-calibration. The blue dashed and red lines show reconstructed the z-vertex in LHRS before and after the z correction. The black dashed lines show the positions of multi-foil target.

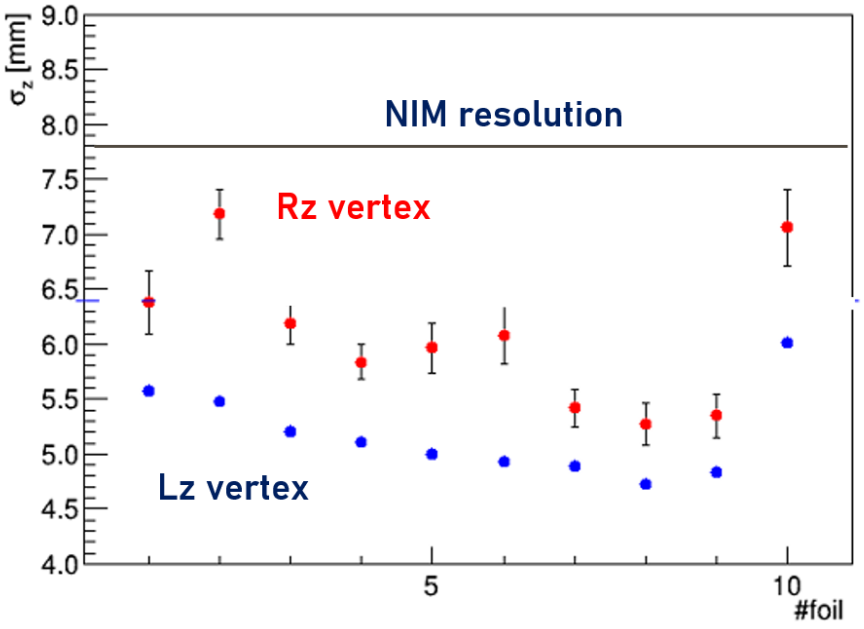

Figure 4.8: A fitting result with each carbon multi-folis. The blue and red points represents z-resolution obtained by fitting with Gaussian function in LHRS and RHRS, respectively.

■ Angle resolution

The tracking angles at target x'_{tar} and y'_{tar} were geometrically obtained from Eq. 4.20 and 4.22. However, a hole size of sieve slit was 2 mm or 4 mm in a diameter which was comparable to a typical angle resolution ($\Delta y' \times l_0 \sim$ a few mm), and had a thickness of 2.54 cm. The schematic

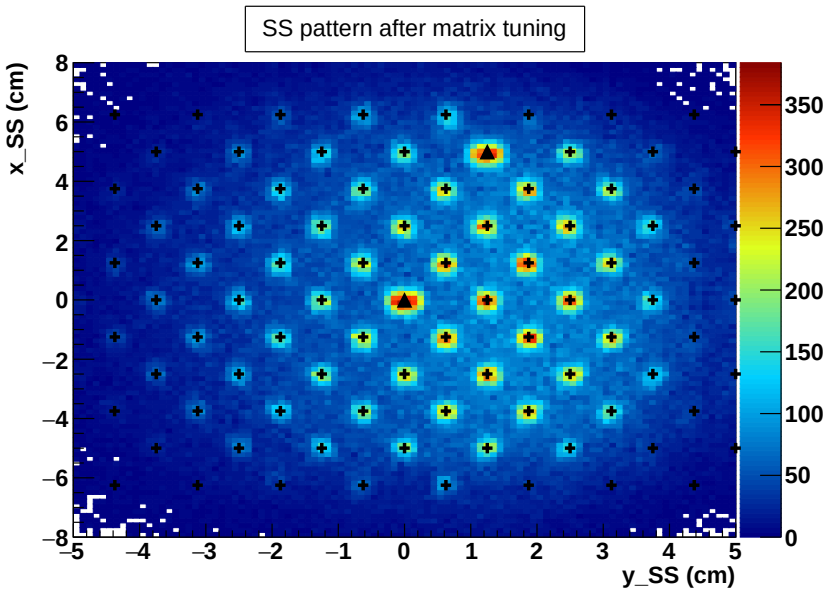

(a) Sieve Slit Pattern at LHRS

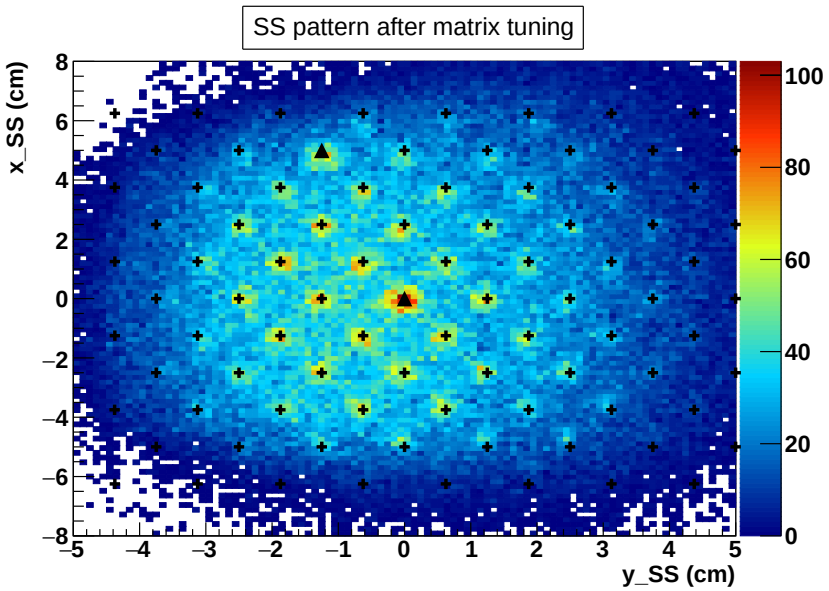

(b) Sieve Slit Pattern at RHRS

Figure 4.9: The distributions of sieve slit patterns after matrix tuning (a: LHRS, b: RHRS). The horizontal and vertex axes are the y and x positions at sieve slit, respectively. The black full cross and triangle up points shows the central point of sieve slit holes, whose diameters are 2 mm (full cross points) and 4 mm (triangle points).

of explanation of the position at sieve slit is shown in Fig. 4.10.

The angular resolution that best reproduced the experimental data was determined by generating the position distribution at the sieve slit for each change in the angular resolution in the Monte Carlo simulation. Figure 4.11 shows the position distributions in the sieve slit by MC simulation. The left figure in Fig. 4.11 shows the (x_{ss}, y_{ss}) distribution generated by MC simulation on assuming the angular resolution of zero. On the other hand, assuming a certain

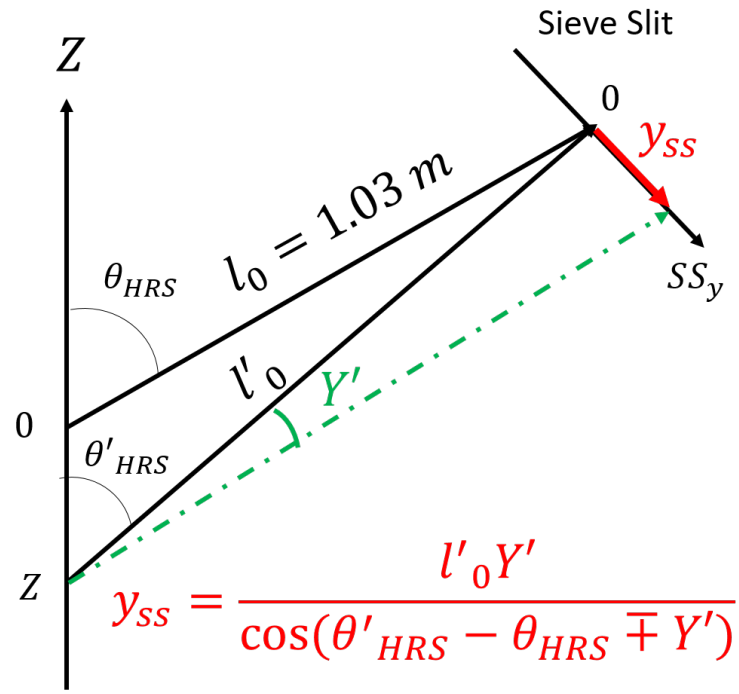

Figure 4.10: A diagram of the relationship between the sieve slit position (y_{SS}) and target position (z).

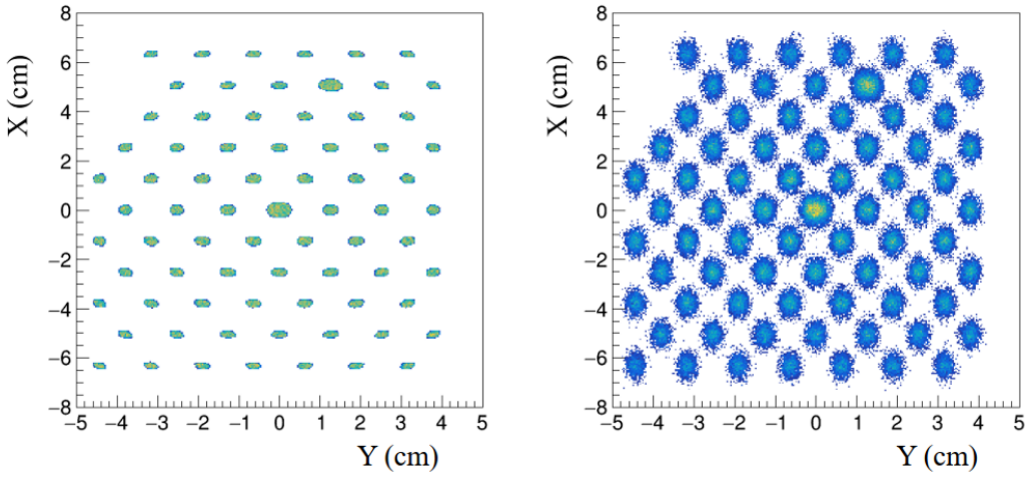

Figure 4.11: The simulation result with Monte Carlo simulation The left figure shows the (x_{ss}, y_{ss}) distribution obtained by the MC simulation in the sieve slit assuming the angular resolution of zero. The right figure shows shows the (x_{ss}, y_{ss}) distribution obtained by the MC simulation in the sieve slit assuming a certain resolution.

angular resolution in the MC simulation, the observed hole distribution was wider (right side of Fig. 4.11).

Selecting the central hole at $(x_{ss} = 0, y_{ss} = 0)$, both of distributions of x_{ss} and y_{ss} at the sieve slit were shown in Fig. 4.12. The dot point is experimental data and the blue histogram is the best fitting result in the central hole. The resolutions of angles, $\Delta x'$ and $\Delta y'$ at the target were 2.37×10^{-3} and 1.52×10^{-3}, respectively.

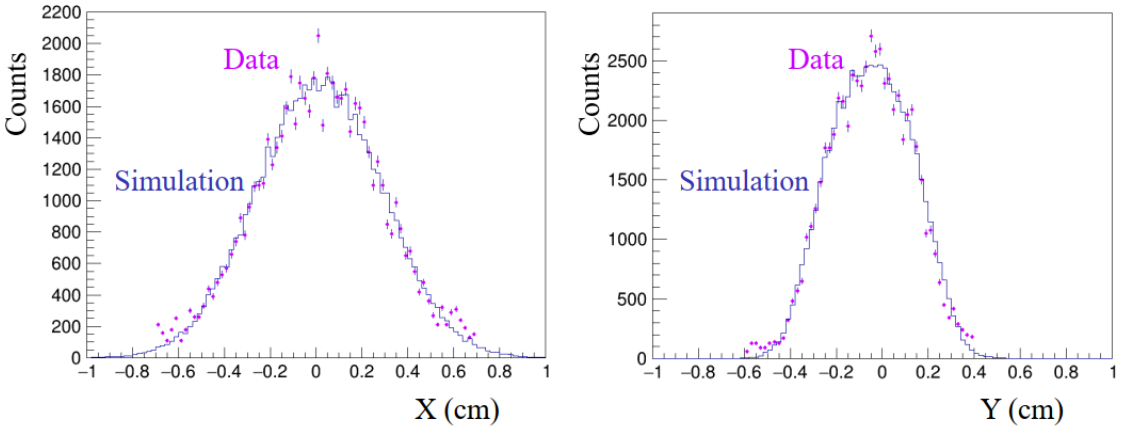

Figure 4.12: The reproduced position distributions with Monte Carlo simulation at sieve slit.

4.2.6 Energy loss correction

When charged particles passed through materials, the particles loss energy can be calculated with the Bethe-Bloch equation [66]. The electron beam lost energy while the electron passed though targets between the entrance window to the reaction point. On the other hands, the e' and K^+ lost energy in materials after the reactions occurred. Therefore, the particles energies $(E'_e, E'_{e'}, E'_K)$ at the reaction are given as :

$$E'_e = E_e - \delta E_e \ , \tag{4.25}$$
$$E'_{e'} = E_{e'} + \delta E_{e'} \ , \tag{4.26}$$
$$E'_K = E_K + \delta E_K \tag{4.27}$$

where $E_e, E_{e'}, E_K$ are particle energies, and $\delta E_e, \delta E_{e'}, \delta E_K$ are energy losses. By the measurement z-vertex point with Eq. 4.13, the energy loss of each charged particles can be estimated with the energy loss distributions by Geant4 simulation (see Sec. 4.4.3).

4.2.7 Momentum calibration

The momenta of scattered electrons and K^+ were calibrated with the missing masses of Λ and Σ^0 by using elementary reactions, $p(e, e'K^+)\Lambda/\Sigma^0$. The masses of Λ and Σ^0 are known precisely ($m_\Lambda = 1115.683(6)$, $m_{\Sigma^0} = 1192.64(2)$ MeV/c^2 [67]) since the matrix elements (C_p) in Eq. 4.16 was optimized with chi-square minimization. The chi-square for the momentum calibration was defined as:

$$\chi^2_{\Lambda,\ \Sigma^0} = \sum_{i=1}^{N} \frac{(m_{\Lambda,\Sigma^0} - m_i)^2}{\sigma^2_{\Lambda,\Sigma^0}}, \tag{4.28}$$

where m_i is measured missing masses with the hydrogen target. This calibration method was developed in the past hypernuclear experiment at JLab Hall C (E05-115) and achieved missing

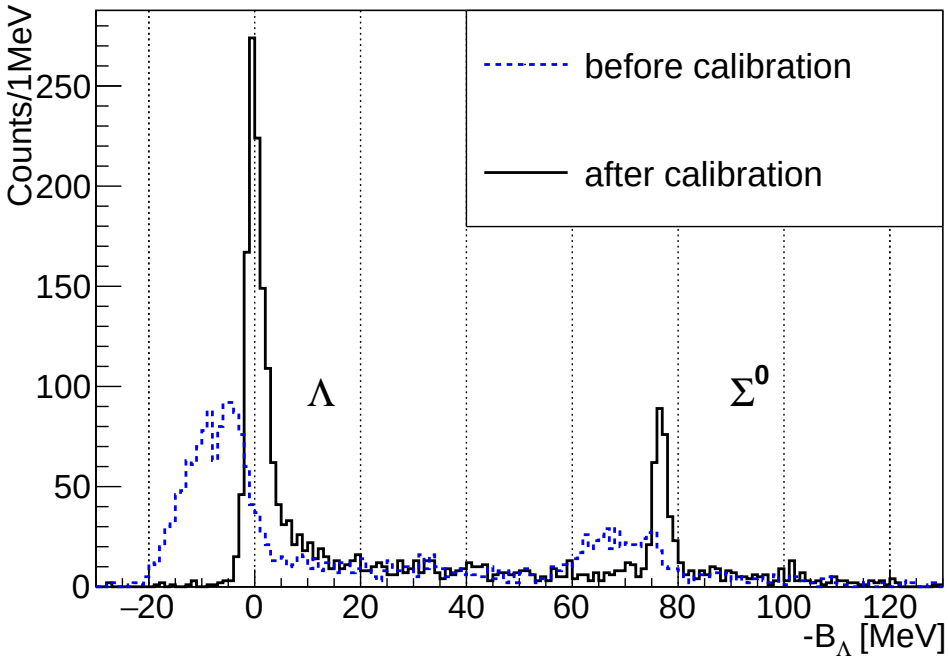

Figure 4.13: Comparison of the H$(e, e'K^+)\Lambda/\Sigma^0$ missing mass spectrum before and after calibration

mass resolution (0.78 MeV in FWHM). On the other hand, the experiment used he target with the 25-cm target. Since the z-dependence of the energy loss was not negligible, the energy resolution was known to be deteriorated. Therefore, the reconstruct momenta of K^+ and e' was calibrated by using Eq. 4.16, which included z-vertex parameters in order to take z-vertex dependence in the momenta into account.

The peaks of Λ and Σ^0 had radiative tails. The number of Λs and Σ^0s were estimated by fitting with the functions as following:

$$((f+h)\cdot g)(x) = (f\cdot g)(x) + (h\cdot g)(x), \tag{4.29}$$

$$f(x) := \frac{1}{\tau}\exp\left(-\frac{x}{\tau}\right),\ x\in[0,\infty], \tag{4.30}$$

$$g(x) := \frac{1}{2\pi\sigma^2}\exp\left(-\frac{(x-\mu)^2}{2\sigma^2}\right), \tag{4.31}$$

$$h(x) := \frac{1}{\pi c}\int_0^\infty \mathrm{e}^{-\mathrm{t}}\cos\left[t\frac{x-\mu}{c}+\frac{2t}{\pi}\log\left(\frac{t}{c}\right)\right]dt \tag{4.32}$$

where f, g and h are exponential, Gaussian and Landau functions, respectively. Figure 4.14 shows the $p(e, e'K^+)\Lambda/\Sigma^0$ missing mass spectra and convolution functions of Λ and Σ^0. Fitting results are summarized in Table 4.3. The energy resolutions of Λ and Σ^0 peaks are 3.3 and 3.5 MeV (FWHM), respectively, and the difference of measurement masses (MPV) of Λ and Σ from PDG values were -0.32 MeV/c^2, respectively.

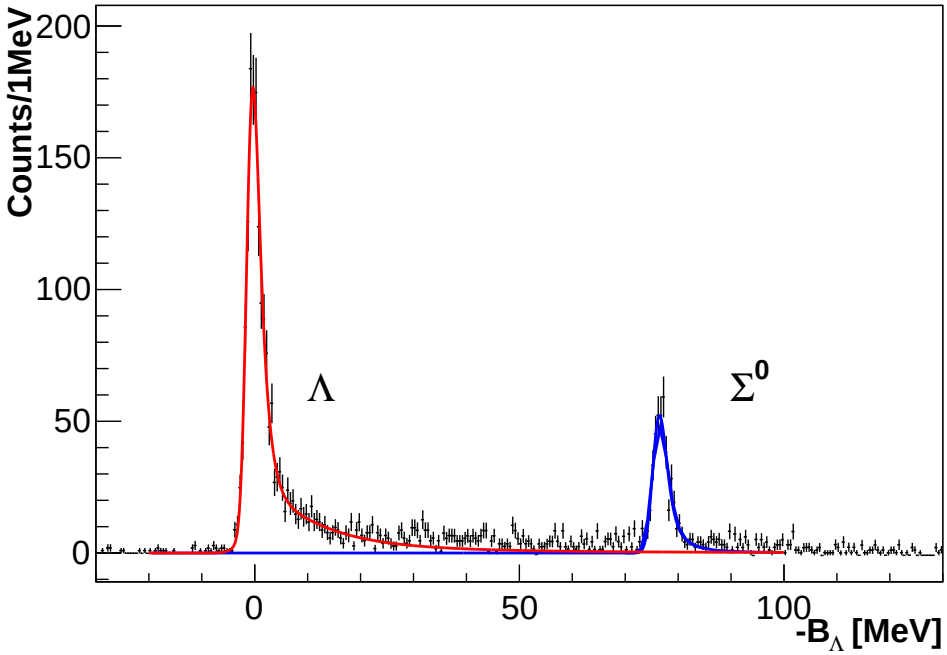

Figure 4.14: H$(e, e'K^+)\Lambda/\Sigma^0$ missing mass spectra

Table 4.3: Fitting results of elementary reaction

Fitting parameters	Λ	Σ^0
M_X (MPV) - M_{PDG} [MeV]	-0.32	-0.32
width (FWHM) [MeV]	3.3	3.5
Number of events	1940 ± 180	440 ± 80

4.3 Resolutions

The mass resolution is deduced from missing mass equation (Eq. 4.7) with error propagation method as :

$$\Delta M = \sqrt{\left(\frac{\partial M}{\partial p_e}\Delta p_e\right)^2 + \left(\frac{\partial M}{\partial p_{e'}}\Delta p_{e'}\right)^2 + \left(\frac{\partial M}{\partial p_K}\Delta p_K\right)^2 + \left(\frac{\partial M}{\partial \theta_{ee'}}\Delta \theta_{ee'}\right)^2 + \left(\frac{\partial M}{\partial \theta_{eK}}\Delta \theta_{eK}\right)^2}, \quad (4.33)$$

and these differential coefficients are described as :

$$\frac{\partial M}{\partial p_e} = \frac{1}{M}\left\{\beta_e(M_{tar} + E_e - E_K - E_{e'}) - p_e + p_{e'}\cos\theta_{ee'} + p_K\cos\theta_{eK}\right\}, \quad (4.34)$$

$$\frac{\partial M}{\partial p_{e'}} = -\frac{1}{M}\left\{\beta_{e'}(M_{tar} + E_e - E_{e'} - E_K) + p_{e'} + p_e\cos\theta_{ee'} + p_K\cos\theta_{eK}\right\}, \quad (4.35)$$

$$\frac{\partial M}{\partial p_K} = -\frac{1}{M}\left\{\beta_K(M_{tar} + E_e - E_{e'} - E_K) + p_K - p_e\cos\theta_{eK} + p_{e'}\cos\theta_{eK}\right\}, \quad (4.36)$$

$$\frac{\partial M}{\partial \theta_{ee'}} = -\frac{1}{M}\left\{p_e p_{e'}\sin\theta_{ee'} - p_{e'}p_K\sin(\theta_{ee'} + \theta_{eK})\right\}, \quad (4.37)$$

$$\frac{\partial M}{\partial \theta_{eK}} = -\frac{1}{M}\left\{p_e p_K\sin\theta_{eK} - p_{e'}p_K\sin(\theta_{ee'} + \theta_{eK})\right\}. \quad (4.38)$$

4.3.1 Angular resolutions at target

The $x'_{\rm tar}$ and $y'_{\rm tar}$ resolutions at target are evaluated in Sec. 4.2.5. In the calculation of missing mass resolution, the $\theta_{ee'}$ and θ_{eK} were used. The $x'_{\rm tar}$ and $y'_{\rm tar}$ were used for representing the momentum vector in the HRS coordinate system as:

$$\vec{p}_{\rm HRS} = \left(\frac{p}{\sqrt{1+(x'_{\rm tar})^2+(y'_{\rm tar})^2}} x'_{\rm tar}, \frac{p}{\sqrt{1+(x'_{\rm tar})^2+(y'_{\rm tar})^2}} y'_{\rm tar}, \frac{p}{\sqrt{1+(x'_{\rm tar})^2+(y'_{\rm tar})^2}} \right). \quad (4.39)$$

The $\theta_{ee'}$ θ_{eK} are particle angles in the HRS coordinate system. Hence, the $\vec{p}_{HallA}$ is deduced from $\vec{p}_{Hall}$ with a rotate matrix M_{rot} at the $y-z$ plane in the Hall A coordinate,

$$\vec{p}_{Hall} = M_{\rm rot}(\Theta_0) \cdot \vec{p}_{\rm HRS}, \quad (4.40)$$

$$= \frac{p}{\sqrt{1+(x'_{\rm tar})^2+(y'_{\rm tar})^2}} (x', (y'\cos\Theta_0 + \sin\Theta_0), (-y'\cos\Theta_0 + \sin\Theta_0)), \quad (4.41)$$

where Θ_0 is HRS angles of $+13.2^\circ$ for the RHRS, -13.2° for the LHRS, respectively. Therefore, the $\theta_{ee'}$ and θ_{eK} were calculated as :

$$\theta_{ee'} = \arccos\left(\frac{-y'_{\rm tar}\sin\Theta_0 + \cos\Theta_0}{\sqrt{1+(x'_{\rm tar})^2+(y'_{\rm tar})^2}} \right) \quad (4.42)$$

The angle is mainly depending on horizontal vertex $y'_{\rm tar}$, therefore the resolutions of $\theta_{ee'}$ and θ_{eK} were obtained as 1.52 mrad (σ).

4.3.2 Momentum resolutions

The momenta of e' and K^+ were calibrated by the missing masses of Λ and Σ^0, and the experiment did not take data to evaluate the momentum resolutions in each spectrometer directly. Therefore, the momentum resolution was estimated by the Monte Carlo simulation (Geant4) simulation. The momentum resolution of the HRS was evaluated in the past experiment through an elastic scattering reaction of electrons [56], and the Ref. [56] reported that the momentum resolution in a range of momentum acceptance ($\Delta p/p \leq 1.5\%$) was achieved to $\Delta p/p = 2.5 \times 10^{-4}$ (FWHM).

Under the same conditions of Ref. [56], the resolution of the momentum was evaluated with Geant4 simulation, and the result was obtained as $\Delta p/p = 2.5 \times 10^{-4}$ (FWHM) which is agreement with Ref. [56].

Fig 4.15 shows the simulation results about momentum resolutions in LHRS. The purple line shows the momentum distribution withthe z-vertex distribution ($|z| \leq 12.5$ cm) and without material, and this resolution was $\Delta p/p = 4.3 \times 10^{-4}$ (FWHM). The red line shows the momentum distributions including the z-vertex distribution and any materials, and had offsets due to energy loss in the materials. After energy loss correction, the blue line in Fig. 4.15 was obtained, and the momentum resolution was estimated to be $\Delta p/p = 1.1 \times 10^{-3}$. The resolution

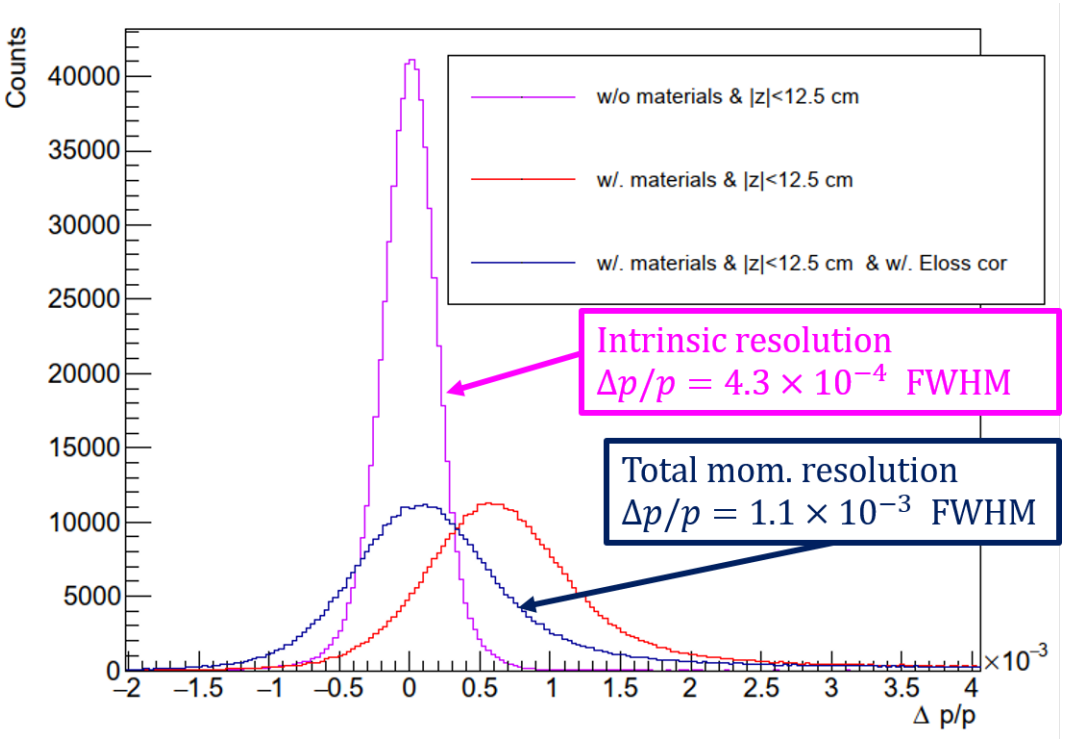

Figure 4.15: As results of momentum resolutions when the material setting were changed.

Table 4.4: Contribution of each term of a missing mass to mass resolution

terms	resolutions (FWHM)
$\Delta p_e/p_e$	2.0×10^{-4}
$\Delta p_{e'}/p_{e'}$	1.1×10^{-3}
$\Delta p_K/p_K$	1.1×10^{-3}
$\theta_{ee'}$	3.57 mrad
θ_{eK}	3.57 mrad
$\Lambda(\Sigma^0)$ missing Mass	3.4 (3.5) MeV

of $\Delta p/p = 1.1 \times 10^{-3}$ was including effects of straggling and multi scattering. The intrinsic resolution of momentum was obtained as $p = 4.3 \times 10^{-4} \times 2218$ MeV/c = 0.95 MeV/c (FWHM) from the purple histogram in Fig. 4.15. Hence, The resolution due to the straggling and multi scattering effects was estimated to be 2.3 MeV/c by subtracting the intrinsic resolution from total momentum resolution ($\Delta p/p = 1.1 \times 10^{-3}$).

The resolution of each term is summarized in Table 4.4

4.4 Monte Carlo simulation

A simulation code was used for accurately analysis to the Λ productions on tritium. A Monte Calro Simulation Code (SIMC), which is JLab standard simulation code, is based on a code written by N. Makins and T.G. O'Neill at SLAC. The code was modified for Hall A or C optics design: spectrometers and detectors, and for including energy loss, multiple scattering, radiative corre-

lations and kaon decay. The SIMC can handle electron scattering reactions $(e, e'\pi^+)$, $(e, e'K^+)$ and $(e, e'p)$. It was modified to including optics model of HRS and momentum distribution of proton in the ^{3}H [68, 69].

4.4.1 Event generation

The SIMC generated terms of a scattered electron momentum ($p_{e'}$), angles at target in both arms ($\theta^{tar}_{e'}$, $\phi^{tar}_{e'}$, θ^{tar}_{K}, ϕ^{tar}_{K}), a momentum of a proton in tritium (p_{fer}) and an excited energy of a residual system (nn). The generation parameters except for the proton momentum and the excited energy of the removal system were generated randomly with an uniform function within a range of spectrometer acceptance. The other parameters, the proton momentum and the excited energy of the removal system, were generated with probability functions (Fermi momentum or spectral function).

4.4.2 Virtual photon approximation

The momentum of virtual photons can be determined by momenta of a beam electron and scattered electron. The electron beam energy was controlled by the magnets at the Arc of the accelerator with the accuracy of 10^{-4} order and with spread of $\Delta E/E \sim 10^{-4}$ (FWHM). The momentum of scattered electrons at reaction point were generated with randomly within a range of HRS acceptance ($\Delta p_{e'}/p_{e'} \leq 4.5\%$). Hence, energies of the incoming and scattered electrons at vertex point ($E^{\rm ver}_{e(e')}$) were written as:

$$E^{\rm ver}_{e} = E^{\rm gen}_{e} - E^{\rm Eloss}_{e} = E^{\rm cent}_{e} + \Delta E_e - E^{\rm Eloss}_{e}, \tag{4.43}$$

$$E^{\rm ver}_{e'} = E^{\rm gen}_{e'} = E^{\rm cent}_{e'} + \Delta E_{e'}, \tag{4.44}$$

$$\tag{4.45}$$

where $E^{\rm gen}$ is the randomly generated energy within beam spread or LHRS acceptance range, and $E^{\rm Eloss}_e$ is the energy loss due to the radiation effect (see 4.4.3). In SIMC, the virtual photon was treated based on one photon exchange (ignored two photon exchange). In the one photon approximation, the virtual photon flux is following Eq. 2.7. Hence, the virtual photon momentum is simply described as:

$$\vec{p}_{\gamma^*} = \vec{p}_e{}^{\rm ver} - \vec{p}_{e'}{}^{\rm ver} = \vec{p}_e{}^{\rm gen} - \Delta p^{\rm Eloss}_e - \vec{p}_{e'}{}^{\rm gen}. \tag{4.46}$$

4.4.3 Radiation corrections

SIMC takes including the radiative corrections into account for the incident and scattered electrons. These corrections are considered about external Bremsstrahlung and internal contri-

Table 4.5: HRS material parameters were used to calculate kaon absorption and multiple scattering

Material	thickness (cm)	radiation length (cm)	Comment
Target			
Chamber cell	0.084	8.897	Aluminum
Target (z)	(12.5 + z)/0.234	0.02/0.031	Target (tritium/hydrogen)
Air	15	30420	
Mylar	0.01	28.7	
Hut			
Material	thickness (cm)	Radiation length (cm)	Note
Air	~ 180	30420	
Spectrometer exit window	0.02	3.56	Titanium
Aluminum Cage	0.0025	8.897	Aluminum around VDCs
Copper window (entrance/exit)	0.0125	1.436	each chamber
Mylar	0.0006	28.54	
Gold plating	8.5×10^{-4}	0.9415	
VDCs	5.25	15815	
mylar	0.12	28.54	at straw chamber
Aluminum	0.012	8.897	at straw chamber
Chamber gas	5.7	15815	
Cherenkov entrance	0.0125	8.897	Aluminum
Gas (GC)	137	19659	C02 at 1 atm
Mirrors of GC	1,4	254.5	1mm plexiglasss +13 mm phenolic honeycomb
GC exit foil	0.0125	8.897	
Al plate	1.3/1.9	8.907	before pre-shower/between the layer

butions. Eq. 4.43, 4.44 are rewrote with internal and external energy losses as:

$$E_e^{\rm ver} = E_e^{\rm gen} - \Delta E_e^{\rm in} - \Delta E_e^{\rm out}, \tag{4.47}$$

$$E_{e',K}^{\rm det} = E_{e',K}^{\rm ver} - \Delta E_{e',K}^{\rm in} - \Delta E_{e',K}^{\rm out}, \tag{4.48}$$

where $E_{e'}^{\rm det}$ and $E_K^{\rm det}$ are energies at detector plane, and $\Delta E_e^{\rm out}$ and $\Delta E_e^{\rm in}$ are energy loss by the real photon emission when electron pass through materials (external radiation), and by scattering by the electro-magnetic field from nuclei (internal radiation), respectively. Energy loss of incoming and outgoing electrons and K^+ are calculated by using HRS material maps and tracking. The materials of HRS and target systems are summarized in Table 4.5.

■ **Energy loss correction in the target system**

The target cell was designed with a special shape. Cell thickness was not uniformed and different from each target (see Table 3.7). The path length in the gas target and cell depended on z-vertex point and angle ϕ (horizontal direction in Hall A coordinate). The e' and K^+ are passed through two parts of the cell, an exit window (semicircle) or side (flat) cell (see Fig. 3.8). When a particle passed through the side cell, the effective cell thickness was multiplied by a factor of $1/\sin(13.2^\circ) \sim 4.4$ to have the actual thickness. In this case, the energy loss was evaluated about 1 MeV. In the case of exit window, the ϕ dependence is relatively small because of the hemispherical design. Figure 4.16 shows the target thickness dependence of the energy

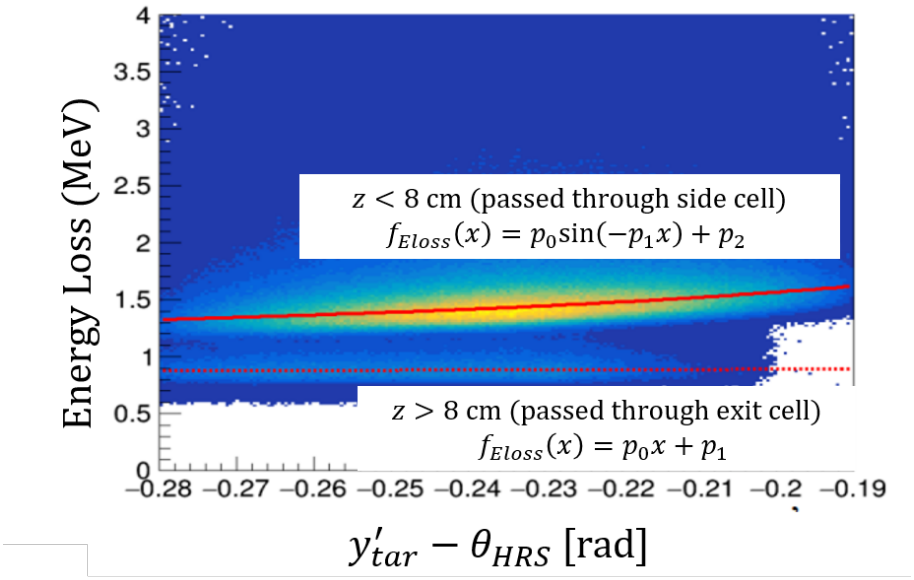

Figure 4.16: [$y'_{\rm tar}$ dependence of the energy loss in the target cell. The solid and dashed lines show $y'_{\rm tar}$ dependence of the energy when the particle passed though the side cell and exit cell, respectively.

Table 4.6: Fitting parameters of energy loss functions

particle	function	p_0	p_1	p_2
K^+	Eq. 4.49 ($z < 8$ cm)	-1.32	-4.62	2.04
	Eq. 4.50 ($z \geq 8$ cm)	0.0316	0.406	
e'	Eq. 4.49 ($z < 8$ cm)	-1.36	-4.60	2.10
	Eq. 4.50 ($z \geq 8$ cm)	0.0623	0.403	

loss which can be shown as $y'_{\rm tar} = \tan(\phi)$. The solid line shows the events passed through the side cell ($z \leq 8$ cm) and the dot line shows the particles passed through the exit cell ($z \geq 8$ cm). The fitting functions in Fig. 4.16 were used as:

$$f^{\rm ELoss}_{\rm K(e')}(y_{\rm tar}) = p_0 \sin(-p_1(\pm y'_{\rm tar} - \theta_{\rm HRS})) + p_2 \quad (z < 8 \text{ cm}), \tag{4.49}$$

$$f^{\rm ELoss}_{\rm K(e')}(y_{\rm tar}) = p_0(\pm y'_{\rm tar} - \theta_{\rm HRS}) + p_1 \quad (z \geq 8 \text{ cm}), \tag{4.50}$$

where $\theta_{\rm HRS}$ is the angle between the beam direction and central position of HRS (13.2°). The fitting parameters of the energy loss was summarized in Tab. 4.6

4.4.4 Proton Fermi momentum in ^{3}H

A nucleon in the nucleus moves with Fermi momentum ((p_{fer})), and this momentum probability is basically obtained by elastic scattering data. Figure 4.17 shows the Fermi momentum distribution of a nucleon in ^{3}H [69], and a proton momentum was generated in the SIMC with this distribution.

A proton having Fermi momentum in nucleus is described by the off-mass-shell model. Therefore, the energy conservation ($E_T = E_p + E_{nn}$) are broken. Hence, the tritium mass can not be

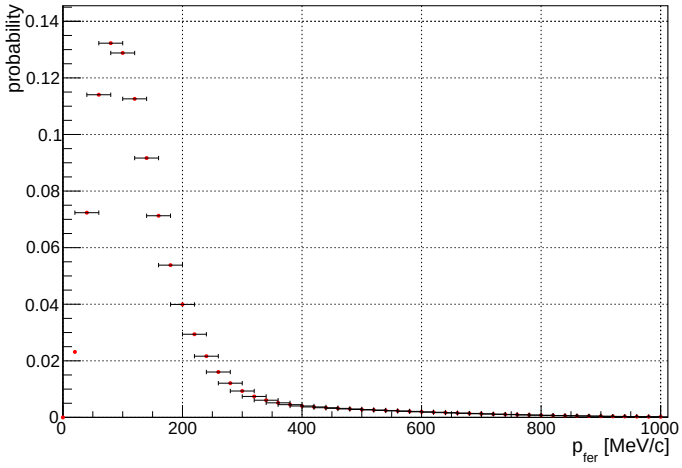

Figure 4.17: Fermi momentum of a proton in ^{3}H.

described with proton mass and removal mass,

$$M_T \neq \sqrt{M_p^2 + p_{fer}^2} + \sqrt{M_{nn}^2 + p_{fer}^2}. \tag{4.51}$$

In this analysis, off-shell masses of proton ($M_p^* \neq M_p$) is introduced. The tritium mass can be described with off-shell mass of proton and removal nucleus as :

$$M_T = \sqrt{(M_p^*)^2 + p_{fer}^2} + \sqrt{(M_{nn})^2 + p_{fer}^2}. \tag{4.52}$$

Hence, the off-shell proton energy is deduced from a following equation,

$$E_p = M_T - \sqrt{(M_{nn})^2 + |\vec{p}_{fer}|^2}. \tag{4.53}$$

4.4.5 Spectral function of ^{3}H

A spectral function gives probability of a bound nucleon momentum and excited energy of the residual system (nn). This is able to describe the off-shell state of a nucleon and the Fermi momentum was derived as:

$$f(k) = \int_0^\infty dE_m \;\; SF(k, E_m), \tag{4.54}$$

where $f(k)$ and $SF(k, E_m)$ are functions of the Fermi momentum and spectral function, and$k$ and E_m are parameters of a nucleon momentum and excited energy for the residual system (A-1), respectively. The removal energy E_m was defined as :

$$E_m = |E_A| - |E_{A-1}| + E_{A-1}^*, \tag{4.55}$$

where $|E_A|$ and $|E_{A-1}|$ are energy of target system and the residual system, and E_{A-1}^* is an excited energy of removal system. In the case of using SF, the mass of removal system M_{nn}^{SF} are

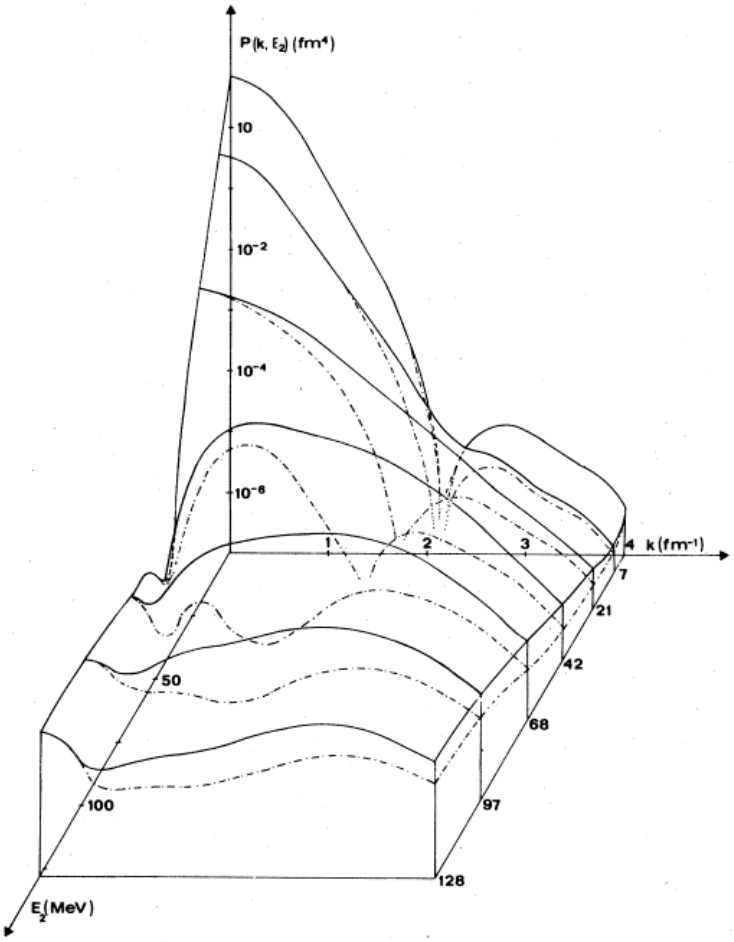

Figure 4.18: Spectral function about a proton in ^{3}H

given as :

$$M_{nn}^{`rmSF} = M_T - M_p + E_m \tag{4.56}$$

Hence, the off-shell proton energy in case of using SF can be obtained from Eq. 4.53 by using M_{nn}^{SF} instead of M_{nn}.

4.4.6 Hyperon production calculation

The reaction between the virtual photon and the target ($\gamma^* + {}^3\mathrm{H} \rightarrow \mathrm{K}^+ + \mathrm{Y}$) can be approximately treated as an elementary reaction $\gamma^* + p \rightarrow K^+ + Y$ because the energy of the virtual photon energy ($E_{\gamma^*} \sim 2.2$ GeV) is high enough to apply the impulse approximation model. The 4-vector momentum of generated Λ can be obtained with the energy and momentum conservation lows,

$$(E_e^{tar} - E_{e'}^{tar}) + E_p^* = E_K^{tar} + E_\Lambda, \tag{4.57}$$

$$(\vec{p}_e{}^{\,tar} - \vec{p}_{e'}{}^{\,tar}) + \vec{p}_{fer} = \vec{p}_K{}^{\,tar} + \vec{p}_\Lambda, \tag{4.58}$$

Table 4.7: Λ cross section for all angels at $Q^2 = 0.5$ GeV/c^2 measured at JLab Hall A [74]

Q^2 (GeV)	W (GeV)	t $(\text{GeV})^2$	θ_{cm} degree	$d\sigma/d\Omega$ (μb/sr)
0.462	1.848	-0.205	8.171	0.517 ± 0.036
0.466	1.831	-0.221	11.479	0.435 ± 0.026
0.493	1.841	-0.238	10.806	0.590 ± 0.039
0.483	1.823	-0.235	13.110	0.435 ± 0.025
0.484	1.817	-0.246	15.447	0.428 ± 0.021
0.487	1.814	-0.247	17,770	0.410 ± 0.019
0.487	1.813	-0.266	20.221	0.420 ± 0.019
0.487	1.805	-0.279	22.309	0.435 ± 0.019
0.508	1.806	-0.286	20.342	0.462 ± 0.024
0.495	1.806	-0.286	23.483	0.423 ± 0.019
0.494	1.806	-0.299	25.998	0.412 ± 0.018
0.495	1.804	-0.314	28.535	0.388 ± 0.017
0.495	1.804	-0.330	31.293	0.406 ± 0.017
0.500	1.797	-0.350	33.902	0.396 ± 0.017
0.497	1.807	-0.340	33.039	0.352 ± 0.022
0.495	1.806	-0.358	35.732	0.352 ± 0.019
0.496	1.803	-0.377	38.270	0.350 ± 0.018
0.497	1.802	-0.398	41.034	0.336 ± 0.018
0.497	1.803	-0.420	43.892	0.349 ± 0.019
0.507	1.796	-0.444	46.289	0.415 ± 0.020

where electron energy and momentum are used after energy loss (see Eq. 4.47), and E_p^* is off-shell proton energy. In the elemental reaction process, E_p^* and $\vec{p}_{fer}$ are treated to be zero. On the other hand, the 4-vector momentum about Λ-QF production is calculated by Eq. 4.57, 4.58. The Λ-QF spectrum is calculated with Fermi momentum, the information of elastic scattering effects and spectrometers acceptance. The energy and angle dependence of the cross section were considered with the factorized cross section model.

■ **The differential cross section calculation**

In the SIMC, the differential cross section is defined as :

$$\frac{d\sigma}{d\Omega}(Q^2, W, t, \phi) = f(Q^2)g(W)h(t)i(\phi), \tag{4.59}$$

where f, g, h, $i$are independent functions of the indicated variables, and the other variables are fixed. Each of independent function is described as following:

$$f(Q^2) = \text{Constant}, \tag{4.60}$$

$$g(W) = \frac{P_1 p_k^{cm}}{(W^2 - M_p^2)W} + \frac{P_2 W^2}{(P_3 W)^2 + (W^2 - P_4^2)^2}, \tag{4.61}$$

$$h(t_{min} - t) = P_1 \exp P_2(t_{min} - t), \tag{4.62}$$

$$i(\phi) = P_1 + P_2 \cos(\theta) + P_3 \cos(2\theta), \tag{4.63}$$

where $P_{1,2,3,4}$ are free parameters. As a result of fitting experimental data (see Table 4.7) with each independent function, the parameters of these functions were summarized in Table 4.8.

Table 4.8: The parameter values of independent functions

Functions	P_1	P_2	P_3	P_4
$f(Q^2)$	0.430 ± 0.005			
$g(W)$	4.470 ± 0.005	0.00089 ± 0.00086	0.0787 ± 0.02458	1.72
$h(t_{min} - t)$	0.4262 ± 0.0056	-2.144 ± 0.211		
$i(\phi)$	0.438 ± 0.006	-0.048 ± 0.009	0.008 ± 0.009	

Table 4.9: Main kaon decay channels used in SIMC. Other channels with branching raito less than 1% are ignored.

Decay mode	Branching ratio (%)
$\mu^+ + \nu_\mu$	63.56 ± 0.11
$\pi^+ + \pi^0$	20.67 ± 0.08
$\pi^+ + \pi^+ + \pi^-$	5.583 ± 0.024
$\pi^0 + e^+ + \nu_e$	5.07 ± 0.04
$\pi^0 + \mu^+ + \nu_\mu$	3.352 ± 0.033
$\pi^+ + \pi^0 + \pi^0$	1.760 ± 0.023

The Λ and Σ^0 production on tritium target were also calculated with these independent functions.

4.4.7 K^+ survival ratio

■ **K^+ decay factor**

A K^+ decays with the mean lifetime ($\tau = 1.2 \times 10^{-8}$ sec), so some of K^+s are decay in flight before they reach the end of HRS detectors. Table 4.9 shows decay channels of the K^+ taken into account in SIMC. In the SIMC, the probability of K^+ decay was calculated by :

$$P(l) = e^{-l/(c\tau\gamma\beta)}, \tag{4.64}$$

where l, β and γ are path length, velocity, and Lorentz factors of K^+, respectively. Figure 4.19 shows K^+ survival ratio in HRS acceptance. Dots points and line are a simulation result of survival ratio with Monte Carlo simulation (Geant4) and function with Eq. 4.64. In the range within HRS acceptance, Eq. 4.64 is a good agreement with Geant4 simulation.

■ **K^+ absorption factor**

Some K^+s were absorbed when they passed trough in materials. The factor of this effect (f_{absorp}) was estimated with the Monte Carlo simulation (Geant4) by comparing with number of events when inelastic processes are included and those when they were not included. As the results of simulation, this effects was 93% and which of momentum dependence of it was negligible small.

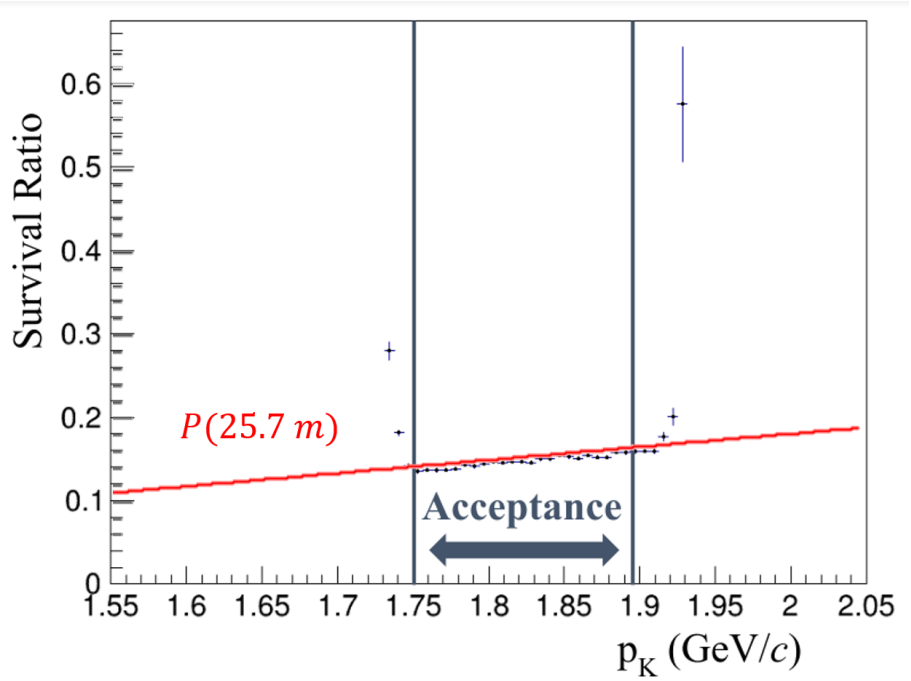

Figure 4.19: K^+ survival ration distribution. Dot points shows the simulation result of K^+ survival ratio with Geant4 and red lines is calculation with Eq. 4.64. In a range within the HRS acceptance, simulation results is comparable with calculation in Eq. 4.64.

4.4.8 Acceptance estimation

The momentum distribution of the HRS acceptance depends on momentum, and it was used for deducing cross section. For the acceptance estimation, SIMC generated angle and momentum with a spherical uniform function. The acceptance can be obtained by ratio of number of total generates N_{gen} and accepts (N_{acc}) in each solid angle setting ($\Delta\Omega$) as :

$$\Delta\Omega = \frac{N_{acc}}{N_{gen}}\Delta\Omega_{gen}. \tag{4.65}$$

For the study of systematical errors, the acceptance was estimated with Geant4 by changing the magnetic field of the spectrometer.

■ Systematical error estimation with Geant4

The Gean4 is more flexible to handle realistic magnetic field than SIMC and thus, it is suitable to study systematical error of the HRS acceptance. Figure 4.21 shows visualized HRS whose geometry is obtained from SIMC. The magnetic field of the dipole magnet was calculated with TOSCA [75] which is a software for 3-dimension magnetic field with the fine element method. On the other hand, quadrupole magnet, Q1, Q2 and Q3, were calculated with Kato-formula [76]. The magnetic fields were optimized in order to be reproduced experimental data. The strengths

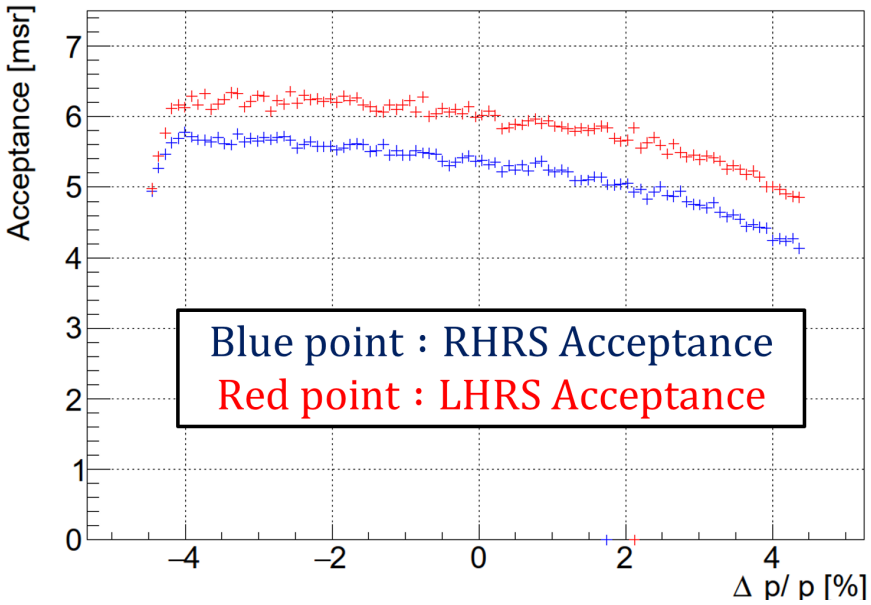

Figure 4.20: HRS acceptance distributions. The blue and red point show the acceptance of LHRS and RHRS, respectively. The vertical axis shows the momentum dispersion ($\Delta p/p \leq 4.5\%$)

of magnetic fields were tuned with keeping following ratio:

$$D_L : Q1_L : Q2_L : Q3_L = D_R : Q1_R : Q2_R : Q3_R, \tag{4.66}$$

where D and Q are dipole and quadrupoles, and the subscript is described labeling of LHRS or RHRS. The strength for the magnetic field of the dipole magnet was optimized so that the momentum distribution would match the experimental data. The Q2 and Q3 were used same model so the ratio of Q2 and Q3 can be fixed. Magnetic fields of Q1 and Q2 were optimized in order to be reproduced the missing mass and momentum distribution from experimental data.

Figure 4.22 shows the Q1 and Q2 magnetic strength dependencies of residue. Each of axis was scaled to match the best setting to be 1.

In a range of rad line in Fig. 4.22, the HRS acceptance systematical error was evaluated and shown in Fig.4.23. The blue shaded area shows systematical error from Geant4 simulation and red line is SIMC estimation. Over the 2.2 GeV/c region, the acceptance given from SIMC is within a range of systematical error. On the other hands, below 2.2 GeV/c momentum region shows the acceptance given SIMC is higher than one of Geant4. However, comparing average systematical error of Geant4, the difference from SIMC was about 2% which was within a range of evaluation of systematical error by Geant4.

The systematical error from virtual photon flux ($\Delta\Gamma$) and K^+ efficiency ($\Delta\Omega_K \times \varepsilon_{decay} \times \varepsilon_{absorp}$) can be evaluated with the acceptance error. The systematical error of virtual photon flux $\Delta\Gamma$ is 8.5% with Eq. 2.7 and systematical error of LHRS acceptance. Hence, the systematical error of $\Delta\Omega_K \times \varepsilon_{decay} \times \varepsilon_{absorp}$ is estimated to be 7.6% which is the average value of momentum region

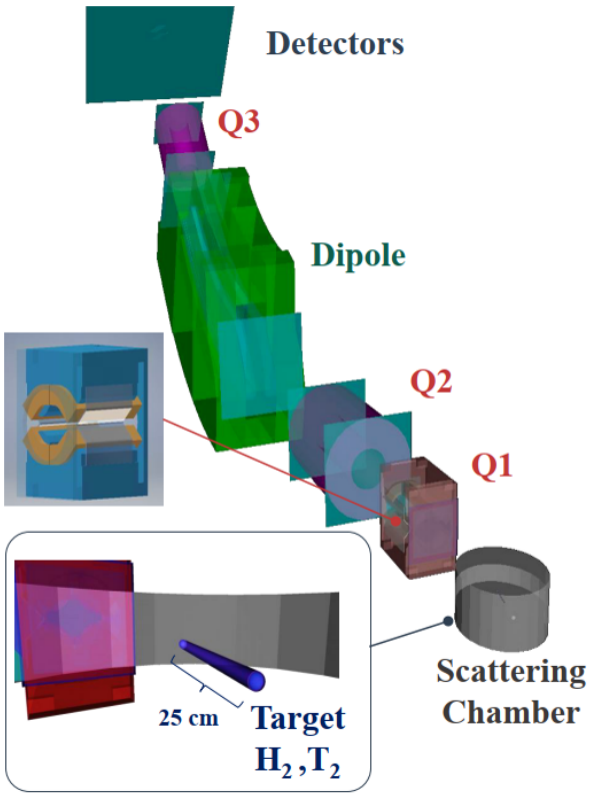

Figure 4.21: Visualization of HRS in Geant4 simulator

by Gean4 simulation.

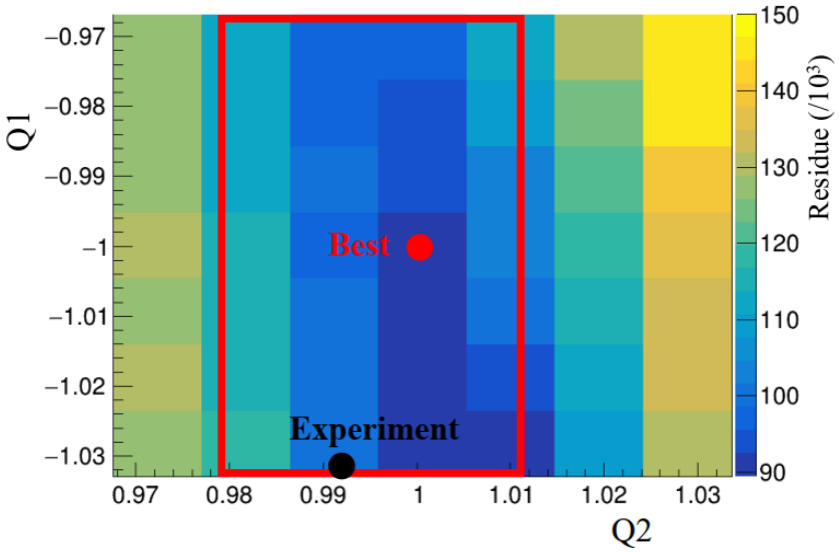

Figure 4.22: The Q1 and Q2 magnetic strength dependency of residue

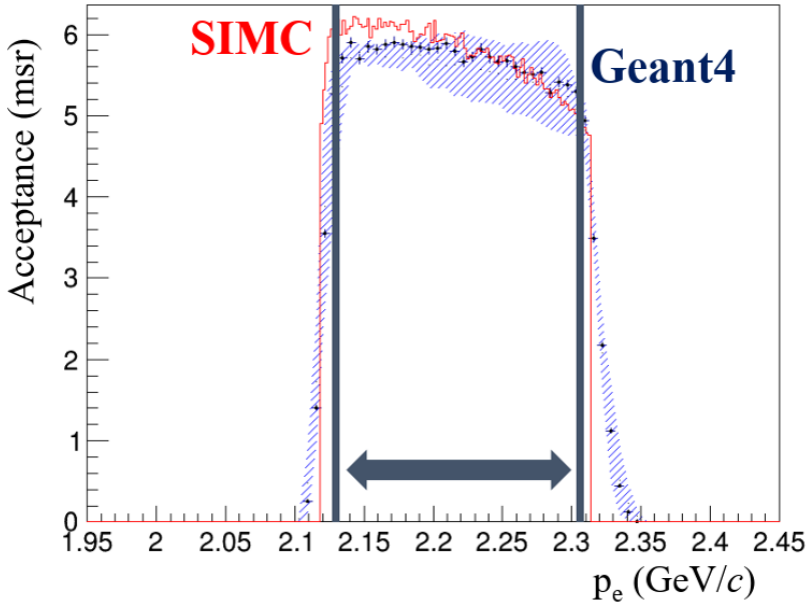

Figure 4.23: The acceptance distributions obtained by SIMC and Geant4

Table 4.10: The efficiencies and relative errors for contribution factors

term	efficiency (%)	Relative error (%)	reference
$\varepsilon_{\rm track}$	99	0.2	Sec. 4.5.4
$\varepsilon_{\rm density}$	90	0.3	Sec. 4.5.1
$\varepsilon_{\rm Tdecay}$	98.6	0.3	Sec. 4.6.3
$\varepsilon_{\rm DAQ}$	96.5	0.1	Sec. 4.5.2
$\varepsilon_{\rm ctime}$	94.7	3.6	Sec. 4.5
$\varepsilon_{\rm vertex}$	76.8	2.4	Sec. 4.5.5
$\varepsilon_{\rm PID}$	87.0	2.0	Sec. 4.5
$\varepsilon_{\rm single}$	98.7	1.3	Sec. 4.5.3
$\varepsilon_{\rm tot}^{\rm det}$	53.6	5.0	
$1/(1-\varepsilon_{\pi})$	3.2	3.3	Sec. 4.5
$1/(1-\varepsilon_{^{3}_{\Lambda}{\rm H}})$	7.4	5.1	Sec. 4.6.3
$1/(1-\varepsilon_{\Lambda})$	5.3	3.2	Sec. 4.6.3

4.5 Efficiencies

The detectors and any cut efficiencies were necessary in order to calculate the cross section (Eq. 2.6).

■Coincidence time cut efficiency

Figure 4.24 shows the coincidence time distributions. The black and blue dot lines show the coincidence time distributions with and without any Cherenkov cut. The Chernkov cuts of two aerogel (Eq.4.5 and 4.6) and gas (ADC $\geq$ 1800 ch) were applied to coincidence time. The peaks around $ct = 0$ ns and $ct = 3$ ns were represented K^+ and π^+, respectively. The π^+ peak has

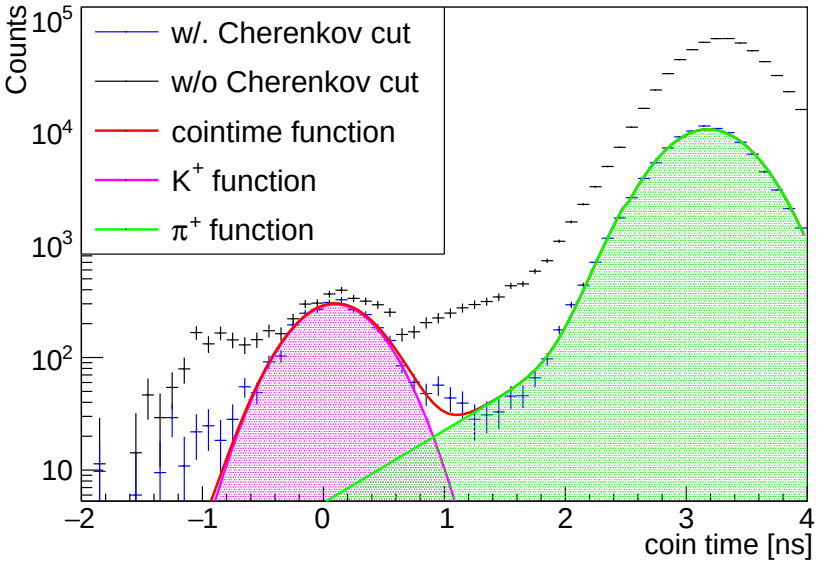

Figure 4.24: The points with errors of black and blue show the coincidence time distributions without and with any Cherekov cuts, respectively. The hatched regions of the red and green were fitting results of K^+ and π^+ peaks, respectively.

tail component which contaminates K^+ peak. In order to estimate π^+ contamination and K^+ events, the function for describing the π^+ and K^+ are

$$f_{\rm ct}(t) = h_K(t) + g_\pi(t) \tag{4.67}$$

$$h_K(t) = \frac{1}{\sqrt{2\pi}\sigma} \exp\left\{-\frac{(t-\mu)^2}{2\sigma^2}\right\}, \tag{4.68}$$

$$g_\pi(t) = \frac{1}{\sqrt{2\pi}\sigma} \exp\left\{-\frac{(t-\mu)^2}{2\sigma^2}\right\} + g_{tail}(t), \tag{4.69}$$

$$g_{tail}(t) = p_0 \exp\left\{\frac{(t-p_1)}{p_2}\right\} \cdot (1-\theta(t-p_3)), \tag{4.70}$$

where $h_K(t)$ and $g_\pi(t)$ are fitting function of K^+ and π^+, and $g_{tail}(t)$ is function to reproduce π^+ tail component. The $\theta(t-p_3)$ is step function which is 1 in case of $t - p_3 \geq 0$. When the coincidence time gate was applied to $-0.7 \leq t \leq 0.7$ ns from Fig. 4.24, the coincidence time cut efficiency was estimated at $94.7 \pm 3.4\%$ from fitting result with K^+ function (Eq. 4.68). Moreover, the π^+ contamination within a range of $-0.7 \leq t \leq 0.7$ ns was $3.2 \pm 3.2\%$.

■ AC cut efficiency

Two aerogel and gas Cherekov detectors were used for particle identification. The two aerogel Cherenkov cut efficiency were studied by fitting of K^+ peak. Figure 4.25 and 4.26 show the K^+ efficiency depending on AC1 and AC2 cuts. In case of study of AC1 cut efficiency, the AC2 and gas Cherenkov cut was applied to coincidence time. The AC1 and AC2 cut efficiencies in cut conditions (Eq. 4.5 and 4.6) were estimated at $\mathrm{Eff_{AC1}} = 99.9^{+0.1}_{-2.0}\%$ and $\mathrm{Eff_{AC2}} = 87.0^{+2.0}_{-2.0}\%$, respectively.

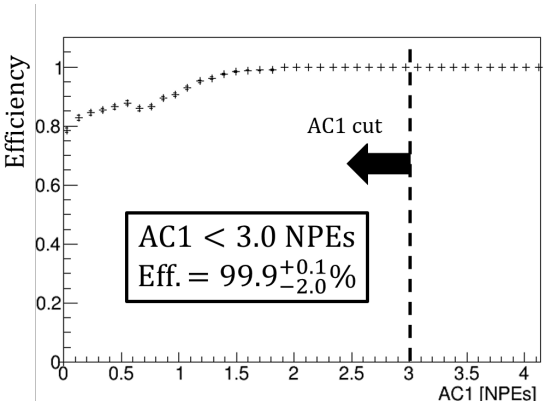

Figure 4.25: AC1 cut efficiency

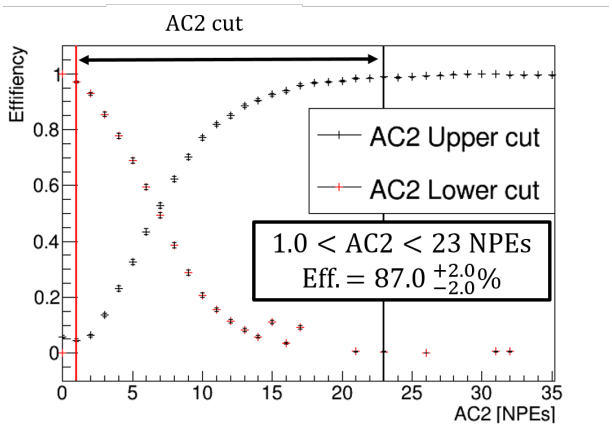

Figure 4.26: AC2 cut efficiency

Table 4.11: Fitting parameters obtained for the density charge calculation Fig.4.27 [59]

target	parameters	value
^{1}H	a	$(1.70 \pm 0.47) \times 10^{-4}$
	b	$(-9.0 \pm 0.12) \times 10^{-3}$
	c	1.0 ± 0.006
	$I_{\mathrm{beam}} = 22.5\ \mu$A	0.884 ± 0.01
^{3}H	a	$(1.04 \pm 0.25) \times 10^{-4}$
	b	$(-5.1 \pm 0.64) \times 10^{-3}$
	c	1.0 ± 0.003
	$I_{\mathrm{beam}} = 22.5\ \mu$A	0.901 ± 0.04

4.5.1 Target density efficiency

The experiment used high density electron beam so the target absorbed the energy which is beam loss ($\sim$ 50 W). it is depends on the beam current. Figure 4.27 shows the yield about target density depending on beam current in the hydrogen (left) and tritium target (right). The yield was normalized at 1 when the beam current is zero. The blue point is data, and the solid line is represented fitting function

$$f(I_{\mathrm{beam}}) = a \cdot I_{\mathrm{beam}}^2 + b \cdot I_{\mathrm{beam}} + c. \tag{4.71}$$

where $a, `b$ and c are free parameters given from fitting target density yield. The blue band and gray hatched are show the 95% confidence level about statistical error and a total error including systematical error, respectively. The fitting parameters are summarized in Table 4.11. In the case of beam current at 22.5 μA, the correction factor of tritium and hydrogen are $90.1 \pm 4\%$ and $88.3 \pm 1\%$, respectively.

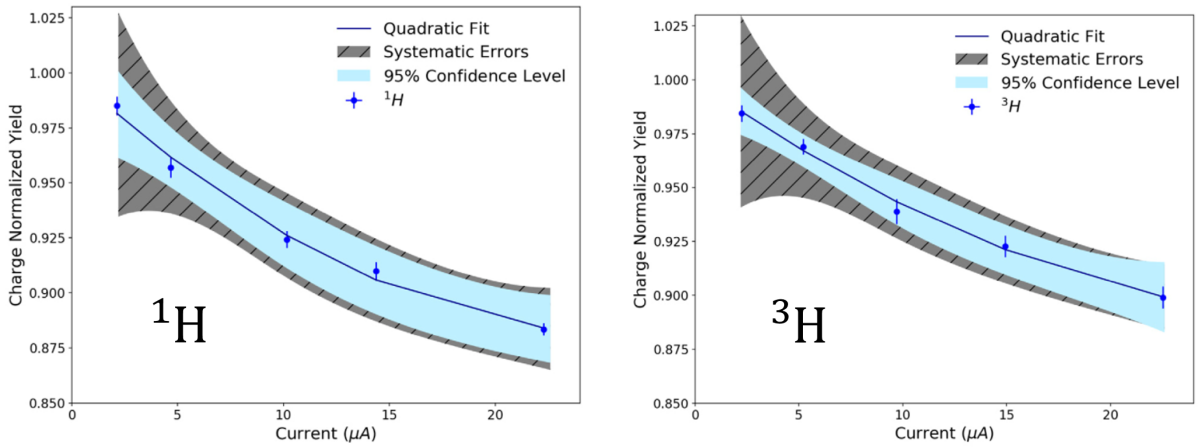

Figure 4.27: Beam current dependence of the target density distributions: (left :^{1}H target, right: ^{3}H target). the horizontal axis shows the beam current, and the vertical axis represents the normalized yield.

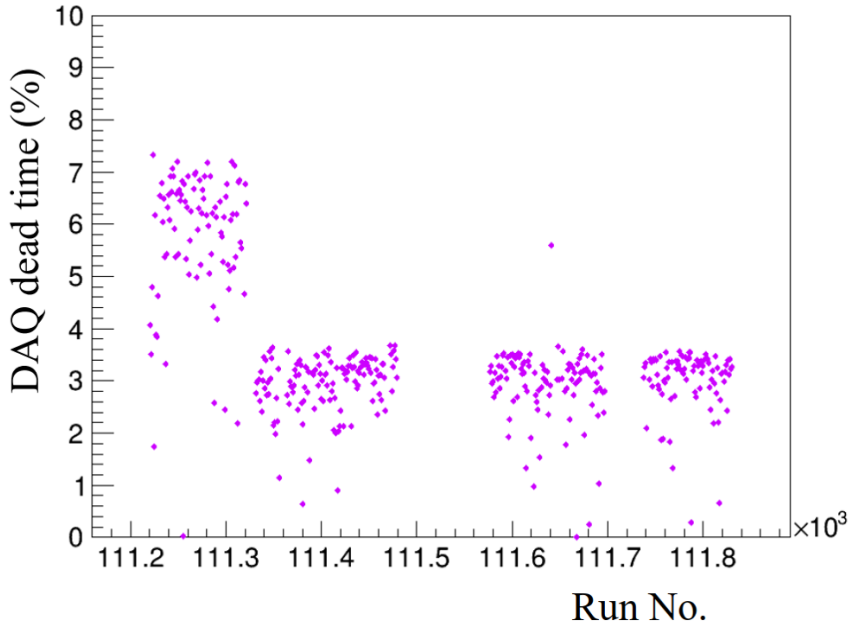

Figure 4.28: DAQ run dependence

4.5.2 DAQ efficiency

The signals from detectors are transported to DAQ system in order to process them. During the processing signals in DAQ, the coming signals were curtailed. Fig.4.28 shows the run dependence of DAQ dead time. DAQ efficiency of less than 111300 runs was worse because excessive data for a single trigger was taking in the period. After 111300 runs, the single trigger rate was decreasing by optimized pre-scalers. The DAQ efficiency of $96.5 \pm 0.1\%$ was obtained by an average value which was scaled by number of events in each run.

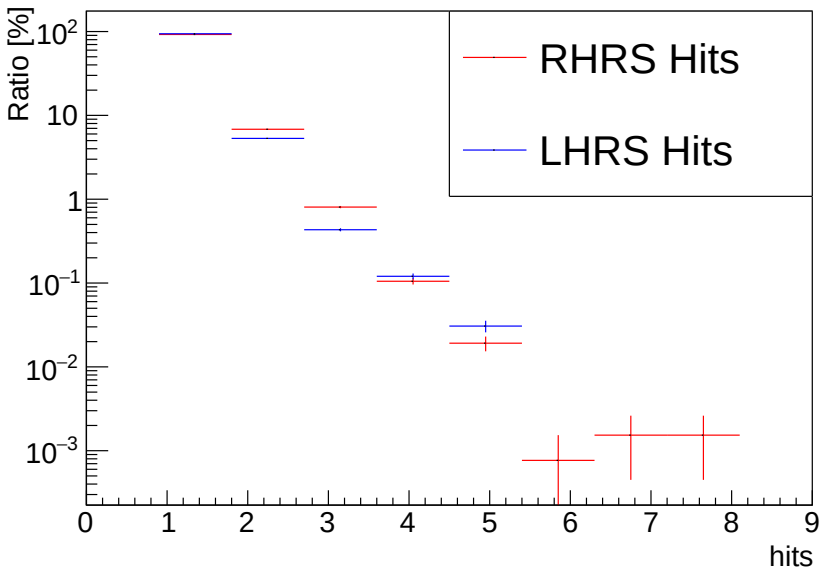

Figure 4.29: Multi hits probability in single triggers.

4.5.3 Single track efficiency

The multi hits events were recorded in DAQ. In the analysis, the only single hit events in both arm are used. Fig. 4.29 shows a ratio of the multi tracking. Multi events more than three hits can be ignored because their detection ratio were less than 1% of single hit events. Therefore, the single or two tracking events, $(M_R, M_L) = (1, 2)$ or $(2, 1)$, were considered in this study. The left and right spectra in Fig. 4.30 show coincidence time in case of $(M_R, M_L) = (1, 2)$ and $(2, 1)$, respectively. In the left spectrum in Fig. 4.30, clear K^+ peak was not found because most of these events consist of accidental coincidence events. The K^+ events were evaluated by upper limit of integration which was calculated with Gaussian and exponential functions. As a result of fitting of coincidence time spectrum in left of Fig. 4.30, the systematical error was 0.86%. The coincidence trigger in the experiment was adjusted to LHRS S2 signals so the T_{LS2} timing was able to be treated as trigger timing in the case of single tracking. In the case of $(M_R, M_L) = (2, 1)$, the TOF of second track in LHRS cannot be known. The number of real coincidence events in $(M_R, M_L) = (2, 1)$ was estimated to be 0.42% by fitting with Gaussian and exponential functions from the single tracking events because the probability of real coincidence was expected to be same between $(N_R, N_L) = (1, 1)$ and $(1, 2)$. Hence, the total systematical error about multi tracking was evaluated at 1.3%.

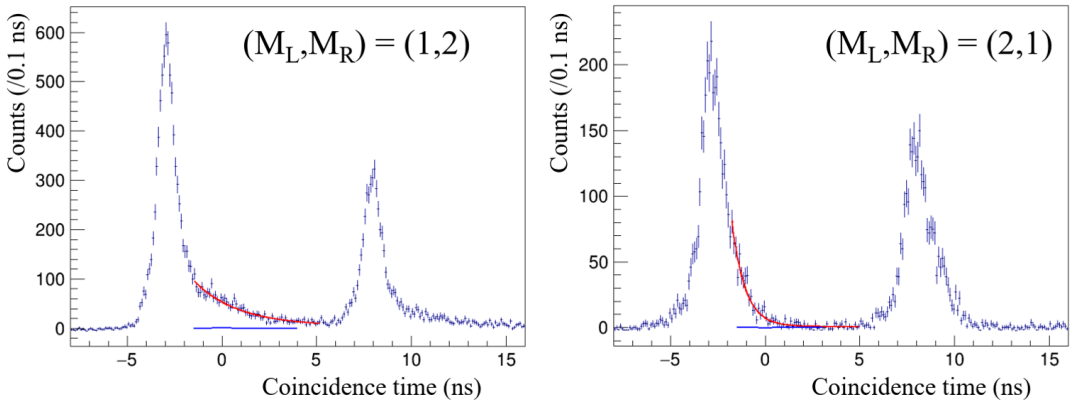

Figure 4.30: Missing mass spectrum in the $p(e, e'K^+)\Lambda/\Sigma^0$ reactions in multi-hits events. The left figure shows the missing mass spectrum when RHRS detected 2 hits evens, the right figure shows the missing mass spectrum when LHRS detected 2 hits events.

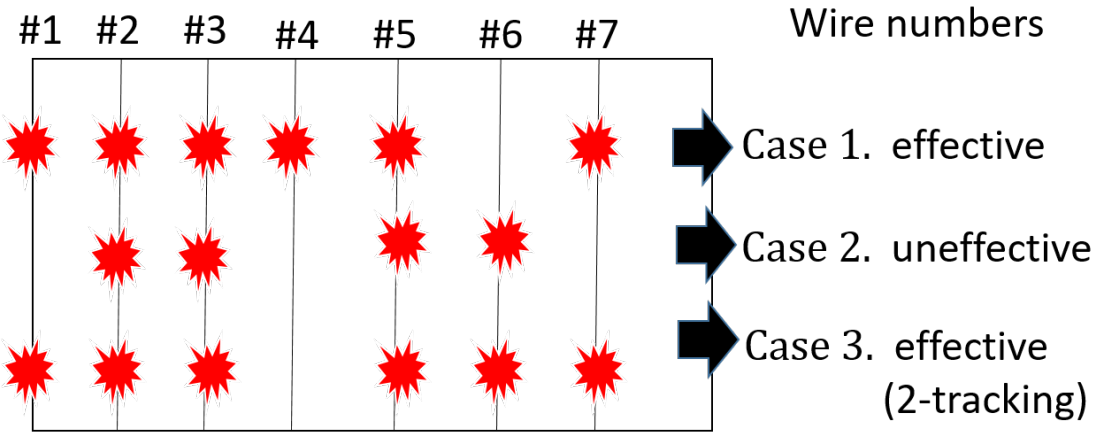

Figure 4.31: An example of the tracking estimation.

4.5.4 Tracking efficiency

The particle tracking was obtained from two VDCs in each HRS. In the analyzer code, the tracking in each VDC layer was required of consecutive hits more than three wires. Figure 4.31 is examples of wire detection patterns. In the case 2 in Fig. 4.31, this hits pattern is not effective because there is not three consecutive hits. On the one hand case 3, both two hitting clusters are effective and treated as two tracking detection. In order to study the tracking efficiency, the Monte Calro simulation was used. The simulation generated events according to the probability distribution of hits on each wire (see Fig. 4.32). Additionally, the generated events was made ineffective following the wire efficiency which is shown in Fig. 4.33. As a result of the simulation, the tracking efficiencies in each VDC layer was summarized in Table 4.12. The tracking efficiency in each HRS can be obtained as 99% which is calculated by multiplied all of plane efficiencies.

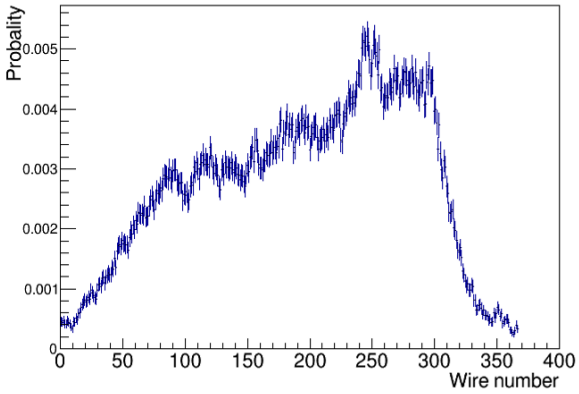

Figure 4.32: Wire hitting probability

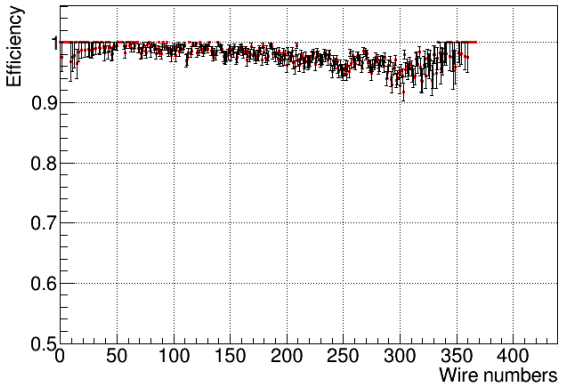

Figure 4.33: Wire efficiency

Table 4.12: VDC layer efficiency

layer	LHRS efficiency [%]	RHRS efficiency [%]
U1	99.72	99.78
V1	99.65	99.64
U2	99.8	99.78
V2	99.73	99,80
Tracking	$98.90^{+0.12}_{-0.18}$	$99.18^{+0.09}_{-0.19}$

4.5.5 z-vertex cut efficiency

After z-vertex calibration, each of reconstructed z-vertex resolution was achieved less than 5 mm (σ). In the production events, each of z reconstruction is expected to be same so the accidental events can be removed from information of z difference between z_R and z_L, and z average $(z_R + z + L)/2$. Figure 4.34 shows the correlation between z average and z difference. The two clusters composed productions from aluminum cells, and the events within a red square were selected as a coincidence events. The other events composed accidental coincidence.

The z-vertex cut was applied to remove background events which were produced from the aluminum cell at an entrance or exit windows or accidental coincidence. Figure 4.35 shows measurement average z -vertex distribution.

It consists of two peaks come from the aluminum cells and gas spectrum. In order to be estimated the z-vertex efficiency, the fitting functions of the aluminum cells f_{Al} and gas f_{gas} were used as following function, respectively:

$$f_{\mathrm{Al}}(z) = g_1(z) + g_2(z), \tag{4.72}$$

$$f_{\mathrm{gas}}(z) = \int \{g_1(z-x) + g_2(z-x)\}h(x)\ dx, \tag{4.73}$$

$$g(x) : p_0 \exp\left(-\frac{(x-p_1)^2}{2{p_2}^2}\right), \tag{4.74}$$

$$h(x) : p_0(x-p_1)^2 + p_2, \tag{4.75}$$

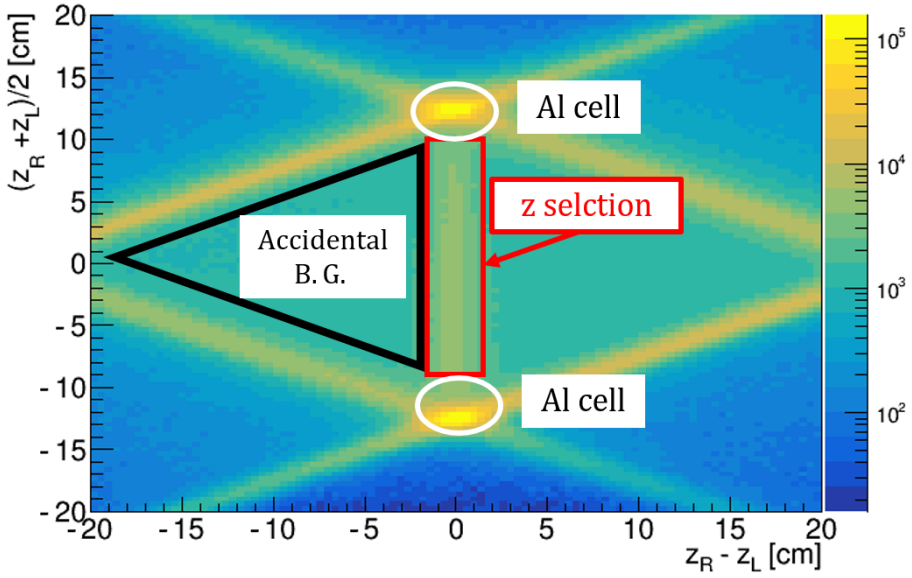

Figure 4.34: Correlation between mean z and z-difference.

where $g(x)$ and $h(x)$ are Gaussian and quadratic functions, respectively. The gas function was described as contribution function with Gaussian and two quadratic functions, and each of the aluminum cell were described two Gaussian functions. The number of gas events were estimated by the integral of the gas function within a selection cut. Figure 4.36 shows the efficiencies of the gas and aluminum events depending on z average cut. When the z average cut was applied to $|z| \leq 10$ cm, the gas and the aluminum efficiencies were 0.80 ± 0.08 and $(1.3 \pm 1.4)^{-4}$, respectively. The aluminum contamination can be ignored because it is evaluated less than 0.3%. The z-diff $(z_R - z_L)$ cut efficiency was evaluated with $p(e, e'K^+)\Lambda/\Sigma^0$ missing mass spectra and obtained as 96%. Moreover, the efficiency of the mean vertex cut was estimated from Λ survival ratio with z-mean and z-differential cut. As a result of analyzing, the efficiency of total z-vertex cut, z-mean ($|z_{mean}| \leq 10$ cm) and z-difference ($|z_{diff}| < 2.5$ cm) cuts, is $76.8 \pm 2.4\%$.

4.6 Background estimation

4.6.1 Accidental background

The distribution of $e'K^+$ accidental background events, which were contaminated in missing mass spectra, enabled us to be obtained by selecting the coincidence time cut. Figure 4.37 (a) shows the coincidence time distribution so that K^+ peak exists on the offset of x-axis (0 ns). The $e'K^+$ accidental events were selected eight accidental coincidence bunches in hatched area in Fig. 4.37 (a). Figure 4.37 (b) shows a missing mass spectrum of the $e'K^+$ accidental background. The number of $e'K^+$ accidental events below the K^+ events selection was obtained

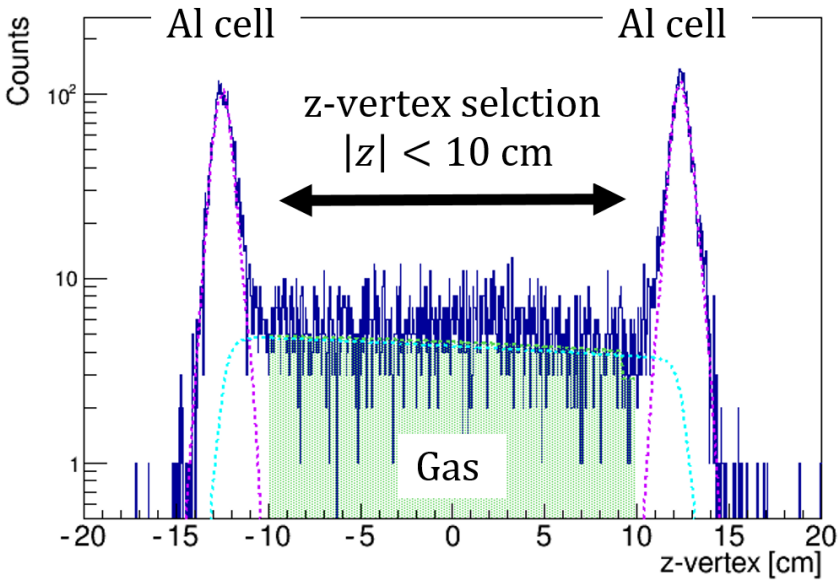

Figure 4.35: z-vertex fit result. The two peaks around $z = \pm 15$ cm represented the Al cell, and green hatched area was fitting result with gas events.

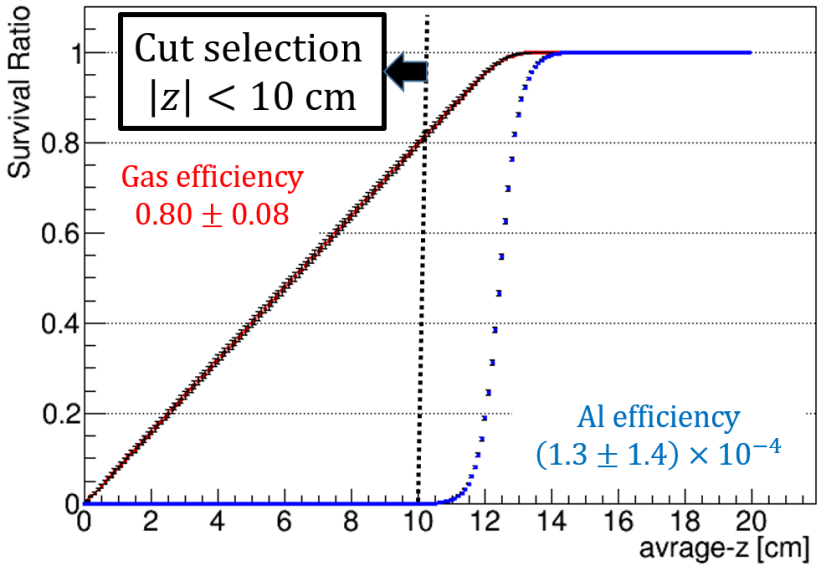

Figure 4.36: z-vertex cut efficiency. The red dot points shows the efficiency of the gas events obtained by fitting (green hatched area) in Fig.4.35, and blue one represents the efficiency of the aluminum events which was estimated by fitting with the aluminum cells (purple dot lines) in Fig.4.35.

by scaled with ratio of coincidence gates.

■ **Mixed event analysis**

To collect more $e'K^+$ accidental events, the mixed event analysis was applied to the accidental background analysis. In this method, the accidental $e'K^+$ coincidence were randomly combined in off-line analysis (see Fig. 4.38 (a)), and successful in 100 times more than accidental

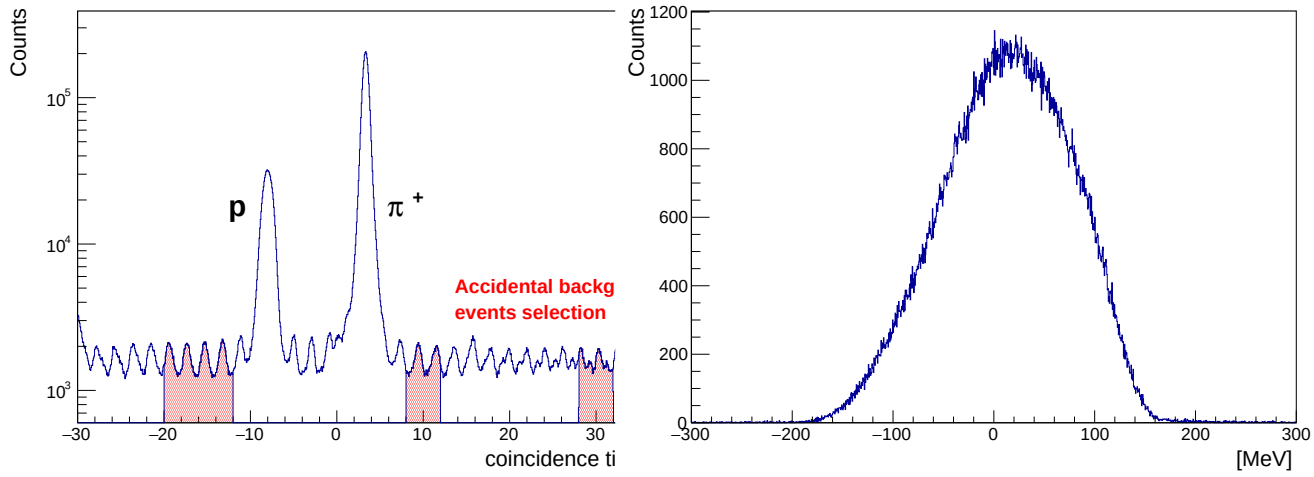

(a) Accidental background event selection (b) missing mass with accidental background events

Figure 4.37: Accidental background event selection

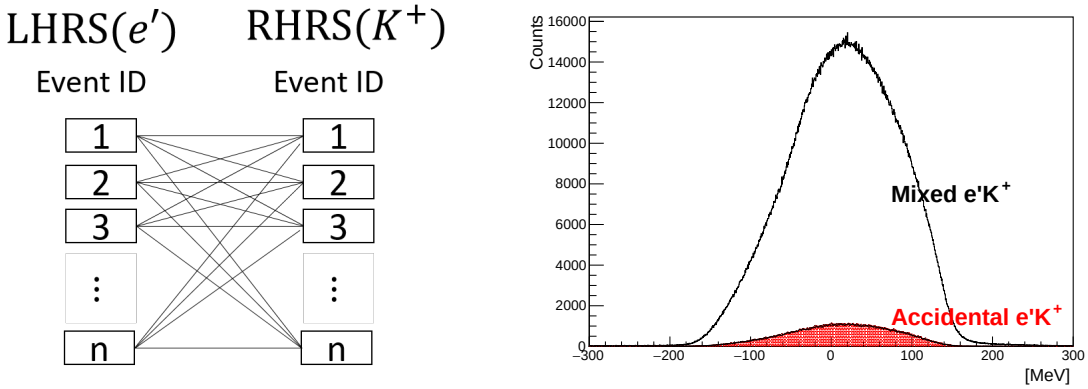

(a) Accidental background event selection

(b) missing mass distribution with mixed events and accidental events

Figure 4.38: Mixed event analysis

coincidence obtained from accidental gate. This analysis method is effective to make small the systematical error from accidental background subtraction from the original spectrum.

4.6.2 Contamination from $p(e, e'K^+)\Lambda$ production

A few percent of H was known to contaminate ^{3}H target. Hence, Λs, which are produced from the reaction with the H contamination in the ^{3}H target, was included in the $^3\mathrm{H}(e, e'K^+)X$ missing mass spectrum. The contamination rate of Λ can be estimated from missing mass spectrum on the $p(e, e'K^+)\Lambda$ reaction because the Λ productions from H contamination were expected to make peaks around the Λ threshold. Fig. 4.39 shows the missing mass spectra with ^{3}H target. The black points with errors represent the missing mass spectrum on the $p(e, e'K^+)\Lambda$ reaction given by experimental data. The blue line is the missing mass spectrum assuming the hydrogen

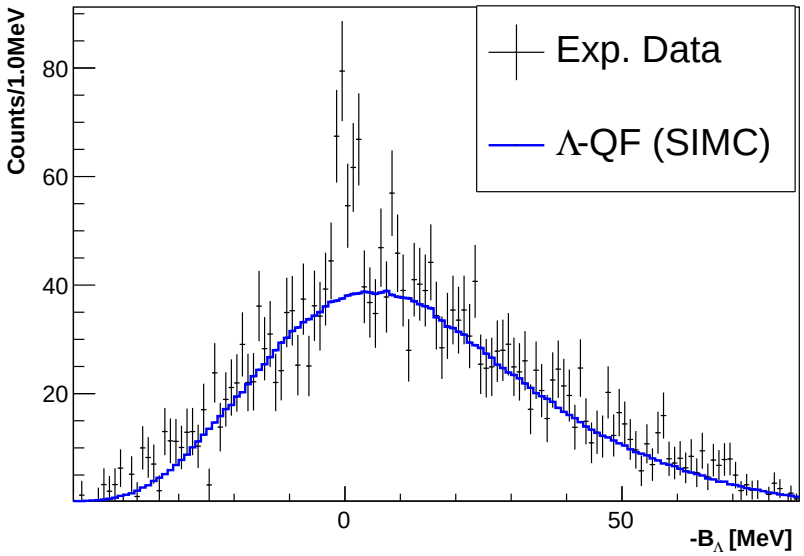

Figure 4.39: The missing mass distribution of the ^{3}H$(e,e'K^+)X$ reaction assuming H target mass. Λ events produced by the reaction with ^{1}H in ^{3}H target made peak near $-B_\Lambda \sim 0$ MeV. The blue line is the missing mass spectrum assuming the hydrogen mass obtained by the SIMC. The Λ productions events in the $p(e,e'K^+)\Lambda$ reaction were evaluated by subtracting the Λ-QF productions obtained by the SIMC from the experimental events.

mass obtained by the SIMC. This spectrum was scaled by fitting it with the experimental data in Fig. 4.39. The Λ productions events in the $p(e,e'K^+)\Lambda$ reaction were evaluated by subtracting the Λ-QF productions obtained by the SIMC from the experimental events. The statistical error on the number of the Λ productions in the $p(e,e'K^+)\Lambda$ reaction were evaluated by the error propagation of statistical errors between the experimental data and the SIMC. As a result of estimation of Λ productions in the $p(e,e'K^+)\Lambda$ reaction was obtained at 190 ± 30 counts.

4.6.3 ^{3}He contamination

^{3}H is radioisotope and decayed to ^{3}He as a following process,

$$^3\mathrm{H} \rightarrow {}^3\mathrm{He} + e^- + \bar{\nu}_e. \tag{4.76}$$

The number of decayed ^{3}He can be described by an exponential function as

$$N_{^3\mathrm{He}}(t) = N_{^3\mathrm{H}} \exp\left(-\frac{t}{\tau}\right), \tag{4.77}$$

where τ is lifetime of ^{3}H at $\tau = (12.32 \pm 0.02)/\ln(2)$ years. The experiment was performed 90 ± 14 days after a gas filling so ^{3}He contamination and loss of ^{3}H can be deduced at $1.4 \pm 0.3\%$ from Eq. 4.77.

The contamination of ^{3}He reacted with virtual photon, and produced the Λ-QF productions through the ^{3}He$(e,e'K^+)\Lambda(pn)$ reaction. These productions are expected to be included in the

Λ-QF spectrum on $^{3}\mathrm{H}(e,e'K^{+})\Lambda(nn)$ reaction as a background. The production ration of Λ-QF ($R_{QF} = \sigma_{\Lambda}^{^{3}\mathrm{He}}/\sigma_{\Lambda}^{^{3}\mathrm{H}}$) was estimated at 2.12 ± 0.03 with a reference to an averaged ratio of cross section ($R = \sigma_{^{3}\mathrm{He}}/\sigma_{^{3}\mathrm{H}}$) from ^{3}H Fermi momentum which is reported in Ref. [72]. Therefore, the $^{3}_{\Lambda}$H contamination was calculated by $N_{^{3}\mathrm{He}} \times R$, and obtained at $3.0 \pm 0.7\%$.

Chapter 5 Results and discussion

In this chapter, the results of the $\mathrm{H}(e,e'K^+)\Lambda/\Sigma^0$ and $^3\mathrm{H}(e,e'K^+)X$ missing mass spectra will be shown and discussed.

5.1 Cross section

The differential cross section is written as:

$$\left(\frac{d\bar{\sigma}}{d\Omega_K}\right) = \frac{1}{N_T}\frac{1}{N_{\gamma^*}}\frac{1}{\varepsilon_{\mathrm{det}}}\sum_{i=0}^{N_{\mathrm{hyp}}}\frac{1}{\varepsilon_K(\boldsymbol{p}^i_{e'},\boldsymbol{p}^i_K)d\Omega_K}, \tag{5.1}$$

where $\varepsilon_{\mathrm{det}}$, ε_K and $d\Omega_K$ are the detector efficiency, the K^+ efficiency ($\varepsilon_K = \varepsilon_{\mathrm{decay}} \times \varepsilon_{\mathrm{absorp}}$) and the momentum acceptance of the RHRS discussed in the previous section (Sec. 4). The number of nucleons (N_T) in Eq. 5.1 is written by the follow equation:

$$N_T = \frac{x_T}{A}N_A \times f(\mathrm{I_{beam}}), \tag{5.2}$$

where N_A, x_T and $f(\mathrm{I_{beam}})$ are the Avogadro's constant, the target thickness (g/cm^2) and the scaling factor of the target density (see Sec. 4.5.1). Other parameters in Eq. 5.1, such as the number of virtual photons (N_{γ^*}) and the Λ-QF productions (N_{hyp}) will discuss in Sec. 5.1.1 and 5.1.2.

5.1.1 Number of the virtual photons

The number of virtual photons is written by the follow equation:

$$N_\gamma = \frac{Q}{e}\int\int \Gamma d\Omega_{e'}dE_{e'}, \tag{5.3}$$

where Γ and Q/e are the virtual photon flux calculated by Eq. 2.7 and the number of beam electrons. The total charges of the beam electrons irradiated to the ^{1}H and the ^{3}H targets were 14 C and 4.7 C, respectively (see. Tab. 3.10). The integral regions in the momenta of scattered electrons in the Λ, Σ^0 and $nn\Lambda$ productions will explain in Sec. 5.1.1 and 5.1.1.

■ Number of the virtual photons in Λ and Σ^0 productions data

Fig. 5.1 shows a momentum correlation between momenta of the e' and K^+. The Λ and Σ^0 production events were selected in the range of scattered electron momentum within $2.092 \leq p_{e'} \leq 2.160$ GeV/c and $2.010 \leq p_{e'} \leq 2.108$ GeV/c, respectively. The number of the virtual

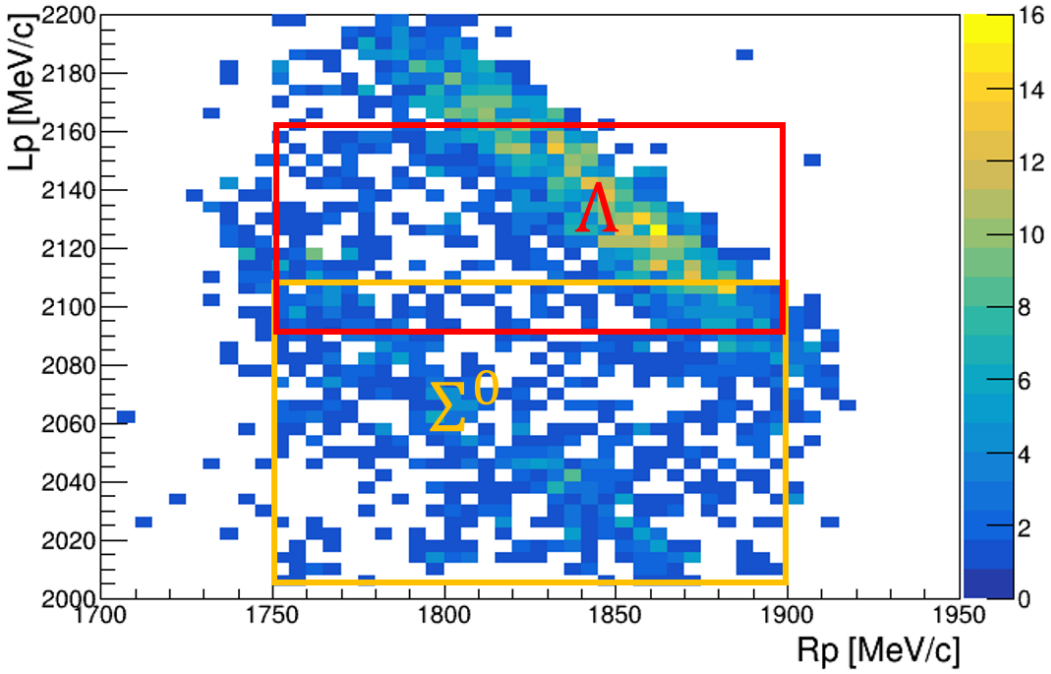

Figure 5.1: The momentum correlation between K^+ and e'. There were two clusters, Λ (right-up) and Σ^0 (left-down) productions. The Λ and Σ^0 productions were selected in the area enclosed by the red box ($2092 \leq p_{e'} \leq 2160$ MeV/c) and yellow box ($2010 \leq p_{e'} \leq 2108$ MeV/c), respectively.

photons for Λ and Σ^0 within these momentum regions were obtained to be $N_\gamma^\Lambda = 3.2 \times 10^{13}$ and $N_\gamma^\Sigma = 4.75 \times 10^{13}$ counts, respectively. The relative systematic error of the N_γ in the Λ and Σ^0 selections was 8.5%. This systematic error was mainly due to the systematic error of the acceptance (see Sec. 4.4.8).

■ **Number of the virtual photons in $nn\Lambda$ productions data**

In the case of the analysis for the $^3\mathrm{H}(e, e'K^+)X$ reaction, the integral range of the energy in Eq. 5.3 was defined same as the full momentum range of the HRS acceptance ($2.12 \leq p_{e'} \leq 2.32$ GeV/c). The number of the virtual photons in the ^{3}H runs was obtained to be $N_\gamma^\Lambda = 3.9 \times 10^{14}$ counts. The relative systematic error in the N_γ of ^{3}H run was also 8.5% same as one of the Λ and Σ^0.

5.1.2 Number of hyperon (Λ-QF)

The experiment took two types of productions data, the Λ and $nn\Lambda$ productions. The Λ and Σ^0 missing mass spectra were shown in Fig. 4.13. The number of the Λ and Σ^0 productions were to 1940 ± 180 and 440 ± 80 counts. These values were obtained by fitting with the function calculated by the convolution integral (see Sec. 4.2.7). On the other hand, the missing mass spectrum of the $^3\mathrm{H}(e, e'K^+)X$ reaction is shown in Fig. 5.2. There were any backgrounds such as

the Λ productions from the $p(e,e'K^+)\Lambda$ reaction, the Λ-QF productions from the $^3\mathrm{He}(e,e'K^+)X$ reaction, the π^+ background and the accidental background. The SIMC reproduced the missing mass spectrum in the $p(e,e'K^+)\Lambda$ reaction and Λ-QF distribution in the $^3_\Lambda$H reaction. The distribution of accidental background was given by mixed events analysis method (see Sec. 4.6.1). The yields of these backgrounds were discussed and were summarized in Tab. 4.10.

The number of the Λ-QF productions in the $^3\mathrm{H}(e,e'K^+)X$ reaction after removing any backgrounds was obtained at $2400 \pm 50(\mathrm{stat.}) \pm 160(\mathrm{syst.})$ counts.

5.1.3 Differential cross sections

Main parameters for the calculation of the differential cross sections were summarized in Tab. 5.1. The differential cross sections of the hyperons such as Λ and Σ^0 in the γ^*K^+ center-of-mass frame, were obtained by Eq. 5.1 at 334±9(stat.)±53(syst.) nb/sr and 83±4(stat.)±13(syst.) nb/sr, respectively. Moreover, the differential cross section of the Λ-QF productions in the $^3\mathrm{H}(e,e'K^+)X$ reaction was obtained at $880 \pm 20(\mathrm{stat.}) \pm 160(\mathrm{syst.})$ nb/sr.

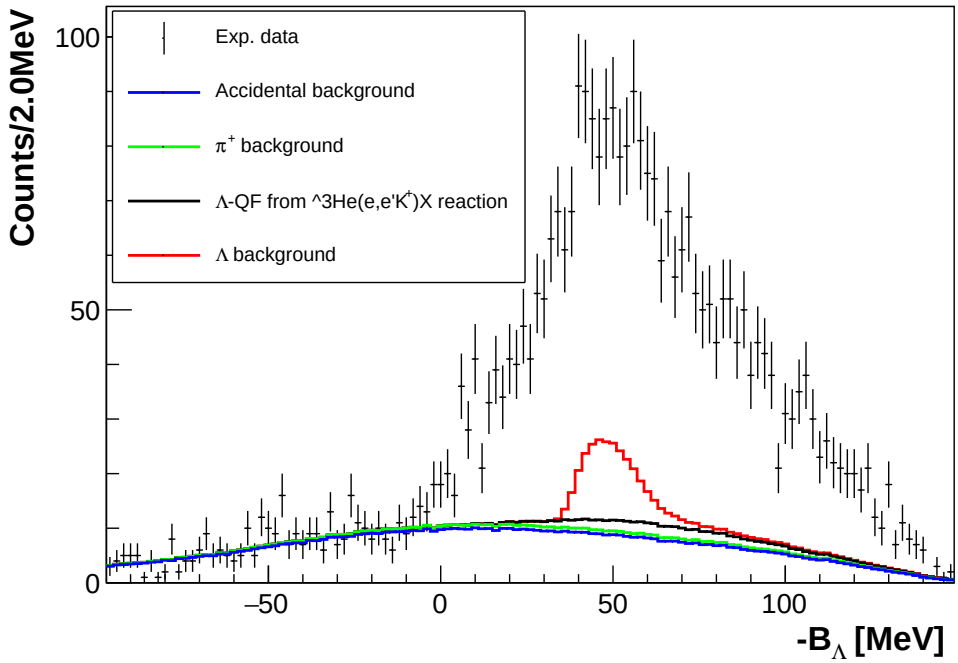

Figure 5.2: $^3\mathrm{H}(e,e'K^+)X$ missing mass spectrum. The dot points with error bars show the experimental data including any backgrounds. The three solid lines represent the spectra of the backgrounds (red: the Λ productions from the $p(e,e'K^+)\Lambda$ reaction, black: the $^3_\Lambda$H productions, green: the π^+e' coincidence events, blue: the accidental background).

Table 5.1: Main parameters for cross section calculation

Term	Target (hyperon)	Value	Relative systematic error [%]	Remark
N_T	T	1.70×10^{22}	0.4	Sec. 4.6.3 and 4.5.1
	H	4.2×10^{22}	0.2	Sec. 4.5.1
N_{γ^*}	T	3.90×10^{14}	8.5	Sec. 5.1.1
	H (Λ)	5.16×10^{13}	8.5	
	H (Σ^0)	5.54×10^{13}	8.5	
N_{HYP}	H (Λ)	1940	9.2	Sec. 4.2.7
	H (Σ^0)	870	18.0	
	T	2370	6.8	Sec. 5.1.2
$\varepsilon_{\mathrm{det}}$	H & T	0.536	5.0	Sec. 4.5
$\varepsilon_{\mathrm{decay}} \times \varepsilon_{\mathrm{absorp}}$ $d\Omega_K$	H & T	0.13 (p_K^{cent}) 5.5 mrad (p_K^{cent})	7.6	Sec. 4.4.7
$\left(\frac{\bar{d\sigma}}{d\Omega_K}\right)_{\mathrm{CM}}$ [nb/sr]	H (Λ)	334 ± 9(stat.)	16	Sec 5.1.3
	H (Σ^0)	83 ± 4(stat.)	16	
$\left(\frac{d\sigma}{d\Omega_K}\right)_{\mathrm{Lab}}$ [nb/sr]	T	880 ± 20(stat.)	18	Sec. 5.1.3

Table 5.2: Main kinematics parameters of $p(e, e'K^+)\Lambda/\Sigma^0$ measurement in this experiment

variable	central value	range
W [GeV]	2.12	$2.05 - 2.21$
Q^2 [(GeV/c^2)^2]	0.46	$0.31 - 0.61$
$\theta^{\mathrm{CM}}_{\gamma^* K}$ [degree]	8.4	$0 - 16$
ε	0.77	$0.74 - 0.80$

5.2 Discussion about elementary production

The experiment measured the missing mass spectra in $\mathrm{H}(e, e'K^+)\Lambda/\Sigma^0$ reactions, and these differential cross sections were obtained (see Table 5.1). The main kinematics settings of this experiment were summarized in Tab. 5.2. The parameters of W, Q^2, $\theta^{\mathrm{CM}}_{\gamma^* K}$ and ε were the total energy in the photon-nucleon system, the invariant mass of γ^*, the angle between γ^* and K^+ in center-of-mass frame. In this section, the differential cross sections of Λ obtained in this experiment will be compared with previous experimental data and theoretical calculations, and will discuss the $\theta^{\mathrm{CM}}_{\gamma K}$ and Q^2 dependence of the differential cross section of Λ.

5.2.1 Angular dependence

In this experiment, the Λ and Σ^0 productions were observed at the angle between γ^* and K^+ in the center-of-mass frame in a range of $0^\circ \leq \theta^{cm}_{\gamma K} \leq 16^\circ$. Fig. 5.3 shows the Λ differential cross sections of experimental data and theoretical calculations which used real photon beam. The red point at 8° was a result of the Λ differential cross section in this experiment. The solid and dashed red lines show the statistical and systematic errors, respectively. Comparing with

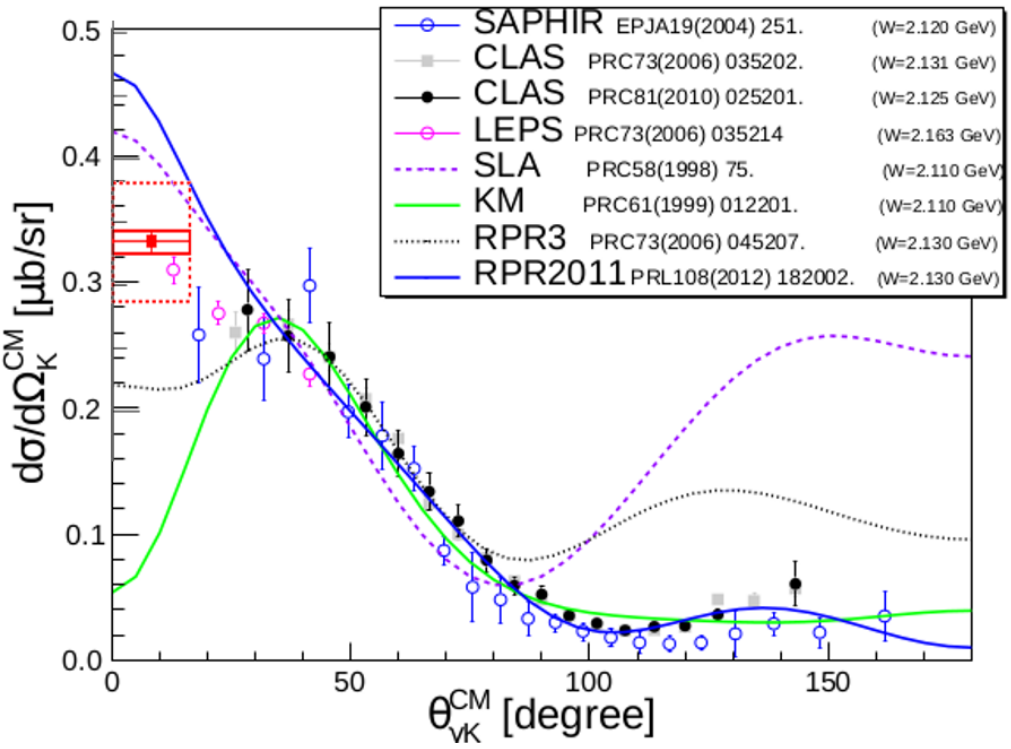

Figure 5.3: The angle ($\theta_{\gamma K}^{\rm CM}$) dependence on the differential cross section in the H$(e, e'K^+)\Lambda$ reaction. The result of the Λ differential cross section in this experiment was plotted with a red point at $\theta_{\gamma K}^{\rm CM} = 8°$. The solid and dot boxes around the data point represent the statistical and systematic errors, respectively. Other points were the results of other experiments with (γ, K^+) reactions [79–82], and each line shows the theoretical calculation of (γ, K^+) reactions [85–88].

theoretical calculations on the real photon reaction, the Λ differential cross section measured in this experiment was more agreement with RPR2011 and SLA than Kaon Maid and RPR3. However, the experiment measured Λ by using the virtual photon reaction ($\gamma^* + p \to \Lambda + K^+$). This reaction includes the longitudinally wave term so the result of this experiment was not exactly comparable with other theoretical calculations. However, on the condition at forward angle such as this experiment, the difference between virtual and real photons were small. Hence, the behavior of the differential cross section of Λ at forward angle in the real photon reaction was predicted from this experimental data.

5.2.2 Q^2 dependence

In the experiment, the differential cross section of the Λ in the $\gamma^* K^+$ reaction was measured in the region of $Q^2 = 0.46 \pm 0.15$ (GeV/c)^2.

Figure 5.4 shows the Q^2 dependence of the Λ differential cross sections. Each point with error in Fig. 5.4 represents the experimental results of the $p(\gamma^*, K^+)\Lambda$ reactions [84,89,90]. The three solid lines in Fig. 5.4 show the theoretical calculations in the (γ, K^+) reaction [86, 91, 92]. To compare the experimental results with different W, the scaling factor ($f(W)$) was defined as

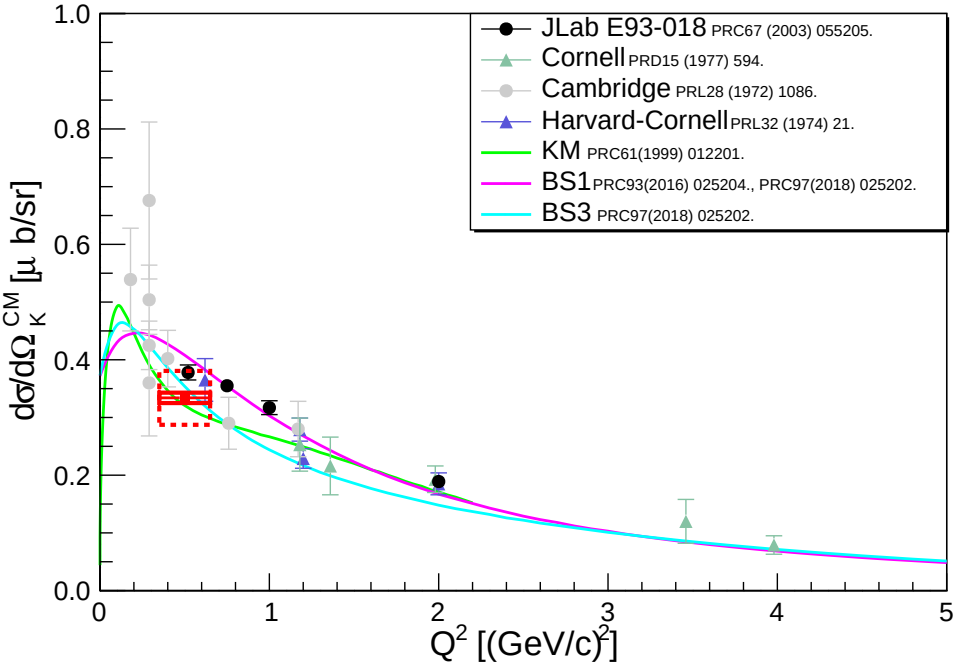

Figure 5.4: The Q^2 dependence on the differential cross section in the H$(e, e'K^+)\Lambda$ reaction. The result of the Λ differential cross section in this experiment was plotted with a red point at $\theta_{\gamma K}^{\rm CM} = 8°$. The other points shows the other experimental results which is scaled by using W correction factor $(f(W))$ in Eq. 5.4 [84, 89, 90]. The solid lines represents theoretical calculations in (γ, K^+) reaction [86, 91, 92].

following:

$$\frac{d\sigma}{d\Omega} \equiv f(W)|\mathcal{M}|^2, \tag{5.4}$$

$$f(W) = C_1 \frac{|\vec{p}_K^{\rm CM}|}{(W^2 - m_p^2)W} + C_2 \frac{A^2 B^2}{(W^2 - A^2)^2 + A^2 B^2}, \tag{5.5}$$

where $\mathcal{M}$ is the transition matrix element independent of W, and A, B, C_1, C_2 are the constant values. These constant values were obtained by fitting the W dependence of the Λ differential cross sections, as $A = 1.72$ GeV, $B = 0.10$ GeV, $C_1 = 4023.9$ $(\text{GeV})^2 \cdot \text{nb/sr}$, $C_2 = 180$ $(\text{GeV})^2 \cdot \text{nb/sr}$. Additionally, other experimental data were scaled to be $W = 2.15$ GeV [93].

This experimental result was in good agreement with the results of other experimental data and any theoretical calculations within the range of the systematic error.

5.3 $^3\mathrm{H}(e,e'K^+)X$ reaction

5.3.1 SIMC distribution in the $^3\mathrm{H}(e,e'K^+)X$ reaction

The differential cross section of the Λ-QF productions is obtained from Eq. 5.1. The scaling factor(f_{simc}) of the MC distribution was determined by fitting with the chi-square as,

$$\chi^2 = \sum_{i=a}^{N} \frac{(y^i_{\mathrm{exp}} - f_{\mathrm{simc}} \times y^i_{\mathrm{simc}})^2}{(\sigma^i)^2}, \tag{5.6}$$

where y^i_{exp} and y^i_{sim} are the differential cross section in each bin obtained by this experiment and the MC simulation. The value of σ^i in Eq. 5.6 is the statistical error in each bin. The fitting range was chosen to the region above 60 MeV where the FSI effect is small (see Sec. 5.5). Fig. 5.5 shows the missing mass spectrum with the $^3\mathrm{H}(e,e'K^+)X$ reaction subtracted any backgrounds. A horizontal axis shows Λ binding energy, and a vertical axis shows the differential cross section for the (γ^*, K^+) reaction which was defined in Eq. 5.1. The error bars in Fig. 5.5 shows statistical errors. The black line represents the the distribution of Λ-QF productions reproduced by the SIMC. This distribution took into account the Fermi momentum distribution of a proton in ^{3}H, and was scaled by Eq. 5.6.

The SIMC distribution was successful to be reproduced the experimental data over the 40 MeV region. Fig. 5.6 represents the energy dependence of the yield ratio for the experimental data to the SIMC calculation. This figure shows that the spectrum of SIMC did not reproduce the region bellow 20 MeV.

5.4 $nn\Lambda$ peak study

5.4.1 $nn\Lambda$ peak function

Figure 5.5 shows the differential cross section spectrum of the $^3\mathrm{H}(e,e'K^+)X$ reaction. The structure which was not reproduced by the MC spectrum existed around $-B_\Lambda \sim 0$ MeV in Fig. 5.5. However, the peak significance of this structure was not enough. The $nn\Lambda$ observed in this experiment was expected to be the large contribution of the radiation tail as seen in the Λ and Σ^0 peaks. Figure 5.7 shows the MC spectrum of $nn\Lambda$ in $(-B_\Lambda, \Gamma) = (0.0, 0.0)$ MeV generated by SIMC. Hence, the response function of $nn\Lambda$ was obtained by fitting the MC spectrum in Fig. 5.7 with the function defined in Eq.4.29. As a result of the fitting, the width of response function was obtained to be 4.32 MeV in FWHM. The three-body Jost function calculation predicts that $nn\Lambda$ exist as a resonance state with $(-B_\Lambda, \Gamma) = (0.55, 4.7)$ MeV [43]. Hence, the $nn\Lambda$ peak was represented by the function, which was calculated by the convolution integration of the Breit-Wigner assuming in $(-B_\Lambda, \Gamma) = (0.55, 4.7)$ MeV and the response function of $nn\Lambda$.

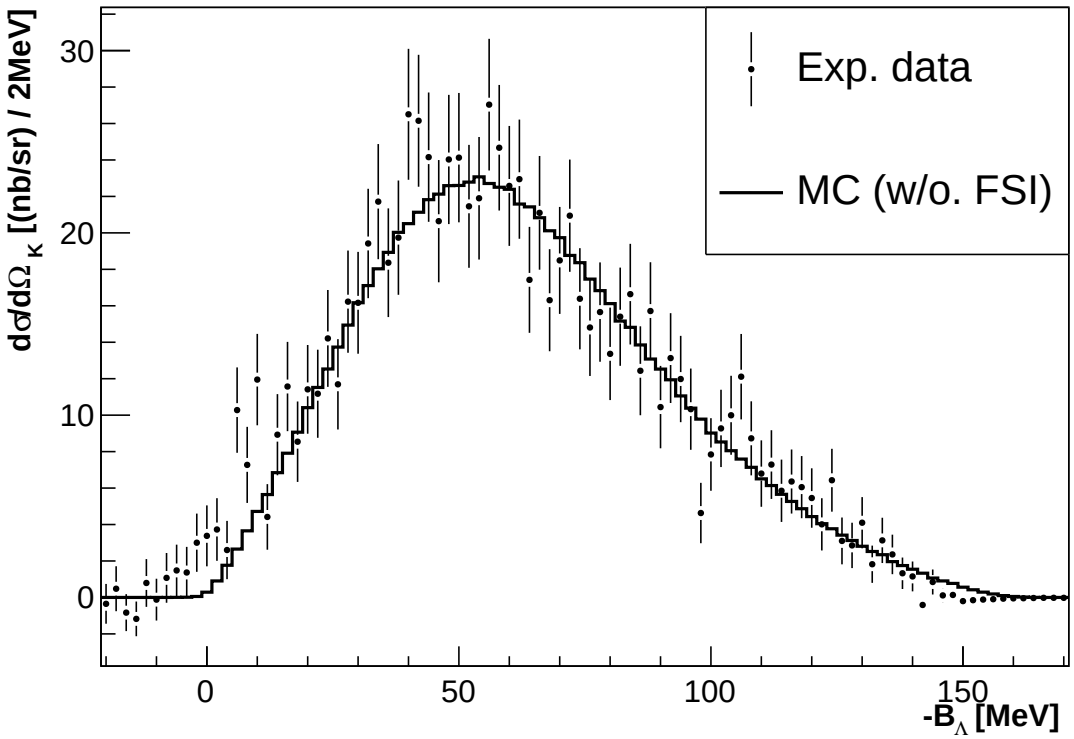

Figure 5.5: The differential cross section of $^3\mathrm{H}(e,e'K^+)X$ reaction as a function of Λ binding energy. The points with bar represent the experimental result, and the solid line shows the Λ-QF production spectra obtained by SIMC.

5.4.2 $nn\Lambda$ peak fitting

The only scaling factor of the $nn\Lambda$ function was set as a free parameter, while the parameters of $-B_\Lambda$ and Γ were fixed at 0.55 and 4.7 MeV where the theoretical calculation predicted the resonance state of $nn\Lambda$ [43]. As result of fitting the enhancement around $-B_\Lambda \sim 0$ MeV, the differential cross section of $nn\Lambda$ was obtained to be $21.7 \pm 6.7(\mathrm{stat.}) \pm 5.2\mathrm{syst.}$ (Fig. 5.8). However, the peak significance of this structure was small because of low statistics in this data. Hence, the upper limit of differential cross section about the structure around $-B_\Lambda \sim 0$ MeV was evaluated with a confidence level at 90% (90%CL).

The systematic error of 90%CL was estimated at the value where the ratio of the integral values for the differential cross section of $nn\Lambda$ above zero was 90% as a following:

$$\mathrm{C.L.90\%} : \frac{\int_0^x f(x)dx}{\int_0^\infty f(x)dx} = 0.9, \tag{5.7}$$

where $f(x)$ represented a Gaussian function. The variance value of the Gaussian function used the error which took into account of the systematic, the statistical and the fitting errors. Moreover, the mean value of the Gaussian function used the differential cross section of $nn\Lambda$. As

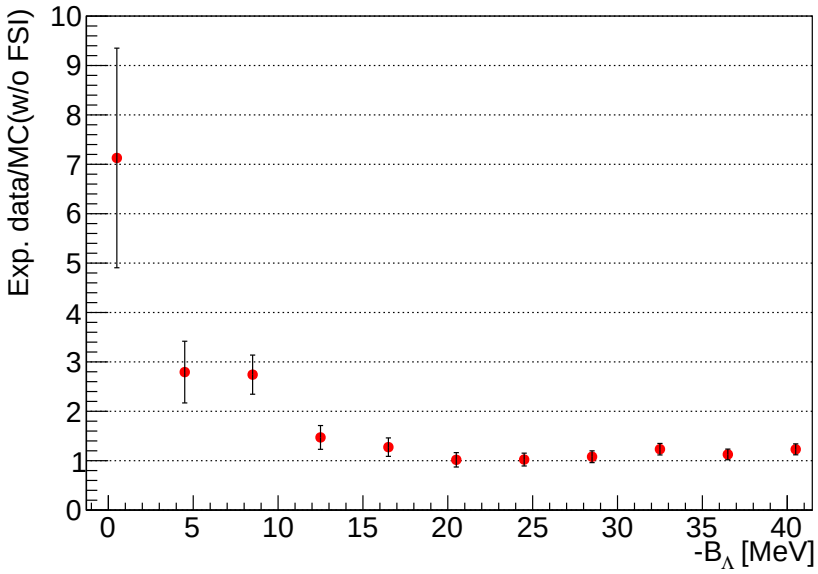

Figure 5.6: The energy dependence of the differential cross section ratio of the data and the SIMC calculation: The points represent the differential cross sections ratio of the data and the SIMC calculation.

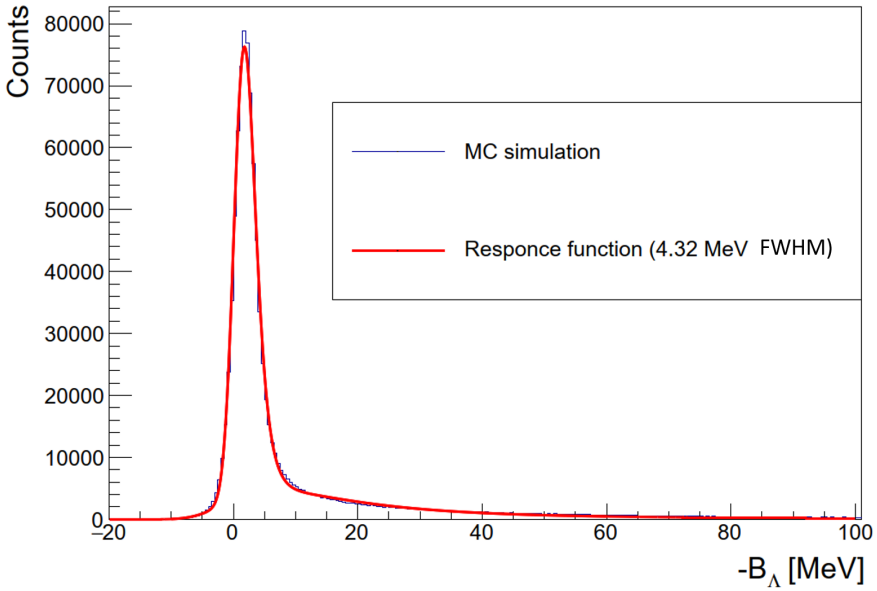

Figure 5.7: The blue solid line represents the $nn\Lambda$ spectrum given by SIMC. The red line is a fitting result with the convolution function defined in Eq. 4.29.

a result of the estimation for the upper limit of 90%CL with Eq. 5.7, the upper limit of 90%CL was obtained at 36.5 nb/sr assuming the $nn\Lambda$ peak at $(-B_\Lambda, \Gamma) = (0.55, 0.47)$ MeV.

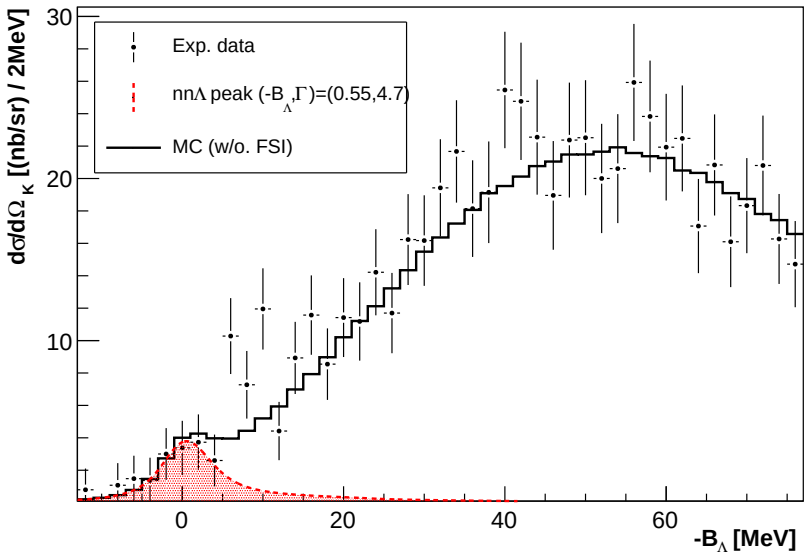

Figure 5.8: The fitting result of $nn\Lambda$ functions. The black dot points with bar are the spectrum of differential cross section after subtracting any backgrounds. The red hatched area represents the fitting function of $nn\Lambda$ defined in Eq.4.29 which was assuming $(-B_\Lambda, \Gamma) = (0.55, 4.7)$ MeV. The black solid line represents the total differential cross sections added the $nn\Lambda$ function and the Λ-QF spectrum given by SIMC.

5.5 Λn final state interaction

As a result of comparison between the experimental distribution and the Λ-QF spectrum with SIMC, There were two structures at $-B_\Lambda \sim 0$ MeV and $-B_\Lambda \sim 20$ MeV which cannot be reproduced by the spectrum obtained by SIMC. The structure at $-B_\Lambda \sim 0$ MeV may be considered as the $nn\Lambda$ state with $(-B_\Lambda, \Gamma) = (0.55, 4.7)$ MeV (Sec. 5.4). It is expected that the other structure at $-B_\Lambda \sim 20$ MeV is made by Λn final state interaction (FSI). Therefore, by comparing the structure in a range of $0 \leq -B_\Lambda \leq 40$ MeV with the MC spectrum of Λ-QF including Λn FSI, the Λn FSI effect is investigated.

5.5.1 Formalism

The Λn FSI can be treated as a two body scattering. Figure 5.9 shows a schematic drawing of the two body scattering in the $\gamma^* + t \to K^+ + (\Lambda nn)$ reaction. The matrix element(M_{fi}) for the elementary reaction $(\gamma^* + t \to K^+(nn) + \Lambda)$ is described as :

$$M_{fi} = \langle K^+ nn\Lambda | \, \mathbf{t}_{\gamma \mathbf{K}} \, | \gamma^* \mathrm{t} \rangle \,, \tag{5.8}$$

where $\mathbf{t}_{\gamma \mathbf{K}}$ is an transition operator. If there are no interactions between outgoing particles, the wave function of the final state was described with four plane waves($\langle K^+ nn\Lambda |$).

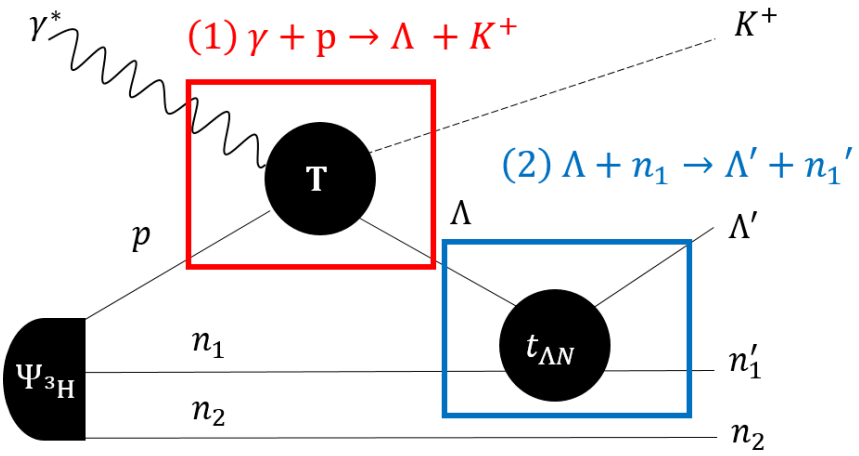

Figure 5.9: A Schematic drawing of the two body scattering in tritium

In the previous FSI study, the YN FSI in the three-body system is derived from a two-body scattering model [29]. In this model, a nucleon which is not involved the scattering reaction, is treated as independent of YN. Hence, the Λnn wave function is treated as :

$$|\Lambda n_1 n_2\rangle \rightarrow |\Lambda n_1\rangle |n_2\rangle . \tag{5.9}$$

The matrix element ($\tilde{M}_{fi}$) including the Λn scattering is written as follows :

$$\tilde{M}_{fi} = \langle n_2 K^+| \langle \Lambda' n_1| \mathbf{t_{\Lambda N}} |\Lambda n_1\rangle |n_2 K^+\rangle , \tag{5.10}$$
$$= \langle n_2 K^+| \langle \Lambda' n_1| \mathbf{t_{\Lambda N} t_{\gamma K}} |\gamma^* t\rangle , \tag{5.11}$$

where $t_{\Lambda N}$ is the transition matrix in the Λn scattering. Here, $\tilde{M}_{fi}$ is matrix parameters including the Λn FSI, and $\langle \Lambda n| |\Lambda' n\rangle$ is written by using Λn scattering wave function. The matrix elements including scattering amplitude with Λn FSI is

$$\tilde{M}_{fi} = \frac{\psi(kr+\delta)}{\psi(kr)} M_{fi}, \tag{5.12}$$

where $\psi(kr+\delta)$ and ψ are the wave function and phase shift parameters after the Λn scattering, and $\psi(kr)$ is the wave function without Λn FSI. Therefore, the correlation between differential cross section with FSI and without FSI is described as :

$$\left(\frac{d\sigma}{d\Omega}\right)_{\text{FSI}} = f_{P.S.} |\tilde{M}_{fi}|^2 = |\frac{\psi(kr+\delta)}{\psi(kr)}|^2 \left(\frac{d\sigma}{d\Omega}\right), \tag{5.13}$$

where $f_{P.S.}$ is a phase space factor. The influence (I) which is defined the ratio of the cross sections with and without FSI, from the Λn FSI on the $^3\text{H}(e, e'K^+)\Lambda nn$ is written as

$$I = |\frac{\psi(kr+\delta)}{\psi(kr)}|^2. \tag{5.14}$$

5.5.2 Jost function

Basically, the Λn FSI can be described by the squared scattering amplitude I (see Fig. 5.14). The scattering amplitude was obtained by Lippmann-Schwinger equation with a Λn potential. In the effective range approximation (ERA) [100], the enhancement factor can be reproduced as:

$$I = \frac{1}{|J_l(k_{rel})|^2}, \tag{5.15}$$

where J_l is Jost function with the lth partial wave, and k_{rel} is the relative momentum between Λ and a neutron. Λn FSI is dominant in a low energy region so the s-wave part ($l = 0$) is taken into account. The s-wave Jost function is written as

$$J_{l=0}(k_{rel}) = \frac{k_{rel} - i\beta}{k_{rel} - i\alpha}, \tag{5.16}$$

where α and β are described from scattering length (a) and effective range (r_e) of a Λn potential as

$$\frac{1}{2}r_e(\alpha - \beta) = 1, \quad \frac{1}{2}r_e\alpha\beta = -\frac{1}{a}. \tag{5.17}$$

From Eq. 5.15-5.17, The influence factor can be written with only two potential parameters (a and r_e) which are summarized in Tab. 5.3. In the two baryon scattering, the total spin state is composed of four states, a singlet ($\{\uparrow\downarrow - \downarrow\uparrow\}/\sqrt{2}$) and three triplet ($\uparrow\uparrow$, $\downarrow\downarrow$, $\{\uparrow\downarrow + \downarrow\uparrow\}/\sqrt{2}$) states. Figure 5.10 shows Influence factors (I) with NSC97f potential parameters (see Table 5.3).

Λn has four spin states, one singlet state and three triplet states, so the Λn influence factor is composed of $(I_s + 3I_t)/4$ by weighting the four possible states equally. Figure 5.11 shows Influence factor calculation for two different Λn potential models.

5.5.3 Relative momentum between Λ and a neutron

The differential cross section with FSI can be calculated with influence factor (I) as a function of the relative momentum between Λ and a neutron in tritium.

■ Calculation of a Λ momentum

On an elementally reaction approximation, the momentum of the recoil Λ was obtained by the conservation equation of the energy and momentum as :

$$\vec{p}_\Lambda = \vec{p}_p + \vec{p}_{\gamma^*} - \vec{p}_K, \tag{5.18}$$
$$E_\Lambda = E_p + E_{\gamma^*} - E_K, \tag{5.19}$$

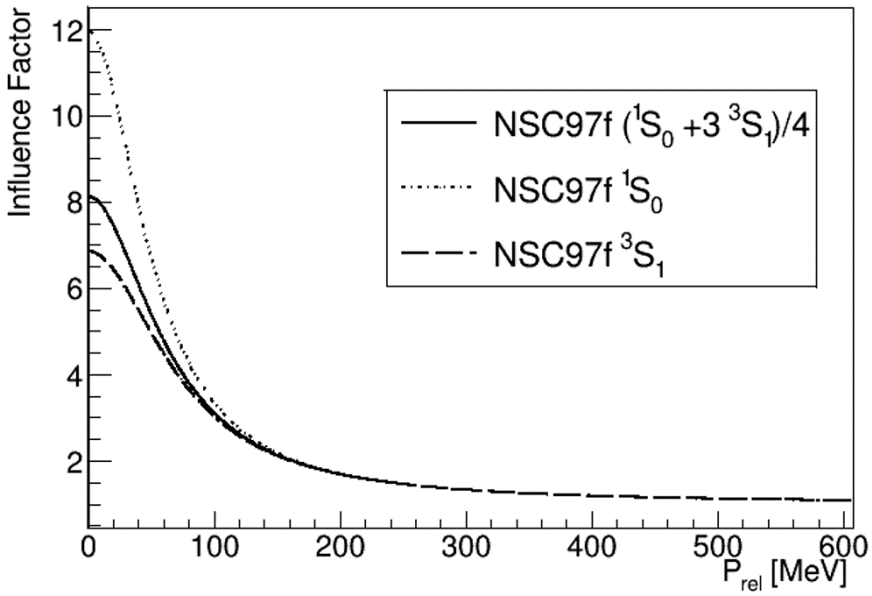

Figure 5.10: Influence factors: The dot, dot-dashed and solid lines represent the influence factors when Λn spin states were singlet, triple and mixing, respectively.

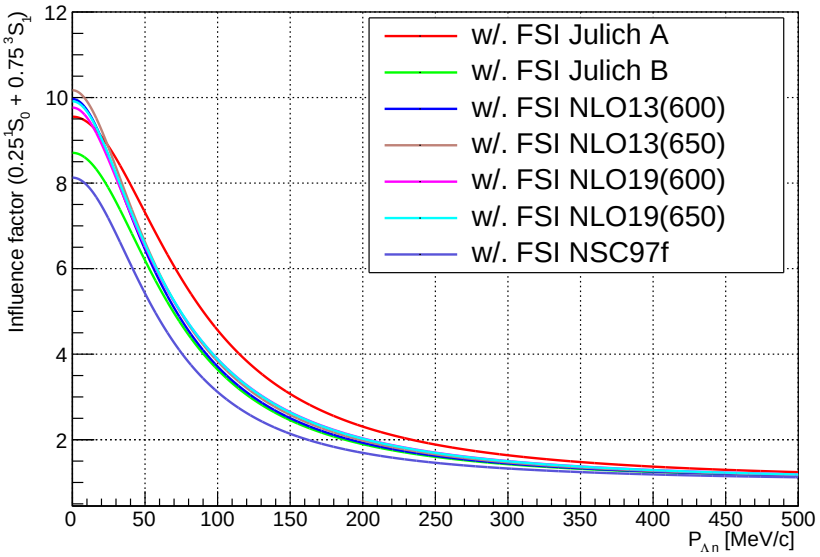

Figure 5.11: Influence factors($I = (I_s + 3I_t)/4$) for the seven different Λn potential models.

where momenta of $\vec{p}_{\gamma^*}$ and $\vec{p}_K$ are measurement values in the HRSs and CEBAF.

The proton momentum value $|\vec{p}_p|$ is determined probablistically from the Fermi momentum distribution. However, a direction of proton momentum should be given by hands. In the study, the direction was assigned by randomly following the spherical uniform distribution in the Lab frame in the event by event basis.

Table 5.3: The main parameters of various Λn potentials [96–99].

Model	state	a (fm)	r (fm)	reference
Julich A	Singlet ($^1S_0$)	-1.60	1.33	[96]
	Triplet ($^3S_1$)	-1.60	3.15	
Julich B	Singlet ($^1S_0$)	-0.57	7.65	[96]
	Triplet ($^3S_1$)	-1.94	2.42	
NSC97f	Singlet ($^1S_0$)	-2.68	3.07	[97]
	Triplet ($^3S_1$)	-1.67	3.34	
NLO13(600)	Singlet ($^1S_0$)	-3.291	2.71	[98, 99]
	Triplet ($^3S_1$)	-1.487	2.72	
NLO13(650)	Singlet ($^1S_0$)	-3.271	2.61	[98, 99]
	Triplet ($^3S_1$)	-1.452	2.64	
NLO19(600)	Singlet ($^1S_0$)	-3.227	2.74	[98, 99]
	Triplet ($^3S_1$)	-1.362	2.51	
NLO19(650)	Singlet ($^1S_0$)	-3.225	2.62	[98, 99]
	Triplet ($^3S_1$)	-1.365	2.56	

■ **Calculation of a neutron momentum in ^{3}H system**

Since the ^{3}H target was stopped, the momenta of nucleons in a ^{3}H nucleus were given by :

$$\vec{k}_{n1} + \vec{k}_{n2} + \vec{p}_p = 0 \ . \tag{5.20}$$

The relative momentum ($\vec{k}_{rel}$) between neutrons in the ^{3}H nucleus is defined as :

$$\vec{k}_{\rm rel} = \frac{M_{n2}\vec{k}_{n1} - M_{n1}\vec{k}_{n2}}{M_{n1} + M_{n2}} \ , \tag{5.21}$$

$$= \frac{\vec{k}_{n1} - \vec{k}_{n2}}{2} \ . \tag{5.22}$$

Therefore, each of the neutron momentum ($\vec{k}_{n1(n2)}$) in the ^{3}H nucleus is written with Eq. 5.20 and 5.22 as :

$$\vec{k}_{n1(n2)} = -\frac{1}{2}\vec{p}_p \pm \vec{k}_{rel} \ , \tag{5.23}$$

$$|\vec{k}_{n1(n2)}| = \sqrt{\vec{k}_{\rm rel}^2 + \frac{\vec{k}_p^2}{4} \pm |\vec{k}_{\rm rel}||\vec{k}_p|\cos\theta} \ , \tag{5.24}$$

where the $\cos\theta$ is the angle between $\vec{k}_{\rm rel}$ and $\vec{k}_p$.

■ **Spectral function (SF)**

The momentum of each neutron was obtained from Eq. 5.24. However, there are two free parameters, the relative momentum and the angle θ between $\vec{k}_{rel}$ and $\vec{k}_p$. The angle was given by generating with the spherical uniform in the Lab coordinate. The relative momentum can be obtained by introducing the spectral function (Sec. 4.4.5). In this study, a neutron momentum was treated as the proton description in the ^{3}H spectral function frame because of the relationship about mirror nuclei between a neutron in ^{3}H and a proton in ^{3}He. The absolute value of the

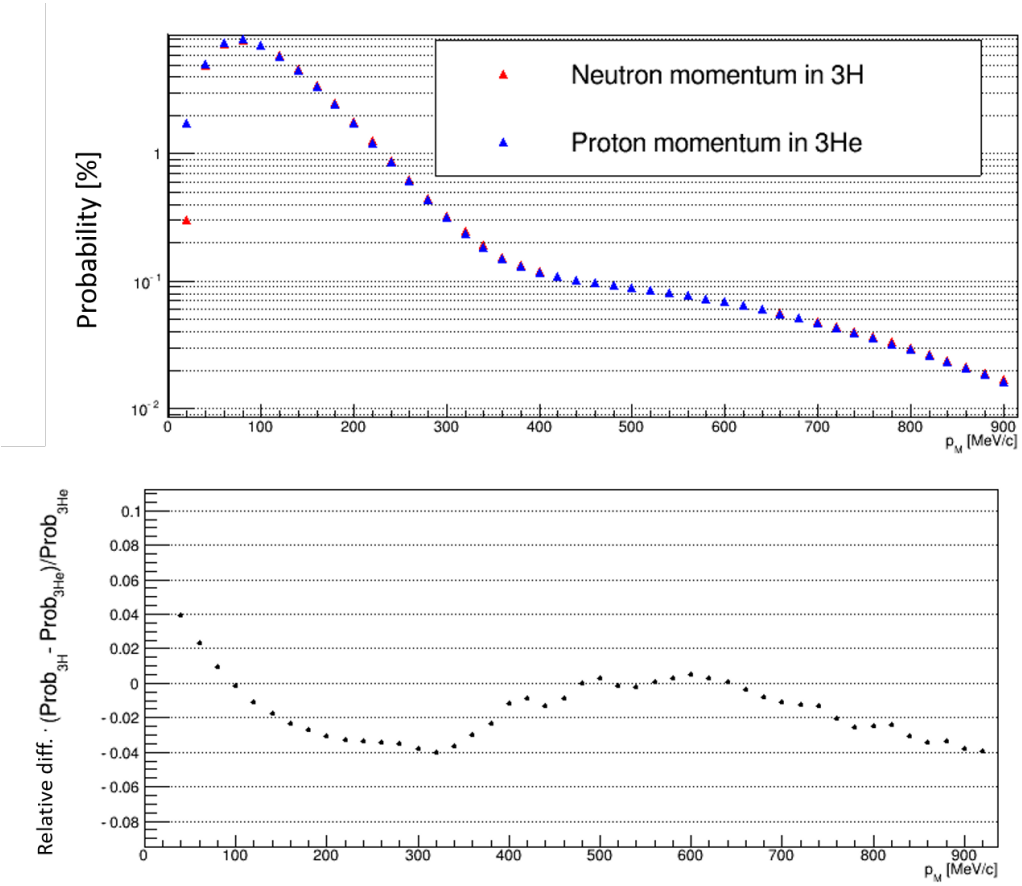

Figure 5.12: The top figure shows the momentum probabilities of one of a nucleon in ^{3}H, ^{3}He [69]. The bottom figure shows the relative difference between momentum probabilities ^{3}H and ^{3}He.

relative momentum ($|\vec{k}_{\rm rel}|$) can be calculated using the given value of E_m as follows :

$$|\vec{k}_{\rm rel}| = (2M_n)E^*_{nn} = 2M_n\sqrt{E_m - |E_{\rm T}| + |E_{nn}|}, \tag{5.25}$$

where E_{nn} and $E_{\rm T}$ are binding energies of the residual system ($E_{nn} = 0$ MeV) and the tritium ($E_{\rm T} = 8.48$ MeV).

However, the theoretical calculation of the ^{3}H SF was old [70] and difficult to confirm. On an assumption of the charge symmetry, the neutron momentum in ^{3}H can be treated as equivalent to the proton momentum in ^{3}H. The proton momentum in ^{3}He was obtained from Eq. 5.25 with $E^*_{pp} = 0$ MeV, and $E_{\rm 3He} = (M_{\rm 2H} + M_p - M_{\rm 3He})c^2 = 4.99$ MeV. The E_m in ^{3}He was estimated from the ^{3}He SF [71]. Figure 5.12 shows the momentum distributions of the a proton in ^{3}He and nucleon in ^{3}H [69]. The relative difference of momentum probabilities between the proton in ^{3}He and neutron in ^{3}H was less than 5% in each momentum point.

As a result of the calculation about the neutron momentum in ^{3}H with ^{3}He SF, the neutron momentum probability in ^{3}H was shown in Fig. 5.13.

The direction of relative momentum between neutrons $\hat{\vec{k}}_{rel}$ was randomly generated uniformly on the sphere in the Lab frame, and the $\vec{k}_{rel}$ and each of a neutron momentum $\vec{k}_{n1(n2)}$ was

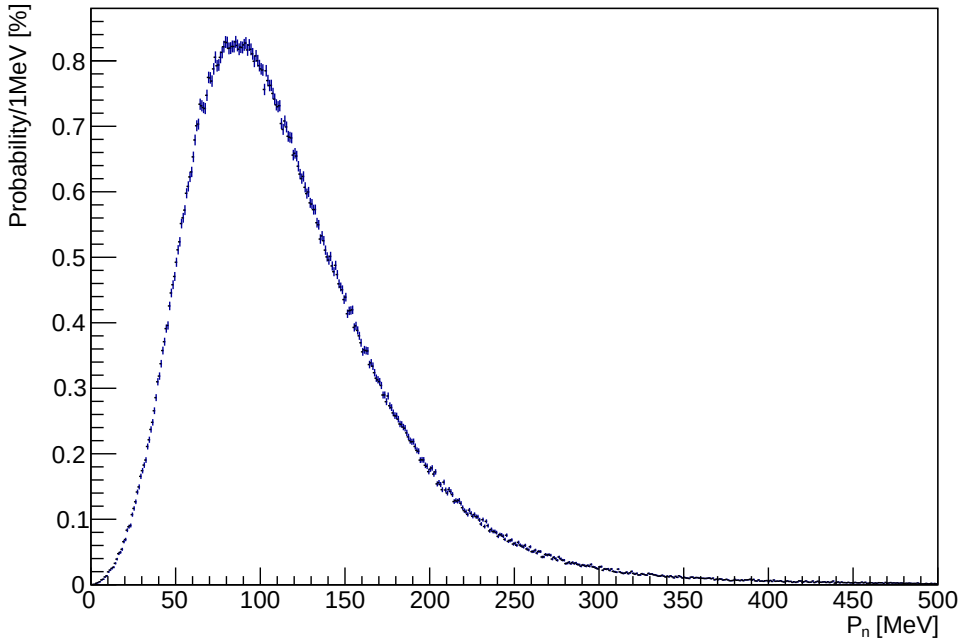

Figure 5.13: Neutron momentum distribution in ^{3}H

obtained from Eq. 5.22.

5.5.4 Scaling of the MC spectra with FSI

The differential cross section including FSI was obtained by multiplying the differential cross section without FSI by the influence factor (I) (see Sec. 5.5.2). In this study, the influence factor was calculated by using the Jost function with the effective range approximation (ERA) (Eq. 5.15-5.17), and the variable of influence factor such as a Λn relative momentum was estimated event by events with the neutron momentum (see Sec.5.5.3). The differential cross section ratio with and without FSI is shown in Fig. 5.15.

The scattering cross section due to the FSI effect is large in the low region of the Λn relative momentum , and the differential cross section ratio with and without FSI has a maximum value at $-B_\Lambda \sim 0$ MeV (Fig. 5.11). In the high energy region $-B_\Lambda \geq 100$ MeV, the Λn relative momentum becomes large and the influence factor is expected to be $I \to 1$ (Fig.5.11). However, for all potential models, the differential cross section ratios are always larger than 1 in high energy region ($-B_\Lambda \geq 100$ MeV). This is because the influence factor calculated from Eq. 5.15 and 5.16 assumes ERA which is the low momentum approximation. Therefore, the scaling factor

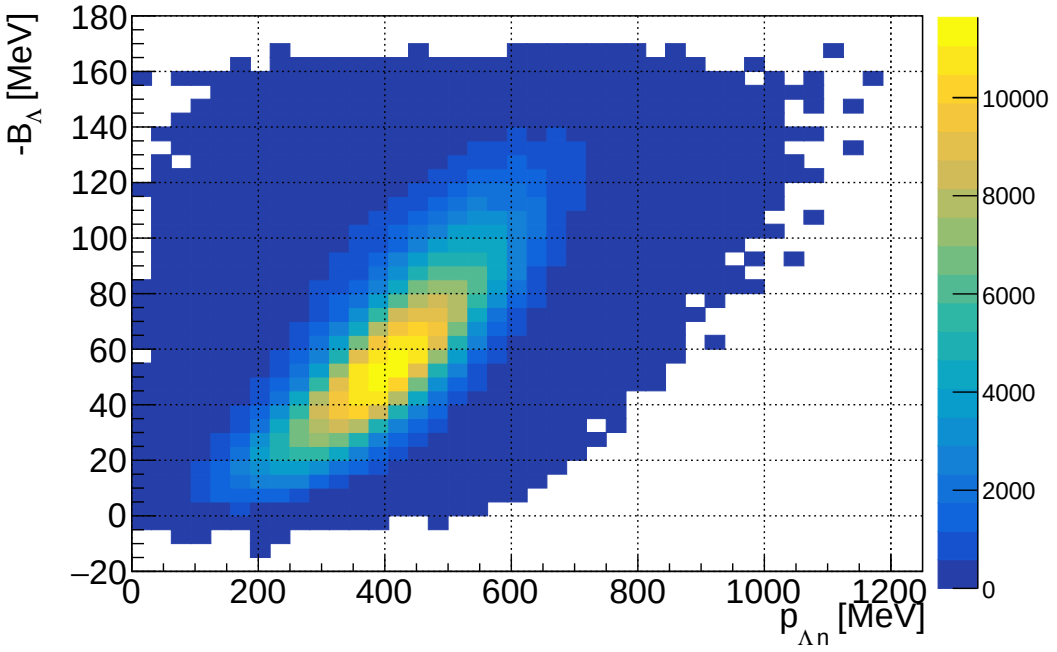

Figure 5.14: Λn relative momentum distribution. The relative momentum between Λ and one of the neutron in ^{3}H was calculated by Eq. 5.25.

pf FSI $f_{\rm FSI}$ was introduced, and the differential cross section with FSI was written by:

$$\left(\frac{d\sigma}{d\Omega}\right)_{\rm FSI} = I \times f_{\rm FSI} \times \left(\frac{d\sigma}{d\Omega}\right)_{\rm w/oFSI}, \tag{5.26}$$

$$= w_{\rm FSI} \times \left(\frac{d\sigma}{d\Omega}\right)_{\rm w/oFSI}. \tag{5.27}$$

The FSI scaling factor was determined by the minimizing chi-square defined in Eq. 5.6 in each potential model. By introducing a weighting factor defined as $w_{\rm FSI} = I \times f_{\rm FSI}$, the Λn FSI effect can be written as the $w_{\rm FSI}$ instead of the influence factor. The weighting factor was determined by the chi-square minimization defined as Eq. 5.6 in the range of ($60 \leq -B_\Lambda$ MeV) where the FSI effect was small.

Figure 5.16 shows the differential cross section of the ^{3}H(e, e′K$^+$)X reaction and the MC spectra without and with FSI.

5.5.5 Potential dependence of FSI

Comparing the MC spectra without and with FSI, the MC spectra with FSI made enhancements in the $0 \leq -B_\Lambda \leq 60$ MeV region for all of Λn potentials (Tab. 5.3). However, these spectra did not reproduce experimental data within the range of $0 \leq -B_\Lambda \leq 10$ MeV. The structure near $-B_\Lambda \sim 0$ MeV might be due to the $nn\Lambda$ peak. Therefore, the study of the Λn FSI was evaluate with two cases, ranges of $20 \leq -B_\Lambda \leq 60$ MeV without the $nn\Lambda$ peak and

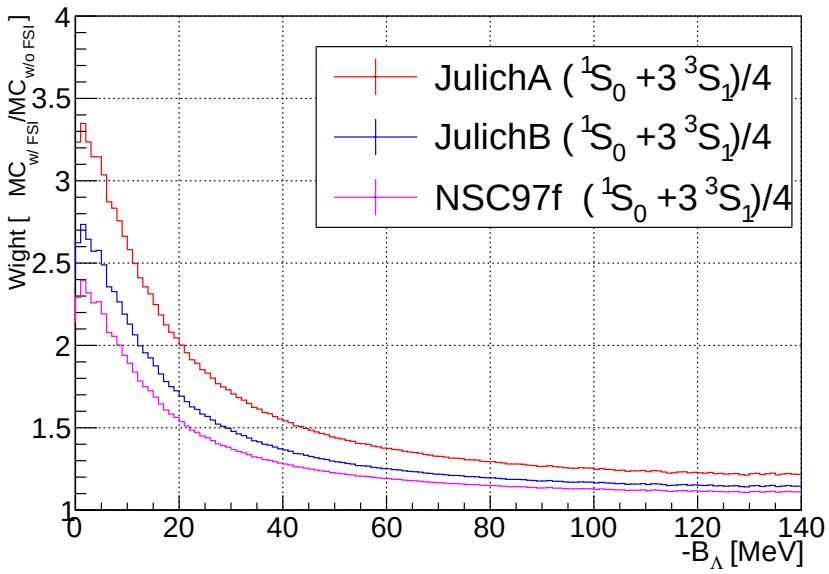

Figure 5.15: Enhancement distributions in each FSI potentials. The enhancement distributions were calculated by Eq. 5.14 and scaled by dividing differential cross section of without FSI. These spectra has enhancement over 100 MeV energy region where the effect of FSI is negligible.

$0 \leq -B_\Lambda \leq 60$ MeV with the $nn\Lambda$ peak.

■ **FSI spectrum without $nn\Lambda$ function ($20 \leq -B_\Lambda \leq 60$ MeV)**

In the region of $20 \leq -B_\Lambda \leq 60$ MeV, the leakage of the $nn\Lambda$ peak is small and negligible. To compare the experimental data with the MC spectra with FSI, the chi-square was defined as follows:

$$\chi^2 = \sum_{i=a}^{N} \frac{(y^i_{\rm exp} - y^i_{\rm FSI})^2}{{\sigma^i_{\rm exp}}^2}, \tag{5.28}$$

where $y^i_{\rm exp}$, $y^i_{\rm FSI}$ and $\sigma^i_{\rm exp}$ were the experimental data, the differential cross section with the FSI obtained by the SIMC, and the systematic error of the differential cross section for each bin within a range of $20 \leq -B_\Lambda \leq 60$ MeV, respectively. Table 5.4 shows the reduced chi-square values obtained by fitting the experimental data with the MC spectra including Λn each FSI model. The Λn FSI with NSC97f potential has the value of chi-square at 0.85, which has the smallest reduced chi-square among seven potential models and without FSI model. However, the differences in the reduced chi-square among seven potential models and without FSI model were small, and the statistics was not sufficient in this experiment to determine the Λn potentials.

■ **FSI spectrum with $nn\Lambda$ function ($0 \leq -B_\Lambda \leq 60$ MeV)**

The FSI made the enhancement within a range of $0 \leq -B_\Lambda \leq 60$ MeV. However, the structure near the $-B_\Lambda \sim 0$ MeV might be due to the $nn\Lambda$ state. Hence, the $nn\Lambda$ peak function with

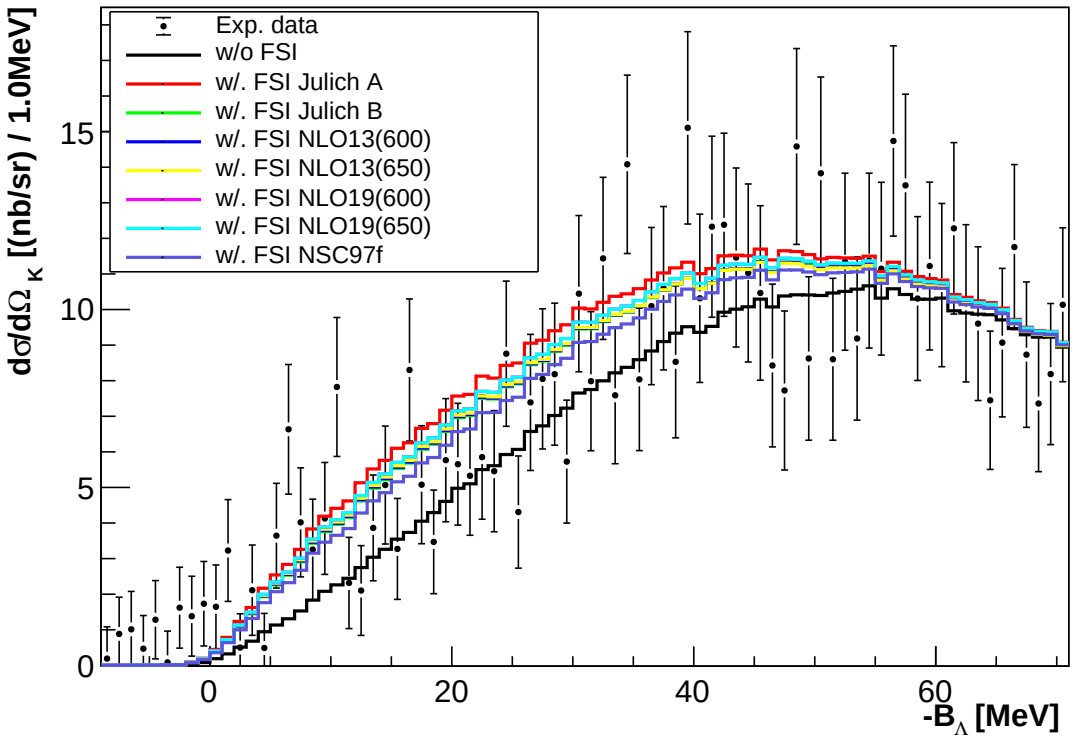

Figure 5.16: The black dot points shows the differential cross section of Λ-QF production. The three lines such as black, red and blue represents the MC spectra without FSI, with FSI (blue line: Jülich A, red line: NSC97f).

Table 5.4: Reduced chi-square values (χ^2/ndf) obtained by fitting the experimental data ($20 \leq -B_\Lambda \leq 60$ MeV) with the MC spectra including each Λn FSI model

Λn Potential	Reduced chi-square (χ^2/ndf)
w/o FSI	0.86
Jülich A	1.06
Jülich B	0.90
NSC97f	0.85
NLO13(600)	0.91
NLO13(650)	0.93
NLO19(600)	0.96
NLO19(650)	0.96

$(-B_\Lambda, \Gamma) = (0.55, 4.7)$ MeV was introduced into the MC spectrum with FSI, and the scaling factor of the $nn\Lambda$ peak function ($w_{nn\Lambda}$) was determined by minimizing the chi-square defined as following:

$$\chi^2 = \sum_{i=a}^{N} \frac{(y^i_{\rm exp} - y^i_{\rm FSI} - w_{nn\Lambda} \times y^i_{\rm nnL})^2}{(\sigma^i_{\rm exp})^2}, \tag{5.29}$$

where $y^i_{\rm FSI}$ is the differential cross section with the FSI obtained by the SIMC, which scaled with $w_{\rm FSI}$ (Eq. 5.27). The results of fitting were shown in Fig. 5.17. Moreover, Fig. 5.18 shows the MC spectra with and without FSI considering the $nn\Lambda$ peak when chi-squares in Eq. 5.29

Table 5.5: Reduced chi-square values (χ^2/ndf) obtained by fitting the experimental data ($0 \leq -B_\Lambda \leq 60$ MeV) with the MC spectra including each Λn FSI model

Λn Potential	Reduced chi-square (χ^2/ndf)	$nn\Lambda$ peak [nb/sr]
w/o FSI (w/o nnL peak)	1.24	0.0
w/o FSI	1.09	23.0
Jülich A	1.40	1.1
Jülich B	1.15	5.5
NSC97f	1.05	8.0
NLO13(600)	1.16	5.1
NLO13(650)	1.17	4.7
NLO19(600)	1.22	4.0
NLO19(650)	1.22	4.0

take the minimum values. The results of reduced chi-square minimization defined in Eq. 5.29 are summarized in Tab. 5.5. In case of the MC spectrum with the NSC97f potential, the chi-square took the the minimum value at 1.05 among other Λn potentials when the differential cross section of the $nn\Lambda$ peak was 8.0 nb/sr. However, since the difference in chi-square between the Λn potentials listed in tab. 5.5 is small, the present experiment did not prefer any particular Λn potential model from them.

5.5.6 Search for best Λn potential parameters

The differential cross section including the FSI was obtained by calculating the influence factor. The influence factor was calculated by using potential parameters such as the scattering length (a) and effective range (r) with Eq. 5.15 - 5.17. Therefore, the influence factor for each (a, r) point was calculated in order to search for the best fit parameters and give a limit to each potential parameter (a, r).

■ **Chi-square of Λn FSI ($20 \leq -B_\Lambda \leq 60$ MeV)**

In Fig. 5.5, there were two structures, near the $nn\Lambda$ threshold ($-B_\Lambda \sim 0$ MeV) and the region of $-B_\Lambda \sim 10$ MeV. However, the Λn FSI made an smooth enhancement from 0 to 60 MeV, and was not reproduced two structures less than 20 MeV. Hence, the (a, r) dependence of the chi-square (Eq. 5.28) was studied within a range of $20 \leq -B_\Lambda \leq 60$ MeV. Figure 5.19 shows the chi-square distribution within the range of $20 \leq -B_\Lambda \leq 60$ MeV. The magenta color point shows $(a, r) = (-0.67, 5.2)$ fm where chi-square is minimized ($\chi^2 = 31.1, \mathrm{ndf} = 40$). The black solid, dashed and dashed-dot lines show the contour lines of chi-squares at 32.1, 33.1 and 34.1, respectively. The black solid lines represent the fitting errors (σ) of (a, r). Therefore, the 1σ upper and lower limits of the effective range can be obtained from the black solid lines in Fig. 5.19. When the scattering length (a) is -0.67 fm, the effective range was obtained at $5.2^{+3.2}_{-1.3}$(stat.) fm. On the other hand, the chi-squares were almost constant with respect to the

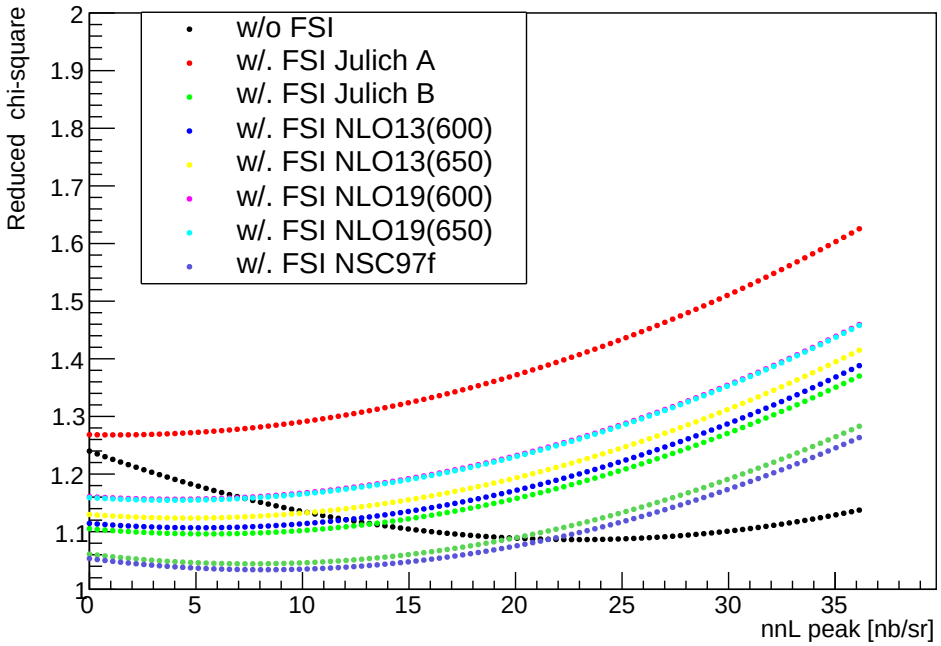

Figure 5.17: The reduced chi-square distributions depending on $nn\Lambda$ differential cross section in each potential model.

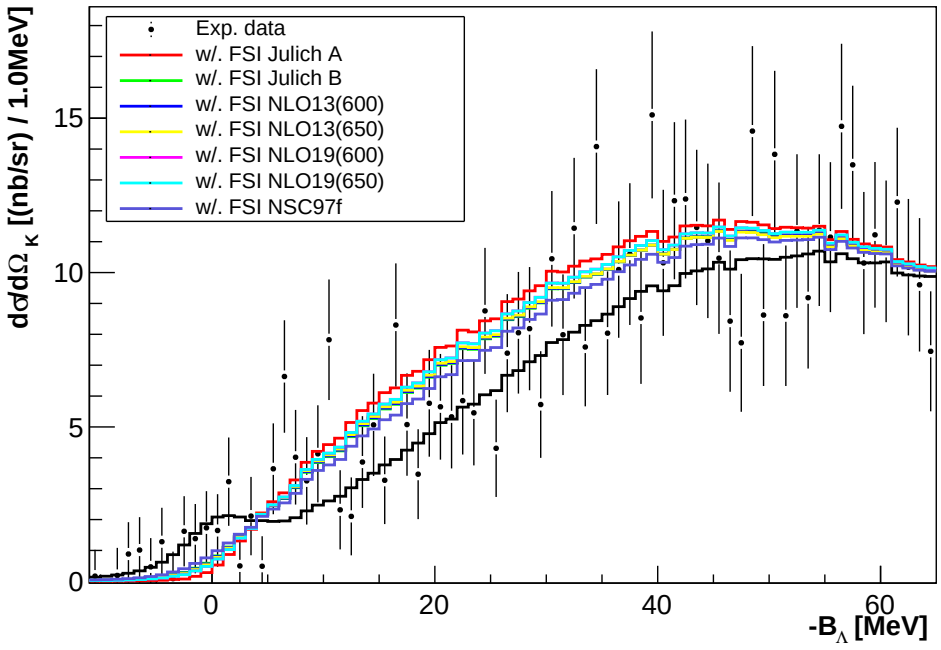

Figure 5.18: The $nn\Lambda$ peak functions and MC spectra with three different Λn FSI after scaled $nn\Lambda$ peak function by chi-square minimization. The differential cross section of nnL in each Λn potential was determined by the chi-square minimization (tab. 5.5).

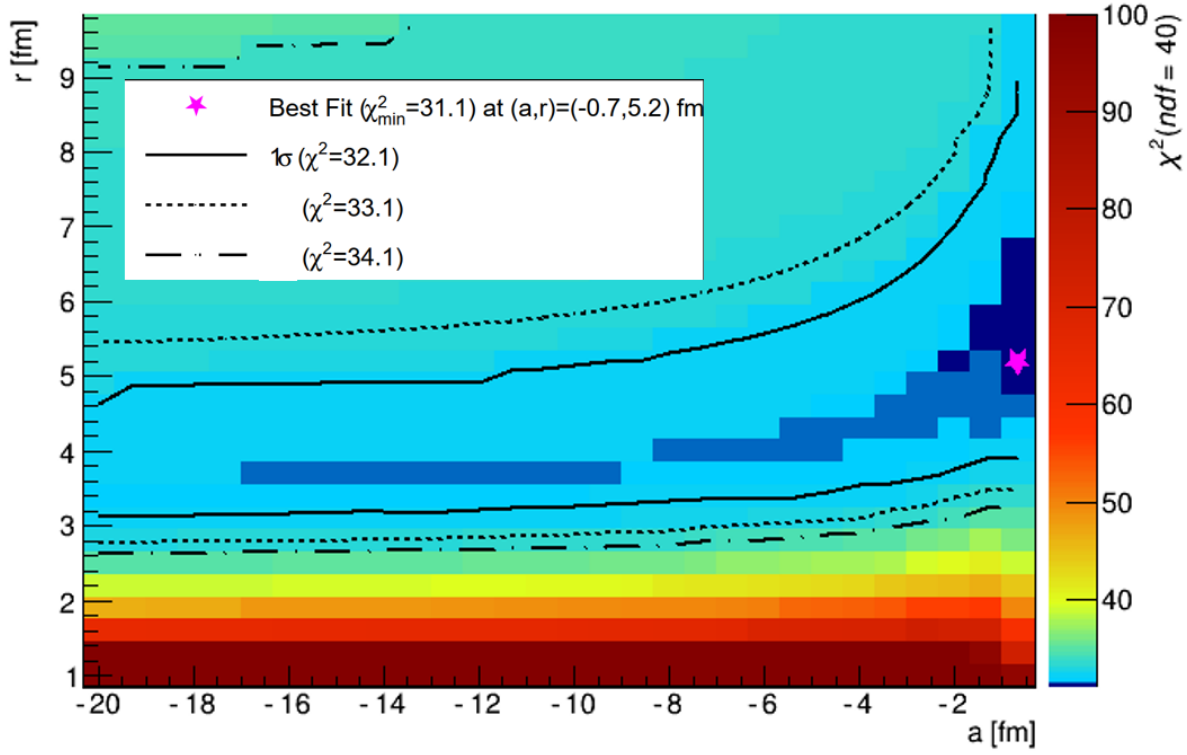

Figure 5.19: Chi-square distributions within a range of $20 \leq -B_\Lambda \leq 60$ MeV: The minimum chi-square is obtained as 31.1 at $(a, r) = (-0.67, 5.2)$ (magenta point). The black solid, dashed and dashed-dot lines show the contour line of chi-square at 32.1, 33.1 and 34.1, respectively.

scattering length so the upper and lower limit of the scattering length could not obtained from Fig. 5.19.

■ **Chi-square of Λn FSI with $nn\Lambda$ peak ($0 \leq -B_\Lambda \leq 60$ MeV)**

In addition, the (a, r) dependence of the chi-square within the range of $0 \leq -B_\Lambda \leq 60$ MeV was studied. The distribution of chi-square defined in Eq. 5.28 and the differential cross section of the $nn\Lambda$ peak when (a, r) parameters were varied, are shown in Fig. 5.20 and Fig. 5.21, respectively. The black solid, dashed and dashed-dot lines show the contour lines of the chi-squares at 60.0, 61.0 and 62.0, respectively. Additionally, when the scattering length and effective range are at -2.6 and 5.0 fm, the chi-square has minimum value at 59.0, and weighting factor distribution with $(a, r) = (-2.6, 5.0)$ fm is shown a red line in Fig. 5.22. The amplitude of the weighting factor with $(a, r) = (-2.6, 5.0)$ fm is smaller than one of theoretical models. The black solid lines represent the fitting errors (σ) of (a, r). When the scattering length (a) was assumed as -2.6 fm, the effective range was obtained as $r = 5.0^{+1.3}_{-1.2}$(stat.) fm.

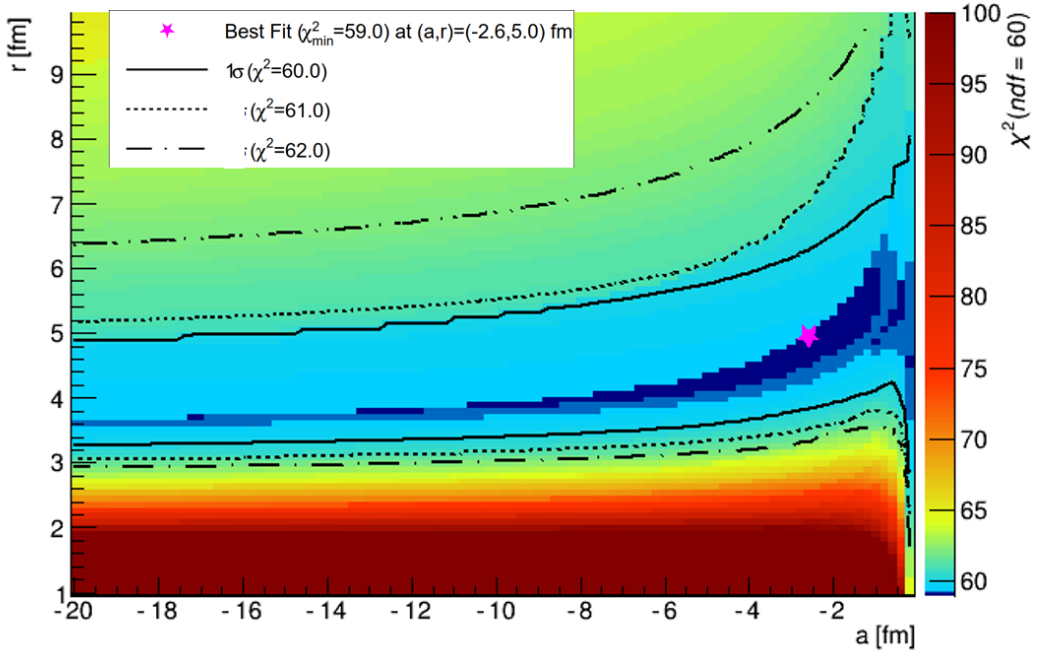

Figure 5.20: Chi-square distributions within a range of $0 \leq -B_\Lambda \leq 60$ MeV. The z-vertex shows the chi-square defined in Eq. 5.28. The magenta point is $(a, r) = (-2.6, 5.0)$ where chi-square was minimum at 59.0. The black solid, dashed and dashed-dot lines show the contour line of chi-square at 60.0, 61.0 and 62.0, respectively.

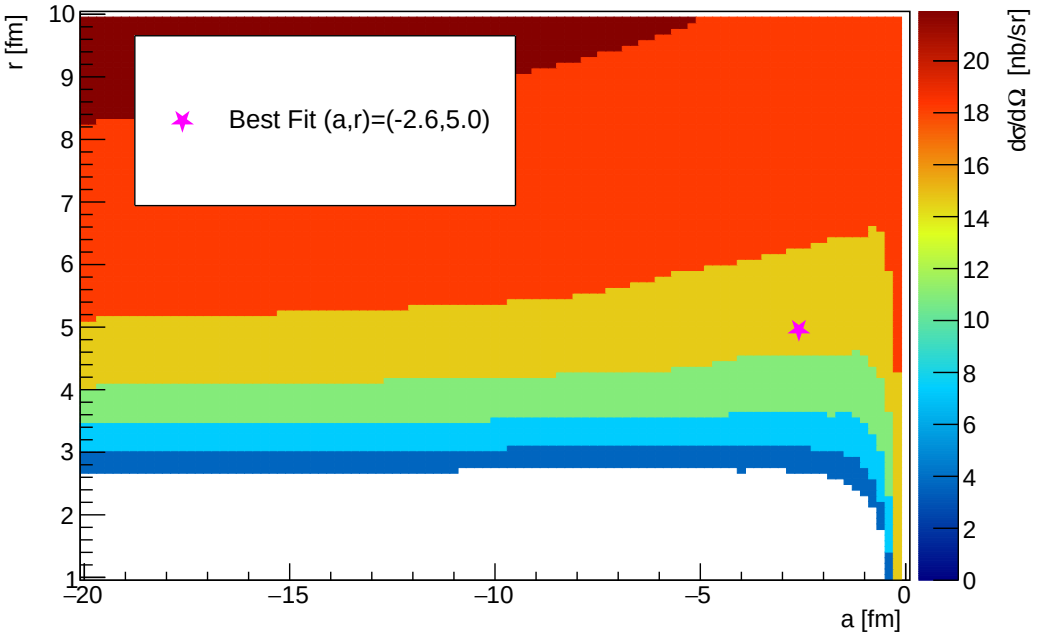

Figure 5.21: Differential cross section of $nn\Lambda$ when chi-square in Eq. 5.28 was calculated. The magenta point is $(a, r) = (-2.6, 5.0)$ fm where chi-square in Fig. 5.20 was minimum, and differential cross section at $(a, r) = (-2.6, 5.0)$ fm is 15 nb/sr.

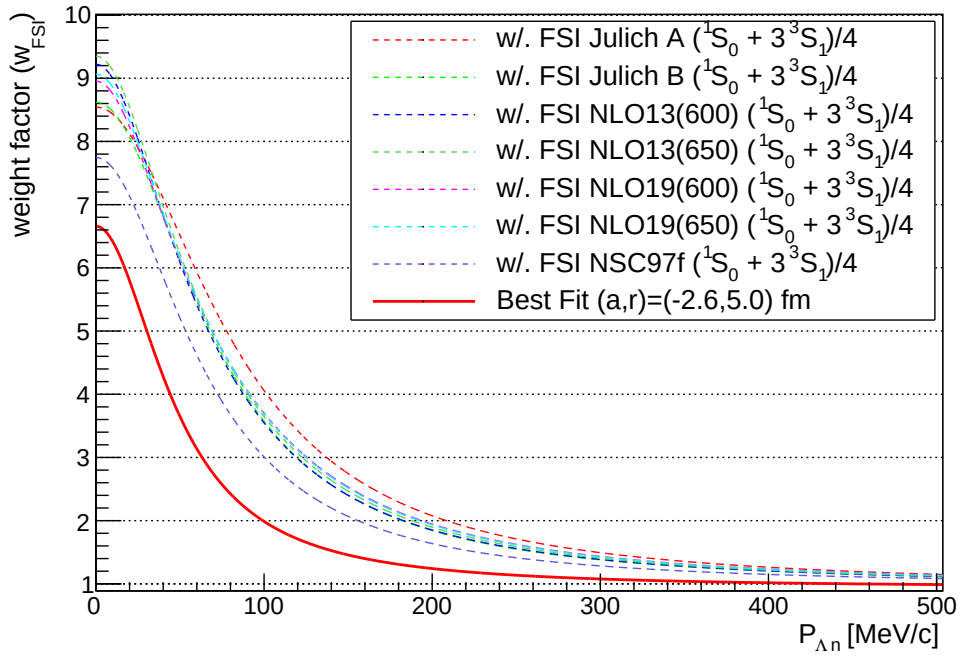

Figure 5.22: Weight factor distributions in each potential model. The weighting factor was defined as $f_{\mathrm{FSI}} \times I$.The red lines represents the weighting factor distribution when scattering length (a) and effective range (r) are -2.6 and 5.0 fm.

5.5.7 Discussion

The effective range (r) is constrained by this experimental data. However, the contour lines in Fig.5.20 is parallel to scattering length directions so the scattering length (a) is not constrained by this experimental data. Therefore, the dependence and trend of each potential parameters are shown as following.

■ **effective range dependence**

The effective range, which is one of the potential parameters for calculating the Jost function. The effective range dependence of influence factor was shown in Fig. 5.24. As the effective range parameter is increased, the amplitude of the influence factors became smaller and tended to converge to $I \to 1$ at $r \to \infty$. The (1σ) contour lines in Fig. 5.19 and 5.20 give us to constrain the effective range by the minimizing chi-squares.

■ **scattering length dependence**

In Fig. 5.20, although there was a chi-square minimum at $(a, r) = (-2.6, 5.0)$ fm, the contour lines of the chi-squares were parallel to the horizontal axis. In order to investigate scattering length dependence, the scattering lengths dependence of reduced chi-square in the range of

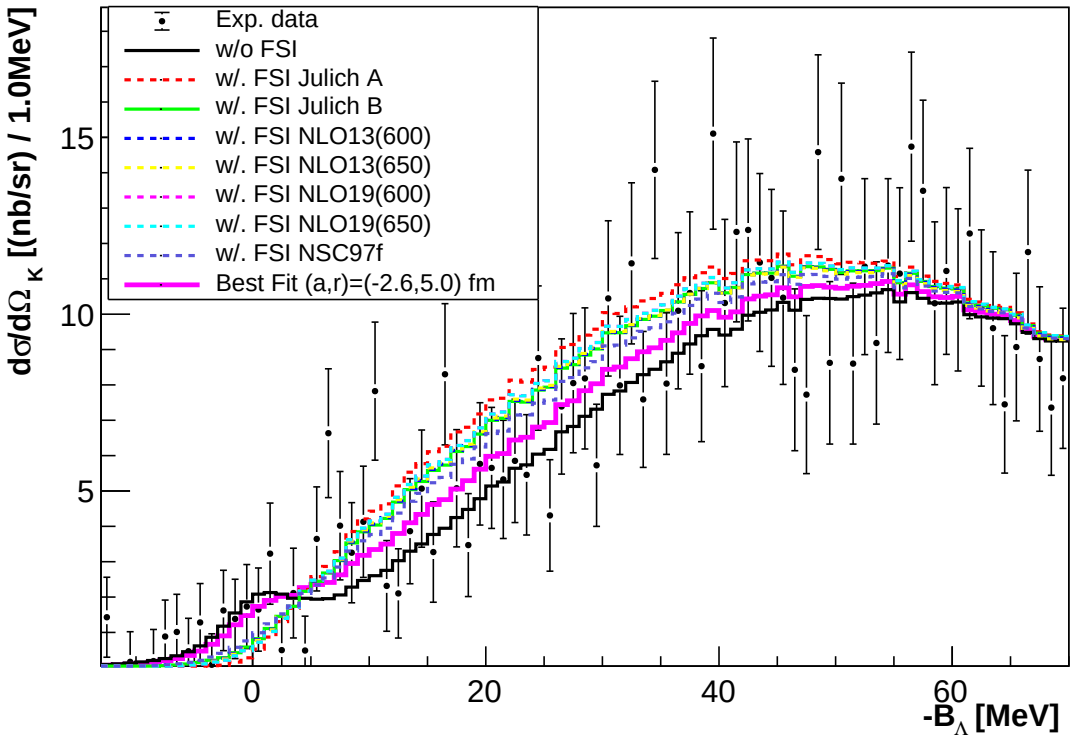

Figure 5.23: Λ-QF distribution by SIMC including FSI at $(a, r) = (-2.6, 5.0)$ fm (magenta line). The differential cross section of $nn\Lambda$ is assuming to be 15 nb/sr.

$-200 \leq a \leq 0$ fm are shown in Fig.5.25 when the effective range was fixed. The chi-square is converged at a certain value for $-a \to \infty$ within the statistical error. Therefore, the experiment could not limit the scattering length.

When effective range was fixed at $r = 4$ fm, the result of influence factor in the range of $-10 \leq a \leq -1.0$ fm was shown in Fig. 5.26. In the region above 100 MeV/c of Λn relative momentum, the amplitude of influence factor was convergent and the amplitude changed significantly in the region below 30 MeV/c. In case of $a \to \infty$, influence factor was obtained as:

$$\lim_{a\to\infty} \mathrm{I}(\mathrm{k_{rel}}) \to 1 + \frac{4}{r^2 k_{\mathrm{rel}}^2}. \tag{5.30}$$

Equation 5.30 indicates that the influence factor at $p_{\Lambda n} = 0$ MeV is divergent. However, this experiment was measured high recoil Λ momentum $p_\Lambda \sim 400$ MeV/c. Since the events below the $p_{\mathrm{rel}} \leq 10$ MeV where the amplitude of the influence factor varies significantly could not be obtained, the scattering length cannot be constrained from this experiment.

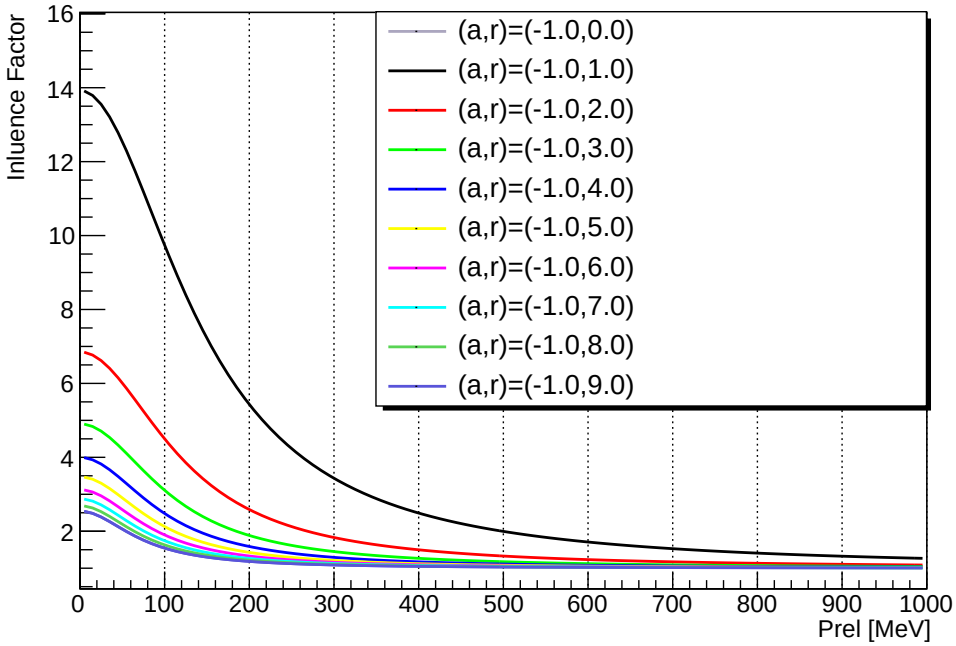

Figure 5.24: Influence factor effective range dependence

5.6 Future plan

5.6.1 Statistical requirement

The Λ-QF distribution including Λn FSI was obtained by using Jost function. In this experiment, the relative systematic error was 18%, which was sufficiently large compared to the relative statistical error at 3%. However, the systematic error does not affect the Λ-QF distribution because it was applied to all Λ-QF productions and only changed scaling of differential cross section. Hence, I investigated the statistical requirement in order to determine the Λn potential among three different potentials (Jülich A, B and NSC97f). Therefore, in order to investigate the difference between the NSC97f potential spectrum and the differential cross section spectra including the Jülich A and Jülich B potentials, the chi-square was defined as,

$$\chi^2_{\mathrm{NSC97f}}(N) = \sum_{i=a}^{N} \frac{(y^i_{\mathrm{NSC97f}} - y^i_{\mathrm{model}})^2}{(\sqrt{w} \times \sigma^i_{\mathrm{NSC97f}})^2}, \tag{5.31}$$

where y^i_{NSC97f}, y^i_{model} were differential cross sections in each bin, and $\sigma^i_{\mathrm{NSC97f}}$ was systematic error in each bin. w represented the statistical wight factor of Λ-QF productions, which was normalized as 1 for the number of Λ-QF productions obtained in this experiment. Figure 5.27 shows the chi-square value when the statistical weight factor was varied. The 95% confidence level in order to determine potential models between NSC97f and other potentials such as Jülich

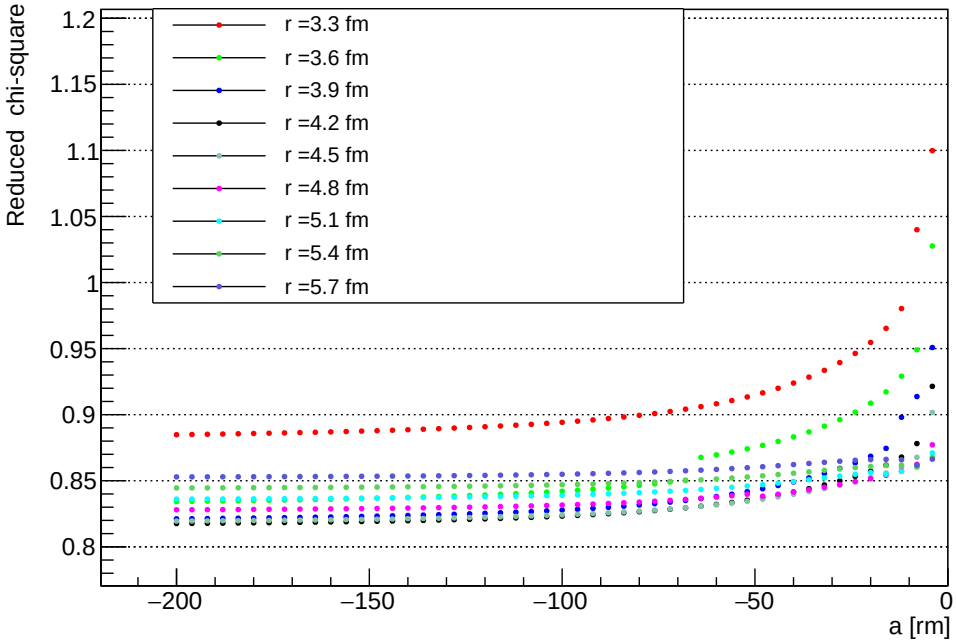

Figure 5.25: FSI scattering length dependence

A, Jülich B was satisfied when the statistical weight was 12. On the other hand, when the statistical weight was 13, The 95% confidence level in order to separate Jülich A from Jülich B was satisfied. Therefore, when Λ-QF production was measured fourteen times more than the number of Λ-QF productions obtained in this experiment, the Λn potential can be determined among three different Λn potentials such as Jülich A, Jülich B and NSC97f.

5.6.2 Experimental design

Study of Λn FSI effect by using Λ-QF shape that mentioned in the thesis would be a good approach to investigate Λn interaction. Further studies are necessary to improve uncertainty. An experiment with higher statistics with HKS spectrometer which has higher acceptance and shorter arm may have a chance to measure Λn potential with a better precision [83]. Because low Λn relative momentum condition is effective to perform Λn FSI studies, experiment with lower momentum transfer reactions such as the in-flight $^3\mathrm{H}(K^-, \pi^-)pn\Lambda$ and $^3\mathrm{H}(K^-, \pi^0)nn\Lambda$ around the magic-momentum are good candidate.

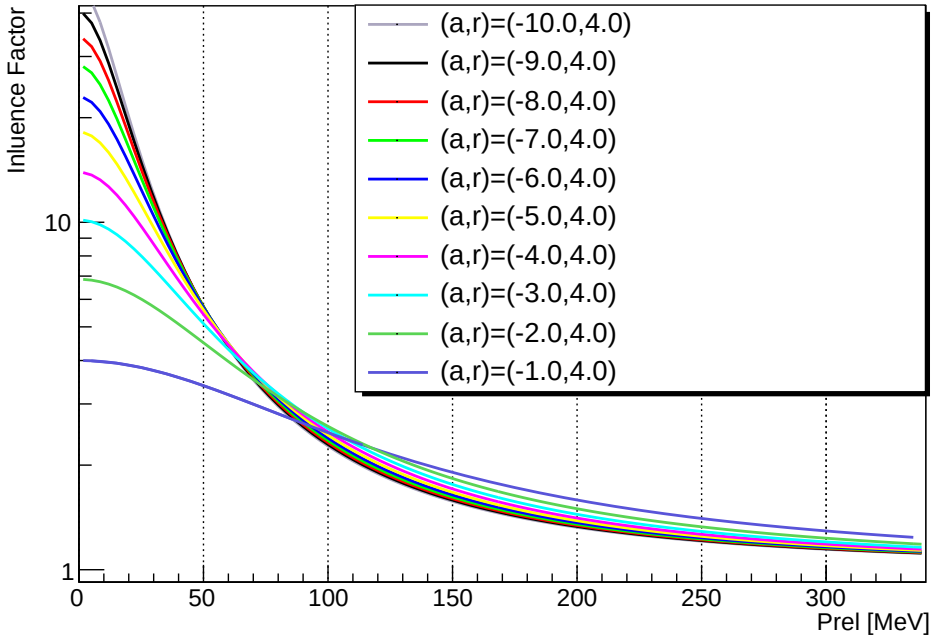

Figure 5.26: Influence factor effective dependence

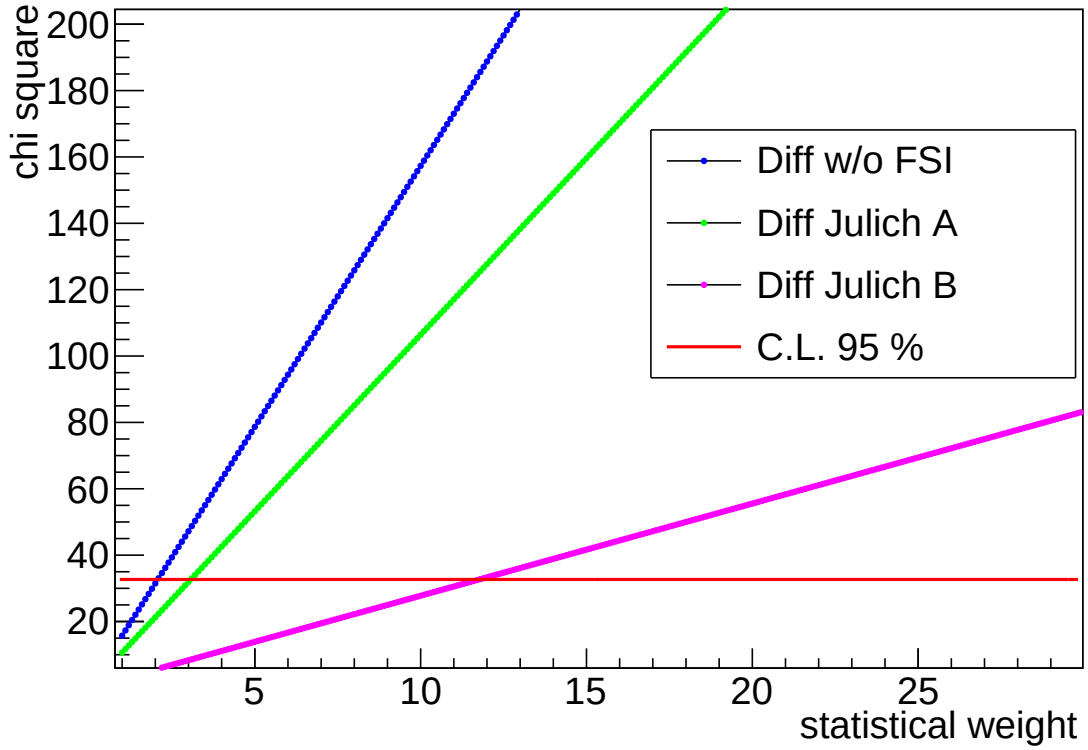

Figure 5.27: Chi-square distribution within a range of $0 \leq -B_\Lambda \leq 40$ MeV. the chi-square was defined in Eq.5.31.

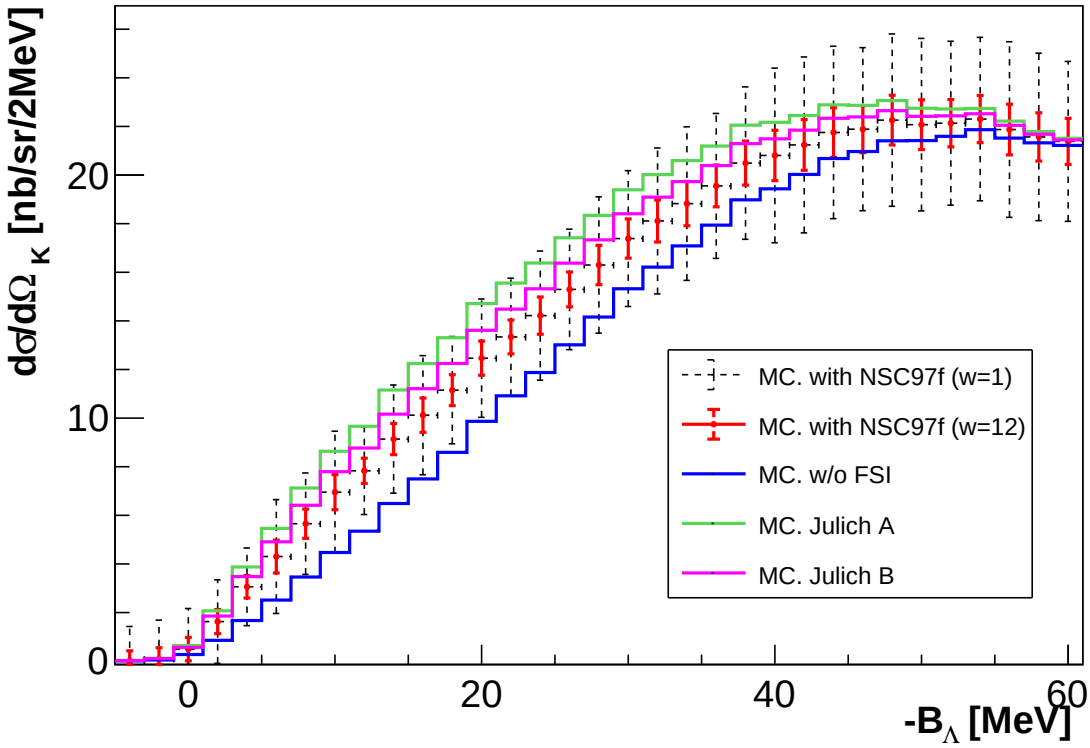

Figure 5.28: The differential cross section distribution obtained by SIMC. The black and red dot lines show the MC spectra including FSI with NSC97f potential model when the weighting factor defined in Eq. 5.31 was to be 1 and 13, respectively.

Chapter 6 Summary

In 2018, the E12-17-003 experiment was performed at JLab to investigate the $nn\Lambda$ with the $(e, e'K^+)$ reaction. A missing mass method in which are calculated with a scattered electron and a kaon measured by the two high resolution spectrometers (HRSs). A gas hydrogen target for the Λ and Σ^0 productions was used to calibrate absolute missing mass. Since this experiment used a 25-cm thick target, the energy calibration method was developed by including the correction for the target thickness effect. As a result of the energy calibration, the Λ and Σ^0 peaks were obtained to be 1115.36$\pm$1.4 MeV/c and 1192.32$\pm$1.5 MeV/c. In the present thesis, experimental results of the $p(e, e'K^+)\Lambda$, $nn\Lambda$ peak and Λ-QF productions in the $^3\mathrm{H}(e, e'K^+)X$ reaction were shown with discussions as follows:

■ $p(e, e'K^+)\Lambda$

The differential cross section of $p(e, e'K^+)\Lambda$ reaction at $\theta_{\gamma K}^{\mathrm{CM}} = 8.4°$, $Q^2 = 0.46$ (GeV/c)^2 and $W = 2.12$ GeV was obtained to be $334 \pm 9(\mathrm{stat.}) \pm 53(\mathrm{syst.})$ nb/sr in the center of mass frame of γK^+.

■ $nn\Lambda$ **peak**

The Faddeev equation by Ref. [41] predicted that there are possibilities existing the $nn\Lambda$ as a resonance state if the Λn potential is 5% deeper than the Λp potential. If the $nn\Lambda$ is a bound or a resonance state, the $nn\Lambda$ peak is expected to be observed. Although some event excess were observed near the $nn\Lambda$ mass threshold in the missing mass spectrum of the $^3\mathrm{H}(e, e'K^+)X$ reaction, significant peaks could not be observed. The differential cross section of the enhancement near the $nn\Lambda$ mass threshold was obtained to be $21.7 \pm 6.7(\mathrm{stat.}) \pm 5.2(\mathrm{syst.})$ nb/sr by fitting with the Breit-Wigner function of $(-B_\Lambda, \Gamma) = (0.55, 4.7)$ MeV.

■ **Λ-QF production in $^3\mathrm{H}(e, e'K^+)X$ reaction**

The Λ quasi-free (Λ-QF) events were observed in the region of $-B_\Lambda \geq 0$ MeV in the $^3\mathrm{H}(e, e'K^+)X$ reaction. The differential cross section of the Λ-QF production was obtained as $880 \pm 20(\mathrm{stat.}) \pm 140(\mathrm{syst.})$ nb/sr. The Λ-QF shape was in good agreement with the result of Monte Carlo simulation by SIMC. However, the SIMC results could not reproduce an event excess around $0 \leq -B_\Lambda \leq 40$ MeV. The structure was expected to be produced by the Λn FSI

effect. The Jost function was applied to estimate the FSI effect on the missing mass. In this thesis, Λ-QF distribution was estimated with the Jost function under the seven Λn potentials, (Jülich A, B, NSC97f, NLO13(600), NLO13(650), NLO19(600) and NLO19(650)). Quantitative comparison between the experimental data and the simulation results was performed with the chi-square method in two ranges ($20 \leq -B_\Lambda \leq 60$ MeV and $0 \leq -B_\Lambda \leq 60$ MeV). In both ranges, the NSC97f potential model was the best fit with the experimental data. The chi-square map of the scattering length (a) and the effective length (r) were made in order to evaluate the potential independent fitting for parameters (a, r). In the range of $20 \leq -B_\Lambda \leq 60$ MeV, the chi-square had the minimum value when the scattering length (a) and effective range (r) had the value of $a = -0.67$ fm and $r = 5.2$ fm. The error of the effective range was $5.2^{+3.2}_{-1.3}$(stat.) fm at $a = -0.67$ fm. In the range of $0 \leq -B_\Lambda \leq 60$ MeV, the chi-square had the minimum value when the scattering length (a) and effective range (r) had the value of $a = -0.67$ fm and $r = 5.2$ fm. The error of the effective range was $5.0^{+1.3}_{-1.2}$(stat.) fm at $a = -2.6$ fm.

■ **Future prospects**

Study of the Λn FSI effect by using Λ-QF shape that mentioned in the thesis would be a good approach to investigate the Λn interaction. Further studies are necessary to improve uncertainty. If there are 14 times larger than statistics than the result in this thesis, it would be possible to determine the Λn potential to be NSC97f model with CL95%. An experiment with higher statistics with HKS which has higher acceptance and shorter arm may have a chance to measure Λn potential with a better precision. Because low Λn relative momentum condition is effective to perform Λn FSI studies, experiment with lower momentum transfer reactions such as the in-flight $^3\mathrm{H}(K^-, \pi^-)pn\Lambda$ and $^3\mathrm{H}(K^-, \pi^0)nn\Lambda$ around the magic-momentum are good candidates.

Acknowledgment

I would like to thank Prof. S.N. Nakamura for supporting me in writing my doctoral thesis and research. Without his generous advice and education in meetings and seminars, I would not have been able to complete my doctoral thesis. In my first year of master course, he gave me a chance to visit JLab and the experience of going abroad at the beginning of my research career gave a great impact on my subsequent research life. I am grateful to Prof. H. Tamura. When I visited his office, he was kind enough to consulted with me about my research and gave me valuable advice. In addition, I learned the hypernuclear physics from his seminar. I would like to express my gratitude to Prof. L. Tang of Hampton University. When I stayed at JLab, I was able to prepare E12-17-003 experiment smoothly thanks to his kind supports. I owe thanks to Dr. K.N. Suzuki for the opportunity to discuss the analysis with him. He gave me advice of his simulation with Geant4. Owing to his wonderful support, I was able to estimate the systematic error of HRS acceptance. It was also very exciting for me to be able to analyze with him. I would like to thank to Dr. B. Pandey for the opportunity to discuss the analysis via BlueJeans and email. In addition, I was invited to his house and became friends with his family, and his kind support enhanced my life in U.S. I would like to thank to Dr. T. Gogami for great help to me both in public and private life. He helped me with every thing and I leaned a lot about not only research. I would like to Dr. S. Nagao for his invaluable advice and suggestions for data analysis. In addition, I was able to finish writing doctoral thesis owing to his correction of it. I learned way to thinking for data analysis and presentation from him. I am deeply grateful for advice and suggestions of Dr. M. Kaneta. His suggestions were very useful in my analysis. I would like to thank to Prof. E. Hiyama, Dr. K. Sekiguchi and Dr. K. Miwa for their invaluable advice. Especially, Prof. E. Hiyama consulted me many times on the theoretical interpretation of this paper. I owe to thank to Dr. Y. Toyama for supported me the E12-17-003 experiment. He always consulted me about my research and provided me with emotional support in my life in Tohoku University. I indebted to Mr. K. Uehara during the beam time in the E12-13-008 experiment. Thanks to his active participation in the night shift of the E12-17-003 experiment, the experiment went smoothly. I would like to thank to Mr. K. Okuyama for helping my analysis in the $p(e, e'K^+)\Lambda/\Sigma^0$ reactions. I would like to express my gratitude to Dr. F. Garibaldi, Prof. P.E.C. Markowitz,, Prof. J. Reinhold and Dr. G. M. Urciuoli for their advice and support. I am deeply grateful

for participating in the E12-17-003 experiment and discussing $nn\Lambda$ analysis to Prof. Y. Fujii and Mr. N. Lashley. I would like to thank to ELS group mates, Dr. Y. Toyama, Mr. K. Uehara, Mr. T. Akiyama, Mr.K. Okuyama, Mr. T. Fujiwara, Mr. M. Mizuno, Mr. Y.R. Nakamura, Ms. Y. Kino, Mr. S. Nagano, Mr.K. Tachibana and Mr. T. Chiaba for their warm support and encouragement. I would like to thank to Ms. H. Kanauchi, Mr. Y. Ishikawa, Ms. T. Roger, Mr. S. Kajikawa, Ms. T. Sakao, Mr. K. Kamata, Mr. T. Kitaoka, Mr. S. Wada, Mr. F. Oura, Mr. T. Morino and Mr. K. Ohashi for their warm support and encouragement. In particular, my classmate Mr. Y. Ishikawa taught me about the gambling, such as horse racing and slots, and I learned the importance of money and time. I would like to thank to Mr. H. Umetsu for his technical support. I would also like to thank secretaries, Ms. A. Takahashi and Ms. S. Sasaki for their support of paperwork for business trips and purchase of research items. This work was supported in part by GP-PU Tohoku univ.. Especially, I would like to thank to Ms. H. Miwa who is secretary of GP-PU for any paperwork and procedures for oversea program.

Bibliography

[1] F. S. Crawford *et al.*, Phys. Rev. Lett. **2**, 174 (1959).

[2] G. Alexander *et al.*, Phys. Rev. Lett. **7**, 348 (1961).

[3] T. Groves, Phys. Rev. 129, 1372 (1963).

[4] P. Beilliére *et al.*, Phys. Lett. **12**, 350 (1964).

[5] L. Piekenbrock *et al.*, Phys. Rev. Lett. **12**, 625 (1964).

[6] B. Sechi-Zorn *et al.*, Phys. Rev. Lett. **13**, 282 (1964).

[7] V. Vishnevskiĭ *et al.*, Sov. J. Nucl. Phys. **3**, 511 (1966).

[8] D. Bassano *et al.*, Phys. Rev. **160**, 1239 (1967).

[9] G. Alexander *et al.*, Phys. Rev. **173**, 1452 (1968).

[10] B. Sechi-Zorn *et al.*, Phys. Rev. **175**, 1735 (1968).

[11] J. Kadyk *et al.*, Nucl. Phys. **B27**, 13 (1971).

[12] K. Anderson *et al.*, Phys. Rev. D **11**, 473 (1975).

[13] R. Mount *et al.*, Phys. Lett. **58B**, 228 (1975).

[14] M. Tanabashi *et al.*, (Particle Data Group), Phys. Rev. D **98**, 030001 (2018).

[15] E. Hiyama *et al.*, Prog. Of Theo. Phys. **97**, 6 (1997).

[16] T. H. Tan, Phys. Rev. Lett. **23** 395 (1969).

[17] C. Pigot, *et al.*, Nucl. Phys. B **249**, 172 (1985).

[18] H. Piekarz, Nucl. Phys. A **479**, 263 (1988).

[19] A. C. Melissinos, *et al.*, Phys. Rev. Lett. **14**, 604 (1965).

[20] J. T. Reed, *et al.*, Phys. Rev. **168**, 1495 (1968).

[21] W. J. Hogan *et al.*, Phys. Rev. **166**,1472 (1968).

[22] R. Siebert *et al.*, Nucl. Phys. A **567**, 819 (1994).

[23] J. T. Balewski, *et al.*, Eur. Phys. J. A **2**, 99 (1998).

[24] B. Bilger, *et al.*, Phys. Lett. B **420**, 217 (1998).

[25] M. Maggiora, *et al.*, Nucl. Phys. A **691**, 329c (2001).

[26] S. Abd El-Samad, *et al.*, Phys. Lett. B **632**, 27 (2006).

[27] A. Budzanowski *et al.*, Phys. Lett. B **687**, 3135 (2010).

[28] F. Hinterberger *et/al.*, Eur. Phys. J **21**, 313321 (2004).

[29] F. Dohrmann *et al.*, Phys. Rev. C **76**, 054004 (2007).

[30] M. A. Faessler *et al.*, Phys. Rev. Lett. B **46**, 468 (1973).

[31] H. Tamura *et al.*, Phys. Rev. Lett. **84**, 5963 (2000).

[32] C. Milner *et al.*, Phys. Rev. Lett. **54**, 1237 (1985).

[33] M. Akei *et al.*, Nucl. Phys. A **534**, 478 (1991).

[34] T. Hasegawa *et al.*, Phys. Rev. Lett. **74**, 224 (1995).

[35] T. Miyoshi *et al.* Phys. Rev. Lett. **9**0, 232502 (2003).

[36] M. Jurič, *et al.*, Nucl. Phys. B, 52, (1973).

[37] B. W. Downs *et al.*, Phys. Rev. Jour. Arch. **114**, 593 (1959)

[38] K. Miyagawa, *et al.*, Phys. Rev. C **51**, 2905 (1995).

[39] C. Rappold *et al.*, Phys. Rev. C **88**, 041001 (2013).

[40] E. Hiyama *et al.*, Phys. Rev. C **89**, 061302 (2014).

[41] I.R. Afnan *et al.*, Phys. Rev. C, **92** 054608 (2015).

[42] Q. Chen *et al.*, Phys. Rev. C **77**, 054002 (2008).

[43] V. B. Belyaev, *et al.,* Nucl. Phys. A, **803**, 210226 (2008).

[44] H. Nemura *et al.,* Prog. Theor. Phys., **103**, 925958 (2000).

[45] T. O. Yamamoto *et al.,* Phys. Rev. Lett. **115**, 222501 (2015).

[46] R. Bradiford *et al.*, Phys. Rev. C **73**, 035202 (2006).

[47] K. H. Glander *et al.*, Euro. Phys. Jour. A **19**, 251273 (2004).

[48] A. Bleckmann *et al.*, Z. Physik **239**, 1 (1970).

[49] R. A. Adelseck *et al.*,, Phys. Rev. C **42**, 108 (1990).

[50] P. Bydžovský *et al.*, Phys. Rev. C **76**, 065202 (2007).

[51] M. Sotona *et al.*, Prog. of Theo. Phys. Supp. **177**, (1994).

[52] R. Bradford et al., Physical Review C 73, 035202 (2006).

[53] Pilat, Proceedings of LINAC2012, TH3A02 792 (2012).

[54] https://hallaweb.jlab.org/github/halla-osp/version/Standard-Equipment-Manual.pdf

[55] O. Hashimoto, *at al.*, Prog. In Part. And Nucl. Phys. **57**, 564653 (2006).

[56] J. Alcorn *et al.*, Nucl. Inst. and Meth. In Phys. Rev. A **522** (2004).

[57] M. Mihovilovic, UNIVERSITY OF LJUBLJANA (2012), arXiv:1208.0748.

[58] J. C. Denard, *et al.*, Proce. Of The 2001 Part. Accel. Conf. 2326 (2002).

[59] S.N. Santiesteban *et al.*, Nucl. Phys. Inst. and Meth. A, **940** (2019).

[60] K.G. Fissum *et al.,* Nucl. Inst. and Meth. A, **474** 108131 (2001).

[61] M. lodice *et al.*, Nucl. Phys. Inst. and Meth. A, **411** (1998).

[62] W. A. Watson III et. al., IEEE transactions on nuclear science 41, 1 (1994).

[63] D. J. Abbott et. al., “CODA performance in the real world”.

[64] X. Li *et al.*, J Phys. G: Nucl. Part. Phys. **17**, 1127(1991).

[65] R. M. Mohring, *et al.*, Phys. Rev. C, **67**, 055205 (2003).

[66] R. M. Barnett *et al*. Phys. Rev. D, **54** 1 (1996).

[67] P. A. Zyla *et al.,* (Particle Data Group), Prog. Theor. Exp. Phys. **2020**, 083C01 (2020).

[68] https://github.com/itabasi/SIMC

[69] https://www.phy.anl.gov/theory/research/momenta/

[70] C. Ciofi degli Atti *et al*., Phys. Rev. C, **21** (1980).

[71] C. Ciofi degli Atti *et al*., Phys. Rev. C, **66**, 044004 (2002).

[72] R. Cruz-Torres, *et al*., Phys. Lett. B, **797**, 134890 (2019).

[73] R. B. Wiringa *et al*., Phys. Rev. C, **89**, 024305 (2014).

[74] D. Koltenuk Ph.D. thesis Univeristy of Pennsylvania (1999).

[75] http://www.rcnp.osaka-u.ac.jp/ sakemi/OPERA/user-3d.pdf

[76] S. Kato. Nucl. Inst. Meth., Phys. Res. Sect. A, **611**, 113 (2009).

[77] J. C. David *et al*., Phys. Rev. C **52**, 2613 (1996).

[78] T. Mart *et al*.,, Phys. Rev. C **61**, 012201 (R) (1999).

[79] K. H. Glander *et al*., Eur. Phys. J. A **19**, 251 (2004) .

[80] R. Bradford *et al*., Phys. Rev. C **73**, 035202 (2006).

[81] M. E. McCracken *et al*., Phys. Rev. C **81**, 025201 (2010).

[82] M. Sumihama *et al*., Phys. Rev. C **73**, 035214 (2006).

[83] T. Gogami *et al*., Phys. Rev. C **93**, 034314 (2016).

[84] R. M. Mohring et al., Phys. Rev. C **67**, 055205 (2003).

[85] T. Mizutani *et al*., Phys. Rev. C **58**, 75 (1998).

[86] T. Mart *et al*., Phys. Rev. C **61**, 012201 (1999).

[87] T. Corthals *et al*., Phys. Rev. C **73**, 045207 (2006).

[88] L. D. Cruz *et al*., Phys. Rev. Lett. **108**, 182002 (2012).

[89] C. J. Bebek *et al*., Phys. Rev. D **15** 594 (1977).

[90] C. N. Brown *et al*., Phys. Rev. Lett. **28**, 1086 (1972).

[91] D. Skoupil *et al*., Phys. Rev. C **93**, 025204 (2016).

[92] D. Skoupil *et al*., Phys. Rev. C **97**, 025202 (2018).

[93] K. Okuyama, Master thesis University of Tohoku (2020).

[94] V. B. Belyaev *et al*., Nucl. Phys. A, **803**, 210226 (2008).

[95] H. Kamada *et al*., EPJ Web Conf., **113**, 07004 (2016).

[96] B. Holzenkamp *et al.,* Nucl. Phys. A, **500**, 485528 (1989).

[97] V. G. J. Stoks *et al.,* Phys. Rev. C, **59**, 3009 (1999).

[98] J. Haidenbauer *et al.,* Few-Body-Systems **62**, 105 (2021).

[99] J. Haidenbauer private community (2022).

[100] M. L. Goldberger *et al.,* Collision Theory.